Coherent spin dynamics and carrier-nuclear interaction in lead halide perovskite crystals

Johan Erik Kirstein

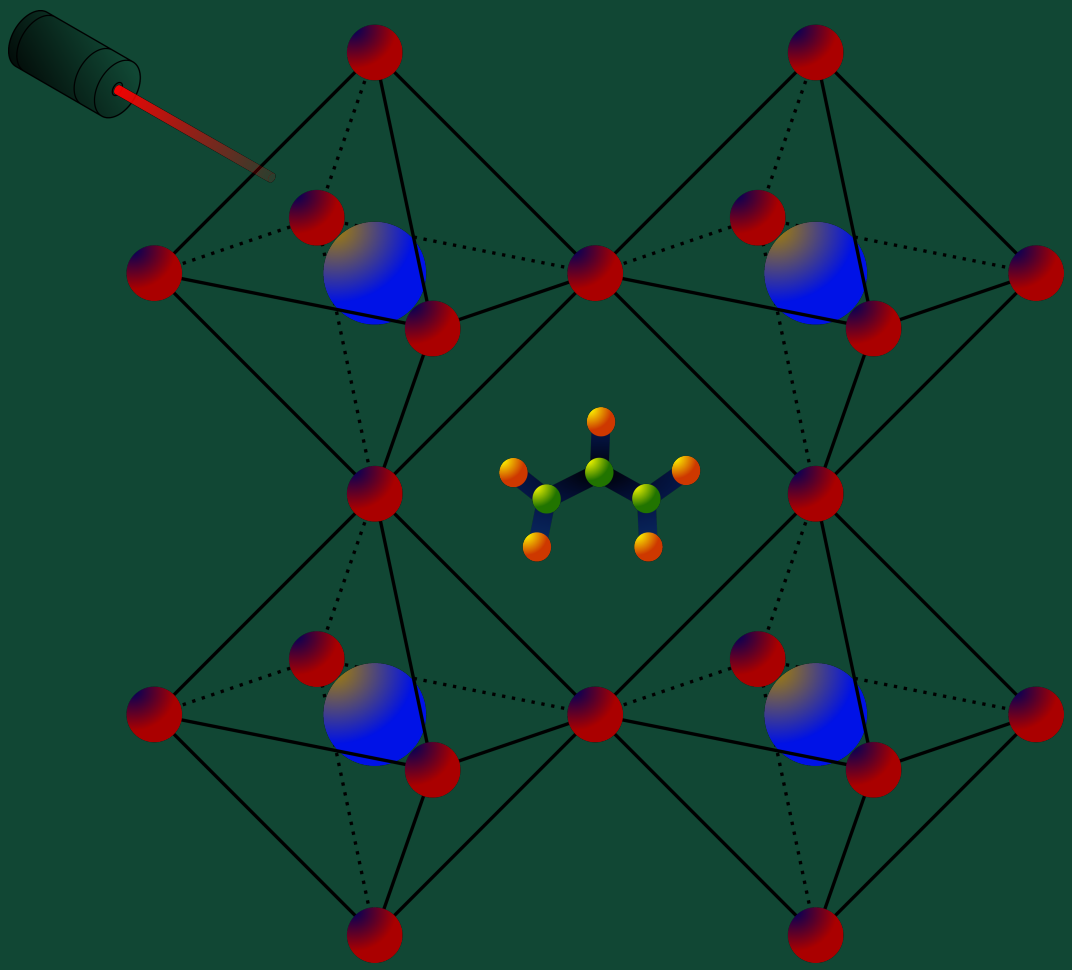

Coherent spin dynamics and carrier-nuclear interaction in lead halide perovskite crystals

Dissertation

submitted in partial fulfilment of
the requirements for the degree of

Dr. rer. nat.

to the Department of Physics
TU Dortmund University, Germany

by

JOHAN ERIK KIRSTEIN

Dortmund, February 2022

technische universität
dortmund

Examination Board:
PD Dr. Alex Greilich
Prof. Dr. Mirko Cinchetti
Dr. Hans Dembinski
Prof. Dr. Roland Böhmer

Abstract

In the present work, the charge carrier spin dynamics in lead halide perovskites $A\mathrm{Pb}X_3$, with $X = \{\mathrm{I,Br,Cl}\}$ are studied. The lead halide perovskites are distinguished with respect to the groups of purely inorganic perovskites with $A = \mathrm{Cs}$ and hybrid organic inorganic ones with $A = \{\mathrm{MA,FA}\}$ (methylammonium and formamidinium), as well as their size, i. e. macroscopic single crystals or nano crystals. The spin dynamics of the charge carriers, electrons and holes, are mainly investigated using picosecond resolution Kerr and Faraday spectroscopy. In addition, the observation of the spin dynamics is complemented by exciton spectroscopy (polarization-resolved photoluminescence, reflection, and transmission) and time-resolved differential reflectometry. Nanosecond spin dynamics are observed and the underlying interaction mechanisms are revealed by the experimental techniques, with a focus on interaction of charge carrier and nuclear spins.

Kurzfassung

In der vorliegenden Arbeit wird die Ladungsträger-Spindynamik in Blei-Halogen-Perowskiten $A\mathrm{Pb}X_3$, mit $X = \{\mathrm{I,Br,Cl}\}$ untersucht. Die Blei-Halogen-Perowskite werden in rein inorganische Perowskite mit $A = \mathrm{Cs}$ und hybride organisch-inorganische mit $A = \{\mathrm{MA,FA}\}$ (Methylammonium and Formamidinium) sowie in ihrer Größe als makroskopische Einkristalle und Nanokristalle unterschieden. Die Spindynamik der Ladungsträger, Elektronen und Löcher, wird hauptsächlich anhand von Kerr- und Faraday-Spektroskopie mit einer Pikosekunden Auflösung untersucht. Zusätzlich wird die Spindynamik durch Exzitonen-spektroskopie (polarisationsaufgelöste Photolumineszenz, Reflektion und Transmission) sowie durch zeitaufgelöste differentielle Reflektrometrie untersucht. Es werden nanosekundenlange Spindynamiken beobachtet, deren zugrundeliegende Wechselwirkungsmechanismen durch die experimentellen Techniken aufgedeckt werden. Ein Schwerpunkt liegt hierbei auf der Untersuchung der Ladungsträger-Kern-Spinwechselwirkung.

Contents

1 Introduction

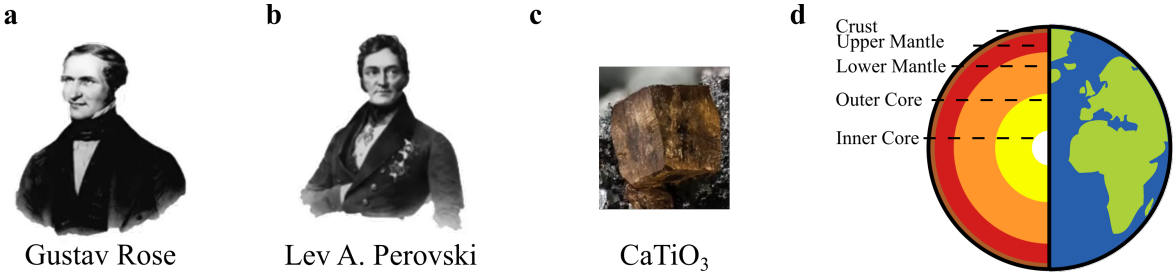

Figure 1.0.1 Introduction. **a** Gustav Rose, who first classified perovskite $CaTiO_3$. **b**, Lev A. Perovski, eponym of the perovskites. **c**, photograph of $CaTiO_3$. **d**, perovskites are the most abundant minerals on earth. 93% of the lower mantel is formed by $(Mg,Fe)SiO_3$. [©**a-c** the copyright is expired]

Fully inorganic and hybrid organic lead halide perovskites, which will be studied in this work, are a subclass of the more general perovskite structure. Perovskite defines a crystallographic structure group, as like for instance the zincblende structure, which can be formed by a wide range of materials in compositional the form of ABX_3, with A, B a pair of cations and X the anion.

The perovskite crystal group is in fact one of the most abundant mineral groups on earth. For instance the perovskite bridgmanite, ($(Mg,Fe)SiO_3$), is assumed to form 93% of the lower earth mantel [Mur12] and thus is with 38% of the total earth mass the most common mineral [Tsc14]. However bridgmanite is only stable in high pressures, above 24 GPa, and thus absent on the earth surface [Hem92].

The first perovskite crystal was discovered 1839 by Gustav Rose, a German mineralogist who studied a mineral originated from Ural mountains. He named the mineral after Lev A. Perovski (Rus. Лев А. Перовский), a russian nobleman, later proposer of the Russian Geographical Society and minister of inner affairs [Att15]. The chemical classification of the first known perovskite as $CaTiO_3$ by Rose, was then taken up by Goldschmidt in 1926 who generalized the mineral by a isomorphic class, covering a broad set of chemical compositions [Gol26]. An enormous range of theoretical and practical works have joined it. Prominent perovskites are ferroelectric perovskites like $BaTiO_3$ or $Pb[Zr_xTi_{1-x}]O_3$ (PzT) (the most used

piezoelectric material)[Att15] or high-T_c cuprate superconductors like $YBa_2Cu_3O_7$ (for which Bednorz and Müller were awarded with the nobel prize) [Bed88].

Another promising candidate was found 2009 by Kojima et al. [Koj09]. In this work the high quantum efficiency of solar cells based on hybrid organic lead halide perovskite methylammonium lead tri-iodine ($MAPbI_3$) was the first time described. Since then, a lot of progress was made on the class of lead halide perovskites in terms of composition, crystal quality etc. whereas a quantum efficiency of 25% was then exceeded [Nre; Jeo21]. Such value is on the scale of mono crystalline Si or GaAs based solar cells, while lead halide perovskites exhibit the advantage of being less demanding in production [Jen19]. The rapid progress of such perovskites is a further incentive for expanded applications. Lead halide perovskites were shown to operate as luminous, easy colour tunable light emitting diodes [Fu19] (nanocrystals), high energy scintillators [Naz17; Wei19], a variety of optoelectronic devices [Sut16; Mur20], and other spintronic applications [Wan19] (like a spin valve).

The huge potential of lead halide perovskites give rise of an important question: what are the physical reasons for this potential? All-inorganic lead halide perovskites are already in the scientists scope for decades [Sak69; Fuj74; Hir78; Ito79; Frö79], as they show unique properties in the very fundamentals of semiconductor physics. Compared to common III-V and II-VI semiconductors, they have in some sense an inverted band structure: the valence band (VB) states are formed by *s*-orbitals, while the conduction band (CB) states are contributed by *p*-orbitals. This work is dedicated to the particular problem, to which extend the physical description, in particular the carrier and nuclear spin as well as optical properties, of III-V and II-VI semiconductors could be brought to lead halide perovskites. Basically, the method of optical spin control will be used. It allows for ultrafast manipulation on time scales shorter than the spin relaxation, giving an *in situ* observation of spin dynamics.

2

Theoretical Basics

In this theory section, a brief introduction to relevant physical properties of lead halide perovskites will be presented. First, the lead halide perovskite bandstructure will be discussed, with a particular interests in comparison to common semiconductors, followed by the interconnected properties of the carrier Landé factor (g-factor) and consequences arising form the perovskite crystal structure for the carrier spin dynamics and for the process of optical spin polarization. Lastly, the focus turns from bulk to nanostructures, with a spotlight on confinement and heterostructure effects.

2.1 Bandstructure

The bandstructure of lead halide perovskite crystals differs, significantly, from materials like GaAs or similar zincblende like structures. Both experimentally and theoretically many questions are still unsolved. However, a description based on the Bloch theorem [Ash76; Mei84; Fox01; Win03; Ivc05; Kit05; Aws08; Gla18] can be given as follows [Nes21; Yu19].
The wavefunction of a carrier in a periodic potential $U(\mathbf{r}) = U(\mathbf{r} + \mathbf{R})$ can be described by a plane wave multiplied a function with periodicity of the crystal. This is named the Bloch theorem .

$$\Psi(\mathbf{r})\mathbf{E} = \Psi(\mathbf{r}) \left[\frac{-\hbar^2 \nabla^2}{2m_0} + U(\mathbf{r}) \right] \tag{2.1.1}$$

$$\Psi(\mathbf{r}) = e^{i\mathbf{k}\cdot\mathbf{r}} u(\mathbf{r}), \tag{2.1.2}$$

with Eq. (2.1.1) the Hamiltonian of the crystal and Eq. (2.1.2) the wave function. The solution of the Bloch functions leads to the formation of energy bands in the momentum k-space, Fig. 2.1.1. The optical band gap is formed between the first unoccupied band and the last occupied one form the conduction band (cb) and valence band (vb), respectively. For zinc-blende like structures (e.g. ZnSe, GaAs, CdTe) the spin orbit coupling leads to a total angular momentum of the cb similar to s-type orbitals with $J = L + S = 0 + 1/2$ and of the vb similar to p-type orbitals with $J = 1 + 1/2 = 3/2$. In the vb, the orientation quantization of the total angular momentum of $J = 3/2$ with the related quantum number m_J leads to the separation of the higher $J = 3/2$ bands with $m_J = \pm 3/2, \pm 1/2$, the heavy hole ($m_J = \pm 3/2$,

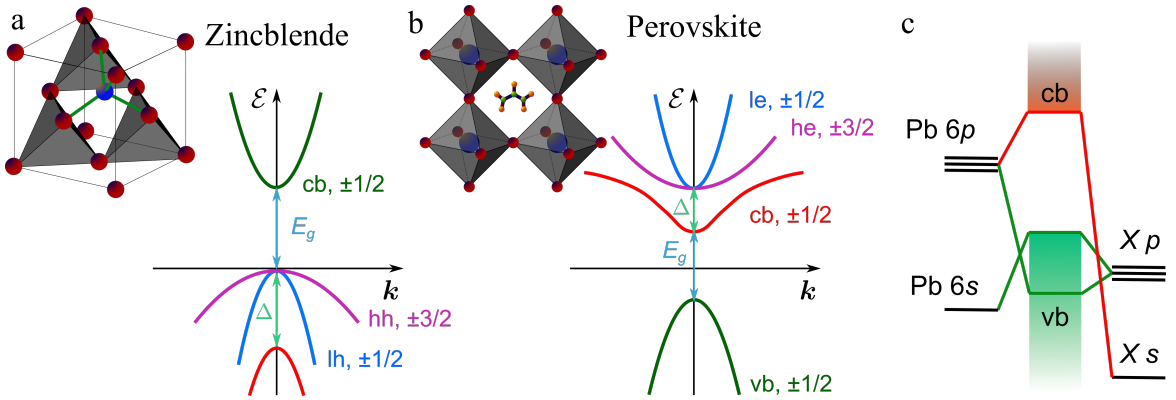

Figure 2.1.1 Perovskite bandstructure in vicinity of band gap. Bandstructure in vicinity of direct band gap for, **a**, zincblende type crystals, **b** bulk perovskite crystals. Bands are labelled with valence band (vb), conduction band (cb) and respective light/heavy electron or hole bands (le, he, lh, hh). Optical band gap is formed between cb and vb and the split off bands separated by spin orbit energy (Δ). In upper left corner the respective sketches of the crystal unit cell is given, in the case of zinc blende with regular tetrahedrons forming the crystal. Front tetrahedron is kept open (without grey box) to visualize the atomic basis of red and blue balls (e.g. the name giving zinc (red) and sulphur (blue)). For lead halide perovskites, the crystal unit cell is formed by corner shared octrahedra (grey), with red balls halogen, blue enclosed lead, and complex molecule, here exemplary FA. **c** The lead halide perovskite band structure can be understood as linear combination of atomic orbitals. Anti bonding between lead (left) and halogen (right) orbitals forms the valence and conduction band.

hh) and light hole ($m_J = \pm 1/2$, lh) band, and a split off band with $J = 1/2, m_J = \pm 1/2$. The situation is reversed in perovskites. The character of the chemical bonds has here less covalent but rather strong ionic character, Fig. 2.1.1**c** [Zei16]. The perovskite crystal lattice is shown in Fig. 2.1.1**b**, upper corner. The lattice consists of corner shared octrahedra composed of lead in the center and the halogen on the corners. In the space between the corner shared octrahedra, the A cation of ABX_3 is located, in this work Cs, FA, MA. For the ionic description, it is sufficient to consider the atomistic orbital structure of lead and the halogen, Fig. 2.1.1**c**[¶]. The band gap of the perovskite crystals is mainly given by the energy difference between lead $6p$ and the corresponding halogen p orbital. Thus, the lowering of the atomic number n from $n = 5$ iodine, $n = 4$ bromide to $n = 3$ chlorine clearly increases the band gap. However, in detail, lead and the halogen form sp bonding and antibonding orbitals. with the band gap composed of the two antibonding orbitals $6p$-ns (cb) and $6s$-np (vb) [‡]. The anti bonding orbital is higher in energy as compared to the composing atomic orbitals thus vacancy states originating from the halogen X p and s have energy levels below the valence band [Bra17]. Unbound lead $6p$ orbitals, however, are located within the band gap.
The orbital configuration leads to a conduction band being nearly p-type and the top of the valence band s-type. Note that according to previous atomistic discussion and total consideration of the density of states (DOS), a significant p-type character for the rest of the

[¶]See further, the linear combination of atomic orbitals (LCAO). The band gap is formed between the highest occupied molecular orbital and lowest unoccupied molecular orbital (HOMO-LUMO).
[‡]$sp\sigma^*$-bond

valance band would be given. The VB Pb-I mixing ratio is estimated to be close to 1:3, while the CB has only about 5% I contribution [Nes21; Fro14; BR16; Tar18; Yu19].
However, anticipating the experimental results, it will be shown that the top of the valence band, and hence the optical properties of the hole, show a dominant coupling to the lead 6s-orbital. It is therefore sufficient to regard the valence band as s-type. The p-type conduction band splits into the lower energy split off band $J = 1/2$ and the higher $J = 3/2$ heavy and light electron bands.
For perovskite crystals, a Rashba splitting is discussed [Nie16; MY21; Kep15; Kim14; Hua21] but is so far not strongly evidenced [Saj20]. In the following it will be neglected.

2.1.1 Tight-Binding

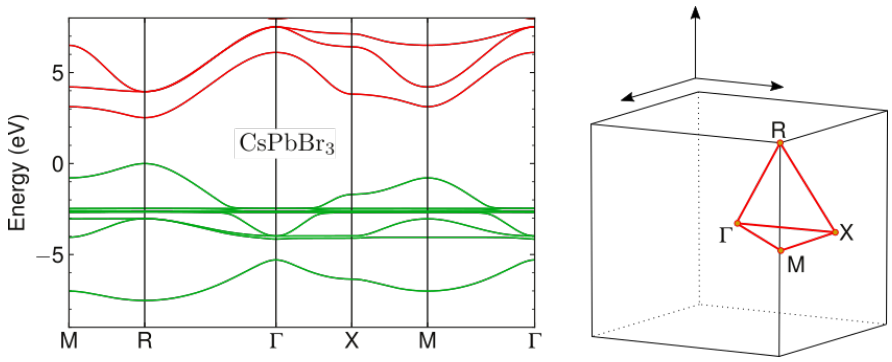

Figure 2.1.2 Band structure. Left, numerically calculated band structure for $CsPbBr_3$ calculated in the empirical tight-binding method, adopted from [Nes21; Kir21b]. The topmost valence band (greens) and the lowest conduction bands (reds) form a direct band gap at the R-point, see Fig. 2.1.1**a**. **Right**, sketch illustration of crystallographic directions in Brillouin zone.

The band structure of $CsPbBr_3$ can be calculated by using the density functional theory (DFT) as well as by the tight-binding (TB) approach [Nes21]. DFT and TB have similar results, thus one can focus on only one theory, the TB theory. The TB is an approach to approximate the (numerical) solution of the band structure of a crystal under only consideration of the nearest neighbour orbital interaction. For TB, an $sp^3d^5s^*$ basis and pseudo cubic symmetry was chosen. Lower symmetry classes could be derived from this as perturbations [Eve15]. The results of the calculus is shown in Fig. 2.1.2. A direct band gap forms at the R-point of the Brillouin zone and is in general good agreement with experimental results discussed in this work.

2.1.2 Carrier g-factor

The Zeeman effect, so the spin coupling to a magnetic field, differs for a free carrier, i.e. an electron in vacuum and a carrier spin inside a solid state matrix. In the first instance, the Zeeman effect for an electron in vacuum $E_Z = g_0\mu_B \boldsymbol{B} \cdot \boldsymbol{S}$ with the vacuum electron g-factor $g_0 = 2.0023$, μ_B the Bohr magneton, $\boldsymbol{B}$ the magnetic field vector, and $\boldsymbol{S}$ the spin vector,

can be rewritten with by replacing $g_0 \to g_c$ to an effective g-factor g_c where the subscript c specifies typically the carrier type and other parameters [Rot59].
To derive the carrier g-factor, one needs to start with the explicit treatment of the spin-orbit Hamiltonian of the crystal [Yug07; Sir97; Ivc05; Kir21b]. The Bloch function for perovskite crystals reads for the valence band,

$$\text{valence band:} \quad \begin{cases} u_{v,\frac{1}{2}}(\boldsymbol{r}) = \mathrm{i}\mathcal{S}(\boldsymbol{r})|\uparrow\rangle\,, \\ u_{v,-\frac{1}{2}}(\boldsymbol{r}) = \mathrm{i}\mathcal{S}(\boldsymbol{r})|\downarrow\rangle\,, \end{cases} \tag{2.1.3}$$

with $|\uparrow\rangle\,, |\downarrow\rangle$ the basic spinors, and $\mathcal{S}(\boldsymbol{r})$ the invariant function according to the valence band s-orbital [Kir21b]. The Bloch functions for the conduction band are

$$\text{bottom conduction band (c.b.):} \quad \begin{cases} u_{c,\frac{1}{2}}(\boldsymbol{r}) = -\sin\vartheta\mathcal{Z}(\boldsymbol{r})|\uparrow\rangle - \cos\vartheta\dfrac{\mathcal{X}(\boldsymbol{r}) + \mathrm{i}\,\mathcal{Y}(\boldsymbol{r})}{\sqrt{2}}|\downarrow\rangle\,, \\ u_{c,-\frac{1}{2}}(\boldsymbol{r}) = \sin\vartheta\,\mathcal{Z}(\boldsymbol{r})|\downarrow\rangle - \cos\vartheta\dfrac{\mathcal{X}(\boldsymbol{r}) - \mathrm{i}\,\mathcal{Y}(\boldsymbol{r})}{\sqrt{2}}|\uparrow\rangle\,, \end{cases} \tag{2.1.4}$$

$$\text{excited (light electron) c.b.:} \quad \begin{cases} u_{le,\frac{1}{2}}(\boldsymbol{r}) = \cos\vartheta\,\mathcal{Z}(\boldsymbol{r})|\uparrow\rangle - \sin\vartheta\dfrac{\mathcal{X}(\boldsymbol{r}) + \mathrm{i}\,\mathcal{Y}(\boldsymbol{r})}{\sqrt{2}}|\downarrow\rangle\,, \\ u_{le,-\frac{1}{2}}(\boldsymbol{r}) = \cos\vartheta\,\mathcal{Z}(\boldsymbol{r})|\downarrow\rangle + \sin\vartheta\dfrac{\mathcal{X}(\boldsymbol{r}) - \mathrm{i}\,\mathcal{Y}(\boldsymbol{r})}{\sqrt{2}}|\uparrow\rangle\,, \end{cases} \tag{2.1.5}$$

$$\text{excited (heavy electron) c.b.:} \quad \begin{cases} u_{he,\frac{3}{2}}(\boldsymbol{r}) = -\dfrac{\mathcal{X}(\boldsymbol{r}) + \mathrm{i}\,\mathcal{Y}(\boldsymbol{r})}{\sqrt{2}}|\uparrow\rangle\,, \\ u_{he,-\frac{3}{2}}(\boldsymbol{r}) = \dfrac{\mathcal{X}(\boldsymbol{r}) - \mathrm{i}\,\mathcal{Y}(\boldsymbol{r})}{\sqrt{2}}|\downarrow\rangle\,, \end{cases} \tag{2.1.6}$$

with $\mathcal{X}, \mathcal{Y}, \mathcal{Z}$ the representation of p-orbitals ($\mathcal{P}$). The parameter ϑ determines the relation between the crystalline splitting and the spin-orbit interaction, with values $\cos\vartheta = \sqrt{2/3}$, $\sin\vartheta = 1/\sqrt{3}$ in cubic crystal symmetry approximation.

With the definition of the interband momentum matrix elements

$$p = \mathrm{i}\langle\mathcal{P}|p_{x,y,z}|\,\mathcal{S}\rangle, \mathcal{P} \in \{\mathcal{X}, \mathcal{Y}, \mathcal{Z}\} \tag{2.1.7}$$

the g-factor dependence can be derived, p is assumed to be real. The g-factor dependence reads

$$g_{vb} = 2 - \frac{4p^2}{3m_0}\left(\frac{1}{E_g} - \frac{1}{E_g + \Delta}\right) \tag{2.1.8}$$

$$g_{cb} = -\frac{2}{3} + \frac{4p^2}{3m_0}\frac{1}{E_g}(+\Delta g). \tag{2.1.9}$$

Note, the term Δg is not part of this derivation but rather taking into account the higher

and lower energy remote bands contributions, see [Kir21a]. It is worth noting that the carrier effective mass has a similar dependence as the g-factor, $\frac{1}{m_{vb}} = \frac{1}{m_0} - \frac{2p^2}{3m_0^2}\left(\frac{1}{E_g} + \frac{2}{E_g+\Delta}\right)$, $\frac{1}{m_{cb}} = \frac{1}{m_0} + \frac{2p^2}{3m_0^2}\frac{1}{E_g}$.

2.1.3 g-factor Anisotropy

A g-factor anisotropy may arise if the symmetry of the carrier wave function is lowered, e.g. due to crystallographic anisotropy, see Sec. 2.1.4.
To start with one symmetry breaking, as e.g. it is present in tetragonal configuration $a = b \neq c$-axis, the light and heavy electron band degeneracy lifts $\Delta \to \Delta_{le}, \Delta_{he}$ due to non zero crystal field splitting Δ_c. The heavy and light electron spin orbit splitting reads

$$\Delta_{le} = \sqrt{\Delta_{SO}^2 + \Delta_c^2 + \frac{2}{3}\Delta_{SO}\Delta_c},\ \Delta_{he} = \frac{\Delta_{le} + \Delta_{SO} + \Delta_c}{2},\ \tan(\vartheta) = \frac{2\sqrt{2}\Delta_{SO}}{\Delta_{SO} - 3\Delta_c}, \quad (2.1.10)$$

with ϑ the relation between the crystalline splitting and the spin orbit splitting (Δ_{SO}). Further the interband momentum matrix elements split $p \to p_\parallel, p_\perp$,

$$p_\perp = \mathrm{i}\langle\mathcal{X}|p_x|\mathcal{S}\rangle = \mathrm{i}\langle\mathcal{Y}|p_y|\mathcal{S}\rangle\,, p_\parallel = \mathrm{i}\langle\mathcal{Z}|p_z|\mathcal{S}\rangle\,. \quad (2.1.11)$$

The anisotropic electron and hole g-factors are

$$g_{vb,\parallel} = 2 - \frac{2p_\perp^2}{m_0}\left(\frac{\cos^2(\vartheta)}{E_g} + \frac{\sin^2(\vartheta)}{E_g + \Delta_{le}} - \frac{1}{E_g + \Delta_{he}}\right), \quad (2.1.12)$$

$$g_{vb,\perp} = 2 - \frac{2\sqrt{2}p_\parallel p_\perp}{m_0}\cos(\vartheta)\sin(\vartheta)\left(\frac{1}{E_g} - \frac{1}{E_g + \Delta_{le}}\right), \quad (2.1.13)$$

$$g_{cb,\parallel} = -\frac{2}{3} + \frac{2p_\perp^2}{m_0}\frac{\cos^2(\vartheta)}{E_g}, \quad (2.1.14)$$

$$g_{cb,\perp} = -\frac{2}{3} + \frac{2\sqrt{2}p_\parallel p_\perp}{m_0}\frac{\cos(\vartheta)\sin(\vartheta)}{E_g}. \quad (2.1.15)$$

$\parallel$ and $\perp$ relate to a, b and c-axis respectively. In a further broken symmetry, e.g. if $a \neq b$, a 3×3 g-tensor needs to be used, whereas in the experiment the g-factor magnitude

$$g = \sqrt{g_{xx}^2\cos(\varphi)\sin(\theta) + g_{yy}^2\sin(\varphi)\sin(\theta) + g_{zz}^2\cos(\varphi)\cos(\theta)} \quad (2.1.16)$$

is the relevant quantity which defines the Zeeman splitting, with the angles φ and θ chosen to suit the experimental configuration e.g. with light propagation along z-axis, see Fig. 3.3.2.

2.1.4 Perovskite Crystallography

All perovskites are of aristotype cubic symmetry. However, depending on the stoichiometry a related symmetry reduction occurs. Glazer identified 23 relevant point groups for the perovskite crystal class in 1972 and became patron of the Glazer notation [Gla72; Gla75; How98; Ale76; Ale01]. The perovskite crystals form a network of corner shared BX_6 octrahedra

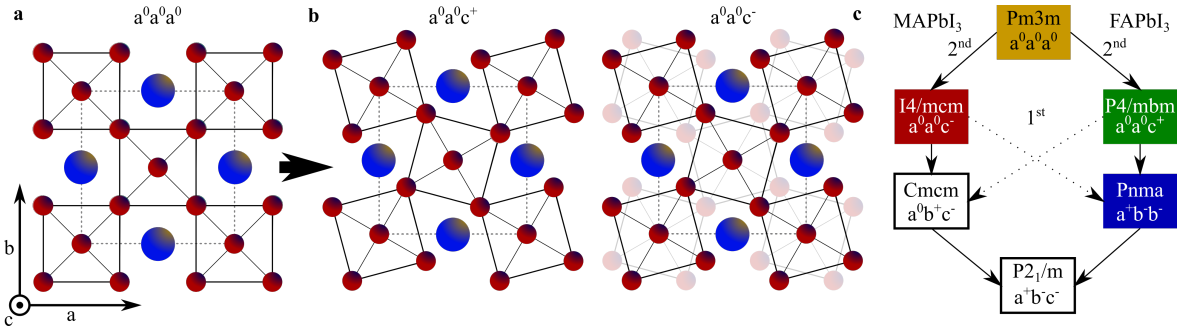

Figure 2.1.3 Octahedral tilting. The lattice of cubic symmetry (**a**), undergoes a phase transition with octahedral tilting. **b**, tilting all sequenced layers in phase ($a^0a^0c^+$), **c**, tilting the first layer in phase but the next layer out of phase ($a^0a^0c^-$). **c** Symmetry class hierarchy for organic lead halide perovskites. Cubic Pm3m reduces to tetragonal I4/mcm ($MAPbI_3$) or P4/mbm ($FAPbI_3$) and ends for both MA and FA based in orthorhombic Pnma.

encapsulating the A cation in the formed gaps. Essentially, all subgroups of perovskite crystals can be derived via octrahedra tilting from the cubic parent. In the Glazer notation $a^0a^0a^0$ refers to a cubic phase with each position corresponding to one of the principal axis [100] [010] [001]. The tilt along a specific axis is then indicate by a letter representing the magnitude and a direction, e.g. $a^0a^0b^+$ refers to an in phase tilt ($^+$) along the c axis with magnitude b. Superscripts reads as ^{0} no-, $^+$ in-,$^-$ out of phase tilt. The corner shared octrahedra tilting is sketched in Fig. 2.1.3**b**.

The octrahedra tilting is closely linked to the close packaging of the crystal whose tendencies can be quantified via the Goldschmidt tolerance factor t [Gol26]. It describes the size ratio of the cation B radius r_B inside the corner shared octrahedra to the outer A cation r_A together with the anion size r_X, $t = \frac{r_A+r_X}{\sqrt{2}(r_B+r_X)}$. For organic cations, as they are present in hybrid organic perovskites, the ion radius corresponds to an averaged radius of a statistically orientated ion, i.e. ball like shape [BR16]. The average atom and molecule radii are given in table 2.1.1. The optimal tolerance factor is close to unity. Too far away from unity, the incorporated organic molecule either exceeds the space given by the octahedron or does not fill it sufficiently. Both cases render the perovskite crystal unstable. One finds for different iodine based perovskites: $MAPbI_3$ $t = 0.91$ and $CsPbI_3$ t=0.85 and $FAPbI_3$ t=0.99.

The octrahedral tilting occurs as temperature-induced transition. In elevated temperatures, the perovskites typically exhibit cubic symmetry. When the temperature is lowered M and R-zone boundary phonon modes condensate [Fuj74; Tre82] and in case of hybrid organic inorganic perovskites, the organic cation nutation freezes [Fro16]. The role of the frozen cation therein is not yet fully clarified but suggested to have a significant influence [Har18; Var19]. In contrast to all inorganic crystals (A =Cs), in case of an organic molecule cation, the specific stereochemistry (with MA (C-N) an axial molecule and FA (N-C-N) showing a triangular shape) and a highly reactive hydrogen surrounding needs to be considered.

The possible paths of symmetry reduction is shown exemplary for $MAPbI_3$ and $FAPbI_3$ in Fig. 2.1.3**c**. For $MAPbI_3$ and $FAPbI_3$, the first phase transition is accompanied by a different tilt of the octrahedra. For $MAPbI_3$, an out of phase tilt (red square) and for $FAPbI_3$ (green

Table 2.1.1 Ionic radii taken from [Oku15; Kie15; Oku20] as well as various tolerance factors for hybrid organic and fully inorganic lead halide $APbX_3$ perovskites. For non pure A-side or X-side perovskites, a weighted average of ionic radii are taken.

Cation	r [Å]	Anion	r [Å]	Material	t
Pb^{2+}	1.18	I^-	2.20	$MAPb\{I_3/Br_3/Cl_3\}$	{0.91/0.93/0.94}
Sn^{2+}	0.93	Br^-	1.96	$FAPb\{I_3/Br_3/Cl_3\}$	{0.99/1.01/1.02}
Cs^+	1.88	Cl^-	1.81	$CsPbI\{I_3/Br_3/Cl_3\}$	{0.85/0.86/0.87}
MA^+	2.17			$FA_{0.9}Cs_{0.1}PbBr_{0.2}I_{2.8}$	0.97
FA^+	2.53				

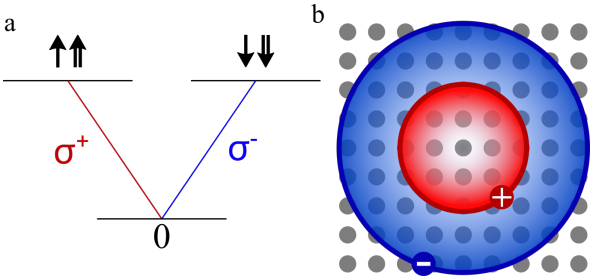

Figure 2.2.1 Optical excitation. **a**, selection rules of a spin 1/2 electron and hole. From groundstate $|0\rangle$, circular polarized light $\sigma^{\pm}$ excites to $J = 1 = \Uparrow\uparrow$ and $J = -1 = \Downarrow\downarrow$, respectively. **b**, representation of a Wannier-Mott exciton. Blue (red) electron (hole) radius, black dots crystal lattice.

square) an in-phase tilt was observed [Whi16; Sto13; Epe14; Oku20; Mas20; Fab16]. Both space groups are tetragonal. With further cooling, a phase transition towards orthorhombic (blue square) Pnma occur. For $MAPbI_3$ and $FAPbI_3$, the phase transition from cubic to tetragonal is of 2^{nd}-order. The phase transition from tetragonal to orthorhombic phase is for $MAPbI_3$ of 1^{st}-order and for $FAPbI_3$ of 2^{nd}. Typically, the phase transition towards orthorhombic phase occurs at temperatures far above liquid helium, e.g. 160 K for $MAPbI_3$. In general, the lead halide perovskites are in orthorhombic phase at temperatures where the spin dynamics are observed in this work. Note, of the most direct consequences of the octahedral tilting is a change of the optical band gap energy [Pra17].

2.2 Optical Polarization of Carrier Spins

The optical polarization of carrier spins is achieved, by lifting an electron out of the valence band to the conduction band resulting in a photoexcited electron and hole pair. The photoexcited carriers typically relax rapidly to the band extrema and recombine within few hundreds of picoseconds under emission of a photon giving the characteristic photoluminescence. First in order to realize optical spin polarization, the angular moment conservation needs to be fulfilled. Circular polarized light ($\sigma^{\pm}$) carries an angular momentum of ± 1, thus a combination of both spin 1/2 conduction and valence band in form of $\Uparrow\uparrow$ and $\Downarrow\downarrow$ is allowed, called selection rules (Fig. 2.2.1**a**) [Mei84]. Linear polarized light (s,π) has an angular moment equal to zero, so doesn't establish, a spin polarization. Second it is beneficial to use a resonant energy and avoid above band excitation which gives rise of a carrier relaxation to the band extrema via phonon emission. Typically, the spin polarization of localized carriers is established by resonant excitation of states below the band gap energy, by the excitation of an exciton (X), see next section, donor bound excitons (D^0X), trions (T) etc.

2.2.1 Exciton

An electron and hole attract each other by the Coulomb interaction $E_C = \frac{e^2}{4\pi\epsilon\epsilon_0|r_e - r_h|}$, with e the elementary charge, ϵ_0 the vacuum permittivity, ϵ the dielectric constant and $|r_e - r_h|$ the distance between electron and hole. Similar to the hydrogen problem, a bound state forms the exciton. The exciton follows a hydrogen like energy series $E_X(n) = -R_y \frac{\mu}{m_0}\frac{1}{\epsilon^2}\frac{1}{n^2}$ with the n the principal quantum number and $R_y = \frac{m_0 e^4}{8\epsilon_0^2 h^2} = 13.6$ eV the Rydberg energy, $1/\mu = 1/m_e + 1/m_h$ the exciton reduced mass $\mu \approx 0.1\ m_e$ (see Sec. 2.9.1). The exciton radius a_X calculates to $a_X = a_B \frac{\epsilon m_0}{\mu} n^2$ with the Bohr radius $a_B = \frac{h^2\epsilon_0}{\pi m_0 e^2} = 0.529$ Å. For a typical exciton, in $A\mathrm{Pb}X_3$, the exciton binding energy is in the range of tens of meV (e.g. 16 meV for $MAPbI_3$ [Miy15]) and the exciton radius for instance, amounts to $a_X(\mathrm{CsPb\{Cl,Br,I\}}) = \{2.5, 3.5, 6\}$ nm [Nes18]. The exciton size is bigger than the lattice constant and treated as Wannier-Mott exciton [Bö18]. Note, one can find in agreement to the above statements a dielectric constant of $\epsilon \approx 4 - 9$ [Miy15; Nes18].

2.3 Electron and Hole Spin Dynamics

2.3.1 Spin in Magnetic Field

A spin, in the semiclassical picture a magnetic dipol, which is subject to a magnetic field, will experience a force, described by the Zeeman Hamiltonian $\mathcal{H}_Z = g\mu_B \mathbf{BS}$. In case of a magnetic field B_z pointing in the same direction as the spin ($S_z = \pm 1/2$) (typical Faraday geometry), it is intuitive to express it as a magnetic dipol being attracted or repelled by the parallel or anti parallel magnetic field. The degenerated spin energy level splits proportional to the magnetic field by $E_Z = g\mu_B B$. If the magnetic field is inclined out of parallelity the magnetic dipol will experience a torque, hence in a non-parallel magnetic field the spin will precess, named Larmor precession. The Larmor precession frequency equals the Zeeman splitting $\hbar\omega_L = g\mu_B|B|$.
In quantum mechanical terminology, the spin dynamics described via the time evolution operator $U = e^{-i\frac{\mathcal{H}_Z t}{\hbar}}$, with $\mathcal{H}_Z = g\mu_B \mathbf{BS} = \omega_L S$. Assuming a magnetic field applied in x direction (typical Voigt geometry), the spin states S_x will become the eigenstates and time independent, while S_y and S_z evolve in time. Analytically, it can be shown that the expectation values of $\langle S_y\rangle$ and $\langle S_z\rangle$ give

$$\langle S_x\rangle = 0, \langle S_y\rangle = 1/2\hbar \sin(\omega_L t), \langle S_z\rangle = 1/2\hbar \cos(\omega_L t) \tag{2.3.1}$$

[Bes05; Sak11]. With a spin initially excited in S_z, the Larmor precession, in the plane orthogonal to the magnetic field (z-y plane), is reproduced.

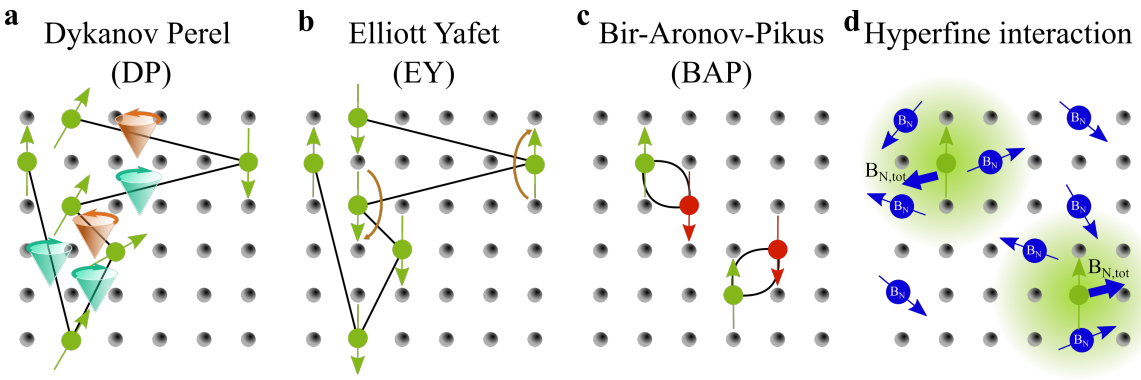

Figure 2.3.1 Spin relaxation mechanisms. **a**, Dyakonov-Perel mechanism, between scattering events, the spin precesses in the effective spin orbit field. Inversion of movement direction inverses the precession direction. **b**, Elliott-Yafet mechanism, a scattering moment may cause a spin flip. **c**, Bir-Aronov-Pikus mechanism, electron hole exchange scattering. **d**, Hyperfine interaction, different nuclear spin surrounding gives different local net magnetic fields for different spins.

2.3.2 Spin Relaxation

The spin orientation can get lost after some time. One distinguishes between the spin relaxation time T_1, the spin decoherence time T_2, and the spin dephasing time T_2^*. The spin relaxation time T_1 describes the relaxation of the spin polarization along an external field axis and therefore characterises the timescale of energy dissipation, e.g. towards the crystal lattice via angular momentum transfer to phonons. The relaxation ultimately stops once the higher entropy, random, thermal equilibrium orientation is reached. The decoherence time T_2 is the time it takes for the state to lose its coherence, e.g. for a single spin, the decoherence time describes the timescale on which the spin orientation can be continuously expressed by a superposition of eigenstates, with a well-defined phase relation. The loss of phase does not require an energy transfer [Bes05]. T_2 is also named transverse relaxation time. The dephasing time T_2^* describes, as T_2, the loss of phase information but for an ensemble of spins. If one considers a set of spins which experience all a slightly different local environment, as to crystal imperfections or inhomogeneities, all spins will precess slightly different, i.e. faster or slower, and thus the full ensemble, even if each individual spin holds its coherence, will be, as an ensemble, out of phase. The dephasing time T_2^* is given by the inverse sum of T_2 and an inhomogeneous contribution T_{inh}, $\frac{1}{T_2^*} = \frac{1}{T_2} + \frac{1}{T_{\text{inh}}}$ [Yak08]. The mentioned effect of different precession frequencies can be characterised, for example, by a spread of g-factor Δg, leading to a inhomogeneous dephasing term $\frac{1}{T_{\text{inh},\Delta g}} = \frac{\Delta g \mu_B B}{\hbar}$.
It is worth to note, that the inhomogeneous part T_{inh} is again a collection of multiple individual terms. If to rule out one, e.g. by measuring a series of magnetic fields and extrapolating to zero field or by observing a dependence on the excitation light intensity and extrapolation to the low intensity of single spin excitation, still multiple uncontrollable terms will bring a deviation from the observed time towards T_2. However, it is possible to access T_2 even in the presence of an ensemble, with the spin echo technique [Abr94]. The technique is not used in this work and is therefore not discussed in detail.
Next, sources for, carrier spin relaxation shall be discussed [Pri21; Bes05]. Most of the

relaxation mechanisms are inspired by studies based on zincblende semiconductors, but will be presented here in order to evaluate their influence on the perovskite system. In zincblende crystals the inversion symmetry is broken, enabling spin orbit effects leading to the Dyakonov-Perel (DP) and the Elliot-Yafet mechanism (EY). Further carrier-carrier exchange, namely electron hole exchange, is considered with the Bir-Aronov-Pikus mechanism. Finally the carrier–nuclear spin, hyperfine, interaction is regarded. A sketch of each mechanism is shown in Fig. 2.3.1.

2.3.3 Dyakonov-Perel Mechanism

A major spin relaxation mechanism for free charge carrier spins is the Dyakonov-Perel mechanism [Dya72]. In non-centrosymmetric crystals, e.g. zincblende crystals like GaAs, the spin orbit interaction manifests as effective spin orbit field causing a spin precession between scattering events. The situation is sketched in Fig. 2.3.1**a**. The spin precession leads to a phase change proportional to the time between scattering events τ and the effective precession frequency $\Omega_{\mathbf{k}}$ in the wavevector $\mathbf{k}$ dependent spin-orbit field, given by the spin orbit Hamiltonian $\mathcal{H} = \hbar\mathbf{\Omega}_{\mathbf{k}} \cdot \mathbf{S}$ [Kir21b] with $\mathbf{S}$ being the charge carrier spin operator. The relaxation rate for the Dyakonov-Perel mechanism reads

$$\frac{1}{\tau_s^{(DP)}} \sim \langle \Omega_{\mathbf{k}}^2 \tau \rangle, \tag{2.3.2}$$

the angular brackets denote the averaging over the thermal distribution. The proportionality of the relaxation rate to the scattering time, i.e. a longer relaxation time with more scattering events, may seem unintuitive, but can be motivated as an analogue to the effect of motional narrowing [Kos19]. At each scattering event, the precession in the effective spin orbit field is disturbed and the phase accumulation appears towards a different angle. Partly, the phase accumulated before the scattering event may get reversed in that way. The more often the reorientation happens, the more the absolute phase accumulation sums up to zero.
For perovskite crystals centrosymmetry, in particular for the case of hybrid organic-inorganic lead halide perovskites and the complex shaped organic cation, is not ensured. In cubic realization, at high temperatures where the cation orientation smears out, perovskite crystals should show a central symmetry. However, in the various symmetry reductions which occur in perovskite crystals evidences are present that the central symmetry is broken, e.g. this would lead to the formation of Rashba- and Dresselhaus-effects [Kim14; Kep15; Nie16].

2.3.4 Elliott-Yafet Mechanism

The Elliot-Yafet (EY) mechanism referees to a spin orbit effect which occurs at a scattering event with phonons or impurities [Gla18]. In real centrosymmetric semiconductors, Bloch states are not real eigenstates and thus the spin orientation can mix at a scattering event [Bes05], Fig. 2.3.1. For the Elliot-Yafet model, the more scattering events take place, the shorter the relaxation time is

$$\frac{1}{\tau_s^{(EY)}} \sim \frac{1}{\tau}. \tag{2.3.3}$$

Uncertainties in the actual perovskite symmetry under study can not fully neglect this model.

2.3.5 Bir-Aronov-Pikus Mechanism

Another relaxation mechanism arises, if one considers, the presence of both electron and hole spins. They may interact in terms of an exchange interaction, $\mathcal{H} = \pi a_B^3 \hat{D} \delta(\mathbf{r}_\mathrm{e} - \mathbf{r}_\mathrm{h})$, with $\hat{D}$ as exchange operator applied on both electron and hole spins, a_B the Bohr radius, $\mathbf{r}_\mathrm{e}$ and $\mathbf{r}_\mathrm{h}$ the carrier position-vectors for electron and hole, $\mathbf{K}_\mathrm{e}$ and $\mathbf{K}_\mathrm{h}$ the electron and hole wavevectors. The exchange operator can be considered as a short range and long range interaction $\hat{D} = \hat{D}_\mathrm{short} + \hat{D}_\mathrm{long}$. The short range interaction $\hat{D}_\mathrm{short} = \Delta(\boldsymbol{S}_\mathrm{e} \cdot \boldsymbol{S}_\mathrm{h})$ is a pure spin-spin exchange with $\boldsymbol{S}_\mathrm{e(h)}$ the spin operator of electron and hole and Δ an interaction parameter. The long range exchange is of excitonic character and reads $\hat{D}_\mathrm{long} = \hbar\omega_{LT} \left[1 - (\hat{\boldsymbol{J}} \cdot \frac{\boldsymbol{K}}{K})^2\right]$ with $\hbar\omega_{LT}$ the longitudinal-transverse splitting of an exciton in a bulk crystal, $\boldsymbol{K} = \boldsymbol{K}_\mathrm{e} + \boldsymbol{K}_\mathrm{h}$ the exciton wavevector and $\hat{\mathbf{J}}$ its angular momentum. The Bir-Aronov-Pikus (BAP) mechanism calculates to

$$\frac{1}{\tau_s^{(BAP)}} \sim \frac{\langle \hat{D}^2 \rangle}{E_B^2} \tau_{eh}^{-1}, \tag{2.3.4}$$

with τ_{eh} the electron hole scattering rate and $E_B = \hbar^2/(2m_e a_B^2)$ the Bohr energy. The BAP mechanism is efficient if one of the carriers is unpolarized e.g. if a strong imbalance of relaxation times is present or e.g. a non polarized residual doping exist [Kir21b].

2.3.6 Hyperfine Interaction

An important relaxation channel is driven by the hyperfine interaction [Kir21b; Gla18]. Within the carrier localization volume with a radius of a few nanometer approximately ten thousands of atoms, are located. Of this atoms, a significant amount shows a non vanishing spin moment, see table 2.3.1. In a simplistic picture, this nuclear spins give rise to a small magnetic field which leads to spin precession (see Fig. 2.3.1**d**) and, in a quantum mechanical picture, a mixing of spin states following the Hamiltonian

$$\mathcal{H}_\mathrm{hf,e(h)} = A_\mathrm{e(h)} \mathbf{I} \cdot \mathbf{S}_\mathrm{e(h)}, \tag{2.3.5}$$

with $A_\mathrm{e(h)}$ the carrier hyperfine constant. The hyperfine interaction is considered to be isotropic [Kir21b] and will further lead to a damping of the carrier spin polarization in the absence of an external magnetic field, see polarization recovery curve Sec. 2.5 and the phenomenon of dynamic nuclear polarization, Sec. 2.4.

2.4 Hyperfine Interaction - Dynamic Nuclear Polarization

A major aspect of the hyperfine interaction, despite providing a relaxation channel (Sec.2.3.6) or damping of the spin polarization (Sec. 2.5), is the chance to transfer the carrier spin polarization to the nuclear spin system (NSS). The Hamiltonian

$$\mathcal{H} \;=\; \mathcal{H}_\mathrm{Z,e(h)} + \mathcal{H}_\mathrm{Z,N} + \mathcal{H}_\mathrm{hf,e(h)} \tag{2.4.1}$$

with the hyperfine term $\mathcal{H}_\mathrm{hf,e}$ (Eq. (2.3.5)), and $\mathcal{H}_\mathrm{Z,e(h)} + \mathcal{H}_\mathrm{Z,N}$ the carrier and nuclear Zeeman terms, implies spin flips between carrier $\mathbf{S}$ and nuclear spins $\mathbf{I}$. Thus continuous pumping of

Table 2.3.1 Major abundant non-zero nuclear spin isotopes in $FA_{0.9}Cs_{0.1}PbI_{2.8}Br_{0.2}$. The table columns give: isotope number, natural abundance α, nuclear spin I, relative dipole moment of the isotope μ relative to the nuclear magneton μ_N, gyromagnetic ratio γ [Kir21b].

Isotope	α	I	μ/μ_N	γ [MHz/T]
^{207}Pb	22.1%	1/2	0.58	8.882
^{133}Cs	100%	7/2	2.58	5.623
^{127}I	100%	5/2	2.81	8.578
^{79}Br	50.7%	3/2	2.1	10.704
^{81}Br	49.3%	3/2	2.27	11.538
^{35}Cl	75.8%	3/2	1.06	4.176
^{37}Cl	24.2%	3/2	0.88	3.476
^{14}N	100%	1	0.4	3.077
^{13}C	1%	1/2	0.7	10.708
^{1}H	100%	1/2	2.8	42.577

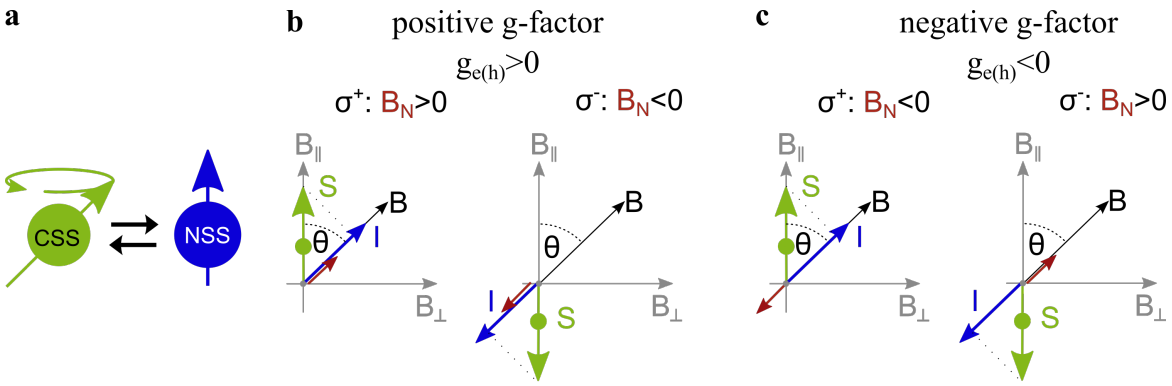

Figure 2.4.1 Dynamic nuclear polarization. **a**, Carrier spin system (CSS) acts on nuclear spin system (NSS) which in turn interacts with CSS. **b**, Polarization of nuclear spin polarization (blue arrows) depend on carrier spin polarization (green arrows) and magnetic field direction (black arrow **B**). Thus the resulting Overhauser field (red arrow) depends on the carrier g-factor sign, the excitation helicity ($\sigma^{\pm}$). If the g-factor of the carrier is positive (like for electrons in lead halide perovskites) and σ^+ polarized light is applied, the Overhauser field acts additive to the external magnetic field (for σ^- subtractive). **c**, for a negative g-factor the situation is reversed, for σ^+ excitation, the Overhauser field is subtractive and for σ^- additive. $B = \sqrt{B_{\parallel}^2 + B_{\perp}^2}$

the carrier spin polarization may lead to a nuclear spin polarization out of thermal equilibrium (see Fig. 2.4.1**a**). The rise of a nuclear polarization will in turn act back on the carrier spin system (CSS). As seen from the Hamiltonian, Eq. (2.3.5) and Eq. (2.4.1), a non vanishing hyperfine term will dependent on the spin polarization sign, $\mathrm{sgn}(\mathbf{S}_{\mathrm{e(h)}})$, lower or raise the carrier energy level. In the same way with additional multiplier, the sign of g-factor, the Zeeman splitting is structured. Thus, the Larmor frequency of the carrier will either increase or decrease with the nuclear polarization in respect to the bare Zeeman splitting case. Hence, the back action of the nuclear polarization on the carrier spin can be understood as a change of the magnetic field, $B \rightarrow B + B_{\mathrm{N}}$, experienced by the carrier,

$$\boldsymbol{\omega}_{\mathrm{L}} = \frac{g\mu_B}{\hbar}(\mathbf{B} + \mathbf{B}_{\mathrm{N}}). \tag{2.4.2}$$

B_{N} is named Overhauser field [Ove53]. In a material like GaAs, an Overhauser field of up to 5.3 T was predicted [Pag77] and also observed [Moc17].
The nuclear polarization $\langle \mathbf{I} \rangle$ can be derived as

$$\langle \mathbf{I} \rangle = \ell \frac{4I(I+1)}{3} \frac{\boldsymbol{B}(\boldsymbol{B} \cdot \boldsymbol{S})}{B^2} \tag{2.4.3}$$

[Abr94; Mei84; Gla18; Bel19] with $\boldsymbol{B}$ the magnetic field, $\boldsymbol{S}$ the steady state carrier spin polarization and I the nuclear spin number, $0 < \ell < 1$ refers to a phenomenological leakage factor.

The leakage factor is related to the spin dynamics of the nuclear spin system. As introduced in Sec. 2.3.2, T_1, T_2 and T_2^* need to be considered. In general, the dephasing and decoherence times range above μs and are much longer than the carrier spin relaxation times, and are therefore neglected for the carrier nuclear spin interaction. The nuclear spin relaxation is composed of a carrier nuclear spin flip term T_{sf} and a part, T_d, collecting all other losses, e.g. phonon emission etc., such as $T_1^{-1} = T_{\mathrm{sf}}^{-1} + T_d^{-1}$ [Gla18]. The leakage factor is defined as the ratio between this two times via

$$\ell = \frac{T_d}{T_{\mathrm{sf}} + T_d}. \tag{2.4.4}$$

2.4.1 Hyperfine Constant

Dominant for the hyperfine interaction is the contact type interaction, as used previously (Eq. (2.3.5)), but in more general it is a dipol-dipol interaction. For s-type orbitals, the (Fermi-)contact interaction is driven with a hyperfine coupling constant

$$A_s = \frac{\mu_0}{4\pi} \frac{8\pi}{3} (g_n \mu_N)(g_{e(h)} \mu_B) |\Psi(0)|^2, \tag{2.4.5}$$

here μ_0 the magnetic permittivity, μ_N and μ_B the nuclear and Bohr magneton with respective g-factors and $|\Psi(0)|^2$ the wavefunction integral, evaluated at the position of the nucleus. For p-type, and higher order, orbitals $|\Psi(0)|^2 = 0$ and the much weaker general dipol-dipol term becomes important [Gla18; Dya08; Sli90; Den06]

$$A_p = \frac{\mu_0}{4\pi} \frac{2}{5} (g_n \mu_N)(g_{e(h)} \mu_B) \left\langle \frac{1}{r^3} \right\rangle \left\langle 3\cos^2\theta - 1 \right\rangle \tag{2.4.6}$$

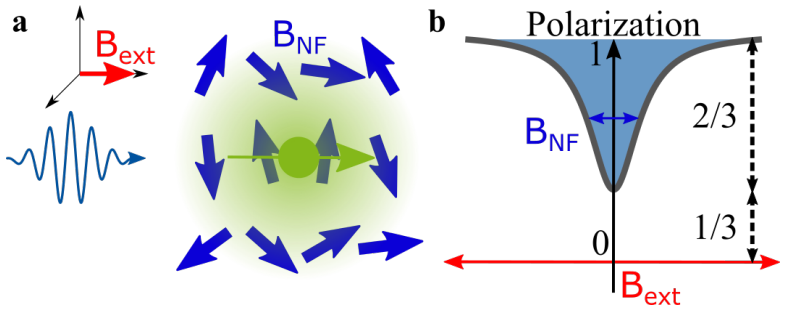

Figure 2.5.1 PRC principle. **a**, A carrier spin (green) is subject to a nuclear spin surrounding (blue) giving rise of a nuclear fluctuation field B_{NF}. In a rising magnetic field in Faraday geometry (see, light wave in respect to magnetic field direction $B_{\mathbf{ext}}$) the fluctuation field can be overcome. In a polarization recovery curve (PRC), **b**, this leads to an increase of recorded polarization. As 1/3 of B_{NF} points in the same direction as the carrier spin still the carrier spin polarization doesn't drop to zero at zero magnetic field.

where r is the carrier vector, and θ the angle between p-orbital and nuclear dipol axis, while $\langle\cdots\rangle$ stands for averaging over the carrier wavefunction.
To estimate the hyperfine constants for lead halide perovskites one needs to estimate the p- and s-type character of the carrier wavefunctions. The valence band has a high lead s-orbitals admixture (Eq. (2.1.3)), with a percentage $\approx 1/3 \ldots 1$, giving a hyperfine constant of $A_{vb} \approx 10 \ldots 100$ μeV. [Gla18; Kir21b]. The values for the hyperfine constants are given for a carrier as if it would be localized on a single nucleus.
The conduction band consists mainly of p-type lead orbitals with a small admixture (C_s) of s-halogen orbitals. The conduction band hyperfine constant calculates as weighted sum of both parts $A_{cb} = \alpha_{^{207}\mathrm{Pb}}(1 - C_s)A_{cb,p} + \alpha_{\mathrm{X}} C_s A_{cb,s}$, with α the abundance of non zero nuclear spin isotopes of lead (α_{Pb}) and the halogen (α_{X}). With $A_{cb,s} \approx 90$ μeV, $A_{cb,p} \approx 6$ μeV, $C_s \approx 0.05 \ldots 0.1$, $\alpha_{^{207}\mathrm{Pb}} = 22.1\%$ and $\alpha_{\mathrm{X}} = 100\%$, the hyperfine constants for s- and p-type interaction become of comparable quantity on the order of a few μeV. The dominance of s- or p-type contribution is difficult to distinguish but in general, the hyperfine interaction for the conduction band will be much weaker than for the valence band.

2.5 Polarization Recovery

If one polarizes the carrier spins with circular polarized light, they will be oriented along the light propagation, due to the presence of non zero nuclear spins, a permanent background of statistically oriented magnetic moments is present, see Fig. 2.5.1. Thus, even in absence of an external magnetic field a carrier spin is subject to magnetic fields. Partially, the fields will be oriented parallel to the carrier spin and partially perpendicular to it. Those which are perpendicular will lead to a spin precession or, in other words, to a mixing of spin up and spin down eigenstates. One can overcome the regime of nuclear spin fluctuations (B_{NF}) by applying a magnetic field along the carrier spin direction (Faraday geometry), $B_{\mathrm{ext}} \gg B_{\mathrm{NF}}$, pinning the carrier spin direction to the eigenstates. From the total amount of the fluctuating nuclear spins in average 1/3 will point in the direction of the carrier spin and act like a parallel magnetic field while 2/3 will be perpendicular and induce a mixing. Hence, the carrier spin

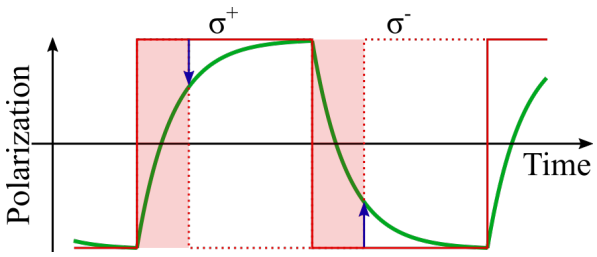

Figure 2.6.1 Spin Inertia. The spin polarization (green) follows the sequence of excitation (red), a period of σ^+ excitation is followed by a period of σ^- polarization. The spin polarization is reaching an equilibrium polarization after a certain time T_s. If the periods of excitation are shortened (red shaded area), the equilibrium polarization is not reached before the next helicity change occurs, hence a decreased polarization will be measured (see, crossing points indicated by arrows).

polarization will be 3 times higher, as a maximum, in a sufficiently strong magnetic field along the light propagation as compared to the carrier spin polarization subject to the nuclear spin fluctuations alone. The polarization recovery curve reflects this. To trace a PRC curve, the carrier spin polarization is observed while a magnetic field applied in Faraday geometry is driven up or down. A Lorentzian shaped dip is typically observed. A more complex shape can also occur, in the form of double Lorentzians (M-shape) [Smi18], but was not observed in perovskite structures in this work. The PRC is measured, see method section, at long time delays (e.g. -10 ps before the arrival of the next pump pulse) in order to avoid influences of the PRC amplitude by short living components.

2.6 Spin Inertia

If an ensemble of spins is excited with circular polarized light, a carrier spin polarization will build up. However, the build up is not instantaneous but hindered by the spin flip rate, represented by the longitudinal relaxation time T_1, $S(t) = S(1 - \exp(-t/T_1)$ with S the spin polarization. If the excitation is stopped or its polarization is inverted before the steady state spin polarization has build up, a smaller spin polarization is reached, see Fig. 2.6.1. Hence, by measuring the dependence of the spin polarization over a decreasing pump period length $1/f_m$, a measure of T_1 can be given. The recorded spin polarization signal L reads

$$|L(f_m)| = \frac{2}{\pi} \frac{n_0 |S_0|}{\sqrt{1 + (2\pi f_m T_s)^2}}, \tag{2.6.1}$$

with T_S the cutoff time and n_0 the amount of resident carriers [Hei15; Smi18]. Still, the steady state spin polarization is an equilibrium between spin relaxation and generation rate (the light intensity), $\frac{dS(t)}{dt} = \frac{S_i - S}{\tau} - \frac{S}{\tau_s}$, with S_i/τ the spin initialization rate, $-S/\tau$ the escape rate due to carrier recombination and $-S/\tau_s$ the relaxation rate, with the steady state solution $S = S_i \tau_S/(\tau_S + \tau)$. For a better approximation of the spin relaxation time $\tau_s \approx T_1$, it is sufficient to correct the experimentally observed value T_s by a term proportional to the generation rate $T_s^{-1} \approx \tau_s^{-1} + GP$, with P the power of the exciting light and G the generation rate [Hei15].

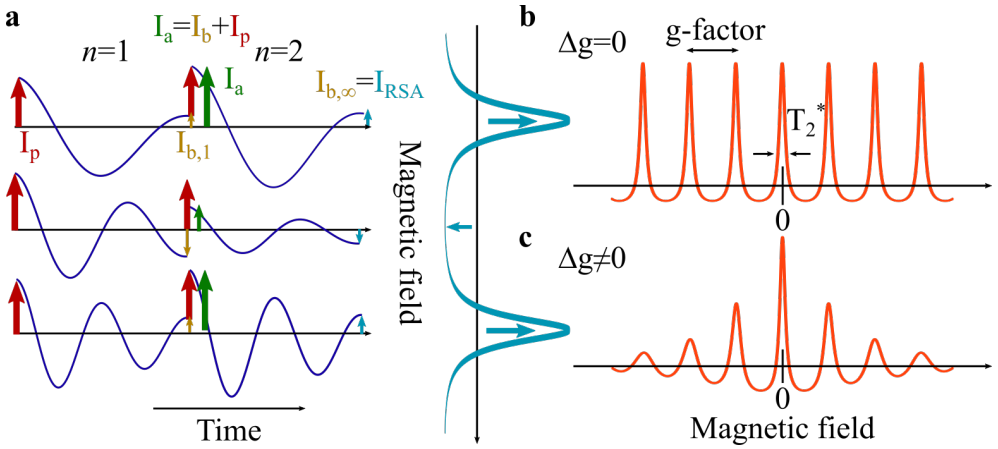

Figure 2.7.1 Resonant spin amplification. RSA build up from **a** time resolved spectra (blue curves). If time evolution of initial spin polarization by pump pulse (I_p, red arrow) prevails up to the next pulse excitation, the amount of spin polarization before pump arrival (I_b, golden arrow) adds to the signal after (I_a, green arrow). This sequence is repeated for a high number of pulses and the sum signal recorded ($I_{\mathrm{b},\infty}$ or I_RSA, turquoise). With a magnetic field scan sharp RSA peaks will be observed. **b** RSA curves for spread of g-factor zero. The peak separation is given by the carrier g-factor and the peak width determined by inverse T_2^*. **b** For non zero spread of g-factor T_2^* decreases with magnetic field, leading to a broadening of RSA peaks and decrease of amplitude.

2.7 Resonant Spin Amplification

The resonant spin amplification (RSA) is a phenomenon which is showing up if the spin relaxation times, and particular T_2^* exceeds the laser repetition rate T_R. For pulsed spin excitation the ensemble dephasing time can be such high that still a non zero spin polarization is present when the next excitation occurs. In particular this case is important to consider if a spin precession is present, so an external magnetic field in Voigt geometry is applied. For a precessing spin ensemble the upcoming excitation pulse could be either in phase with the ongoing spin precession or counter phase, which is called the phase synchronization condition (PSC). If the spin is counter phase the excitation pulse acts counter to the ongoing polarization and even a smaller amplitude than with infinite pulse separation would be observed, see Fig. 2.7.1**a** second curve. The opposite is happening for the inphase excitation, the new pulse enhances or amplifies the signal, Fig. 2.7.1**a** first and third curve. The PSC reads $\omega(B) = nT_R^{-1}$, with n an integer number. The RSA curve is a measurement of this effect. As measurement point a long time delay, see method Sec. 3.3.2, also called negative time delay, is chosen and a magnetic field, applied in Voigt geometry, scanned while the spin polarization amplitude is recorded. Thus, with increasing of the magnetic field the PSC is alternating fulfilled and unfulfilled. A series of Lorentzian shaped sharp peaks occur with fulfilment of the PSC condition. The periodicity follows the spin precession frequency change with the magnetic field, hence is a measure for the carrier g-factor. The width of the RSA peaks is a measure for the ensemble dephasing time T_2^*. The narrower the line the longer is T_2^*. If T_2^* is short the peaks will become such broad that the shape appears to be like a sinusoidal curve.

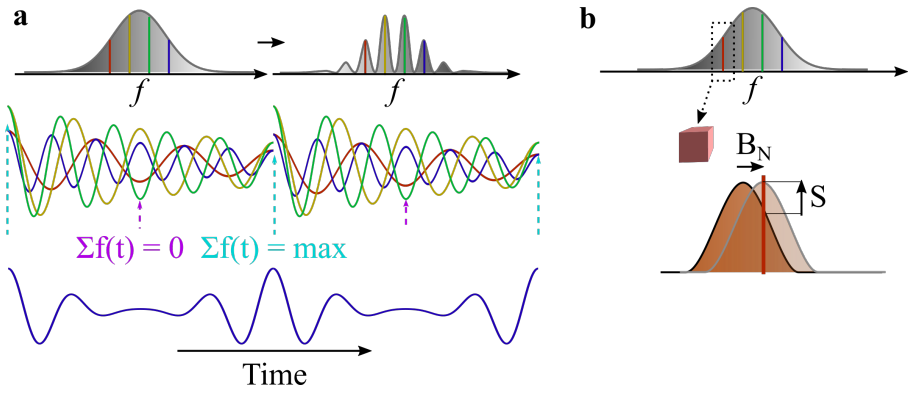

Figure 2.8.1 Spin modelocking. **a**, if in a given magnetic the distribution of Larmor frequencies (grey upper curve) consist of several frequencies multiple to inverse laser repetition rate ($1/T_\mathrm{R}$) (coloured lines), in time domain the interference of signals $\sum f(t)$ (blue bottom curve) can show after a decreasing envelope also an increase. The increase is given by constructive interference of contributing signals as sketched by superimposed individual curves above. **b** Feedback cycle of nuclear focusing. A carrier spin e.g. in a quantum dot shows a frequency which is not consumable to the modelocking frequency. However a small polarization can cause a nuclear polarization which induces an Overhauser field detuning the precession frequency closer to a mode, this causes a higher carrier spin polarization enhancing the Overhauser field build up and finally pushes the carrier spin precession onto a mode.

The RSA equation reads

$$f_\mathrm{RSA}(B) = \frac{S_0}{2\exp\left(-\frac{t}{T_2^*}\right)} \frac{\exp\left(-\frac{T_R}{T_2^*}\right)\cos\left(\omega(B)t\right) - \cos\left(\omega(B)(t+T_R)\right)}{\cosh\left(\frac{T_R}{T_2^*}\right) - \cos\left(\omega(B)T_R\right)}, \tag{2.7.1}$$

with $\omega(B) = g\mu_B B/\hbar$ [Yug12].
In case of a non zero spread of g-factor, T_2^* is magnetic field dependent, and will decrease with an increase of the external magnetic field, see Fig. 2.7.1**c**. With a simple replacement of $(T_2^*)^{-1} = (T_{2,0}^*)^{-1} + \Delta g\mu_B B/\hbar$ one can model this behaviour. In comparison of Fig. 2.7.1**b** and Fig. 2.7.1**c** only the central peak for $B = 0$ is unaffected. For increasing of the absolute magnetic field strength (independent on the magnetic field sign) the RSA peaks become broader and the RSA amplitude drops. For high fields then a close to sinusoidal dependence is found.

2.8 Spin Modelocking

Analogue to RSA, spin modelocking is an effect which can occur if the spin relaxation time exceeds the laser repetition frequency and a spin precession is present [Gre06b; Gre07]. In the spin modelocking regime however not an extremely high T_2^* is driving the presence of this effect but rather a long T_2 in combination with a high spread of g-factor, as being the cause of a short T_2^*. The decrease of T_2^* with increasing magnetic field is accompanied by a broadening of the precession frequency distribution of the ensemble. Thus in higher fields

the frequency distribution can become such high that the PSC condition is fulfilled for not only $\omega(B) = nT_R^{-1} = g\mu_B B$ but also for spins within $nT_R^{-1} = (\Delta g \pm g)\mu_B B$. While the full ensemble might be already dephased, the individual spins prevail as long as T_2 and those precession modes fulfilling the PSC will be amplified by the continuous series of pump pulses. Hence, those modes contribute with a higher amplitude. The frequency distribution of the ensemble turns from a homogeneously broadened type into a comb like distribution, see Fig. 2.8.1. In the regime of a time resolved spin polarization signal, first a decreasing signal envelope, as the ensemble dephases, followed by an increasing envelope, as more and more modes rephases, will be observed, see Fig. 2.8.1**a**.

Nuclear Induced Frequency Focussing Spin modelocking can be accompanied by the phenomenon of the nuclear induced frequency focussing. This effect is driven by a specific dynamic nuclear polarization process [Mar19; Gla12b]. As it was shown in Sec. 2.4 a spin polarization can induce a dynamic nuclear polarization, which in turn can shift the Larmor frequency of the carrier. In the regime of modelocking a feedback cycle with the DNP occurs. The DNP is proportional to the carrier spin polarization magnitude. Thus if the Larmor frequency of a carrier gets affected by an Overhauser field in such a way, that it shifts into the direction of a mode, the carrier spin polarization gets higher, causing an even stronger build up of the Overhauser field which in turn shifts it further. The mechanism is sketched in 2.8.1**b**. Note, a more elaborated description needs to take into account the optical Stark effect and leads to a slightly different description of the feedback mechanism [Car09; Kor11].

2.9 Nanocrystals

Decreasing the size of a crystal down to the size of the carrier wave functions, i.e. down to the de Broglie wavelength, the carriers get confined. With the confinement, analogue to the quantum mechanical particle in a box model, the respective energy levels lift and the wavefunctions will penetrate into the surrounding material. The latter is, for instance, important for heterostructures consisting of similar inner and confinement materials, i.e. with close chemical composition like GaAs/$In_xGa_{1-x}As$ quantum wells, whereas the carrier g-factor can be formulated as a weighted sum over both materials [Ivc05]. In this study the barrier material for nanocrystals is glass. A penetration of the carrier wavefunction will be neglected as for the absence of energetically close bands to the excited states.

2.9.1 Carrier Confinement

The lift of the energy levels for a confinement carrier follows an inverse parabolic dependence $E_c = \frac{\hbar^2\pi^2}{2\mu d^2} + E_0$, with $1/\mu = 1/m_e^* + 1/m_h^*$ exciton reduced mass and d the nanocrystal size [Ivc05]. For the presented case in this study, of all inorganic nanocrystals, reports combining structural analysis using transmission electron microscopy (TEM) together with photoluminescence spectra are considered, [Don18] ($CsPbCl_3$), [Zha20b] ($CsPbI_3$),[Kri21]($CsPbBr_3$). The data given by [Don18] are reproduced in Fig. 2.9.1 and a respective fit is performed with $E(d) = E_0 + E_c(d)$. The fit gives $E_0 = 2.367$ eV (524 nm), a reasonable value for bulk $CsPbBr_3$ crystals [Bel19], and $a = \frac{\hbar^2\pi^2}{2\mu} = 4.2358$ eV nm^2. For exemplary nanocrystals, with size of 7 nm ±1 nm, this results in $E_c = 86$ meV (66–118) meV. This fit yields a reduced

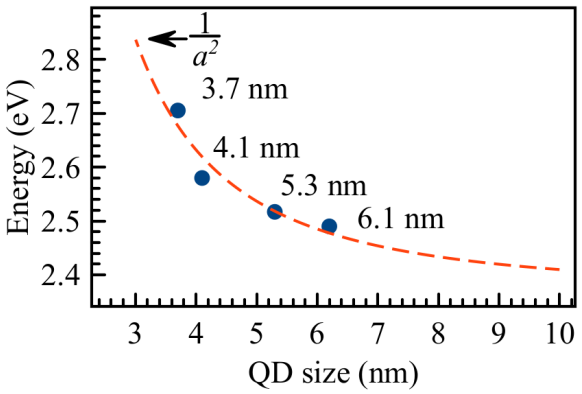

Figure 2.9.1 Confinement for $CsPbBr_3$ NCs. Energies of PL maxima versus corresponding NC size (dots), reproduced from Ref. [Don18]. Fit with inverse parabolic curve (dashed line) shows good agreement.

exciton mass of $\mu = 0.0907\mathrm{m}_e$, derived from parameter a, which is in line with the literature value of $\mu = 0.104\mathrm{m}_e$ [Miy15]. Note that this estimates does not take into account a renormalization of the exciton binding energy or change of an exciton fine structure splitting [Bay02].

As additional consequences from the confinement, the heavy and light electron band degeneracy is lifted and respective mixing with the conduction band in magnetic fields occur. A preliminary estimate by M. A. Semina, M. M. Glazov, M. O. Nestoklon and E. L. Ivchenko uses parts of the $\mathbf{k}\cdot\mathbf{p}$-Hamiltonian,

$$\langle c,+1/2|\mathcal{H}|he,+3/2\rangle = \frac{D}{\sqrt{e}}k_z(k_x+ik_y), \langle c,+1/2|\mathcal{H}|le,-1/2\rangle = \frac{\sqrt{3}D}{\sqrt{e}}k_z(k_x-ik_y) \quad (2.9.1)$$

together with its Hermitian conjugated and time reversals, with $k_{x,y,z}$ the wavevectors and D the band structure parameter for an estimate. In the presence of a magnetic field $B \parallel z$, $[k_x, k_y] = \frac{ie}{\hbar c}B_z$ do not commute and the correction of the conduction band g-factor derives approximately as

$$\delta g_e^{nc} \approx -\frac{4p^2}{3m_0E_g}\frac{E_c}{\Delta} \quad (2.9.2)$$

with E_c the confinement energy and Δ the spin orbit energy. The conduction valence band mixing term $\frac{4p^2}{3m_0E_g}$ in Eq. (2.1.8) is replaced by $\frac{4p^2}{3m_0E_g} \to \frac{4p^2}{3m_0E_g}(1-\frac{E_c}{\Delta})$. For the s-type valence band, no mixing with the heavy or light electron band is present thus the g-factor renormalizes by confinement without deviation from the universal law Eq. (2.1.8), i.e. according to the renormalized energy as sum of the band gap energy and the confinement energy $E_g \to E_g + E_c$.

3

Experimental Methods

In the methods section, the experimental apparatus will be described. First, the synthesis of the studied crystals, then its X-Ray characterisation and a detailed description of the optical setup, in terms of time resolved pump probe spectroscopy and related measurement setups are presented.

3.1 Perovskite Samples - Growth

One of the key advantages of perovskite crystals, in contrast to traditional MBE grown II-VI, III-V and IV structures, is the ease of synthesis. Two types of crystals were studied, macroscopic (bulk) single crystals and dot like, zero dimensional, nanocrystals embedded in a glass matrix.

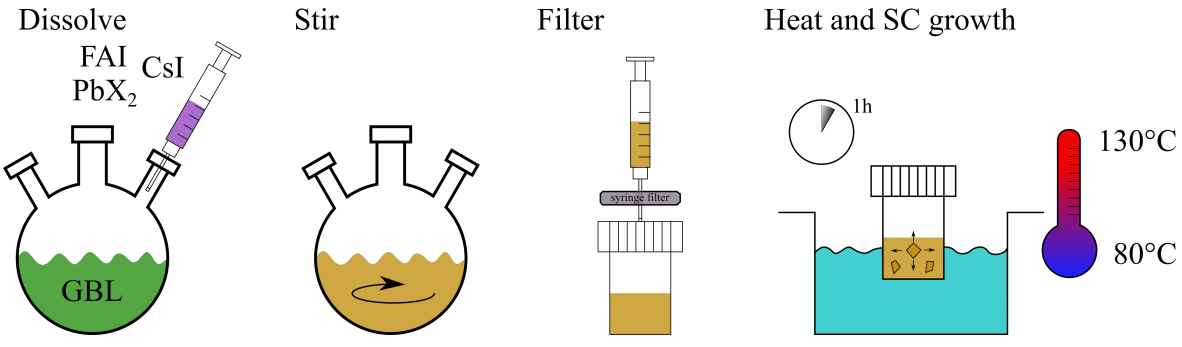

Figure 3.1.1 Single crystal sample growth The growth of single crystals follows a sequenced protocol, from left to right. First, all ingredients need to be dissolved and stirred. Next, the solution is filtered from undissolved parts. Finally, the solution is heated in a water-bath whereas the single crystals are formed.

3.1.1 Single Crystals

The basic principle of perovskite single crystal growth is the so called inverse temperature crystallization (ITC) technique, see Fig. 3.1.1. The single crystals were grown in the groups of M. Kovalenko (ETH Zürich) and V. Dyakonov (University Würzburg). In a polar solvent like γ-butyrolactone (GBL), an aprotic polar solvent, all reagents (a lead salt and a salt with the organic cation or a caesium salt) are dissolved and carefully mixed. The mixture, or precursor, is then filtered and transferred to the crystallization pot. The pot is heated in a water-bath (Bain-marie). The increase of temperature decreases the solubility product thus the perovskite crystals are formed under precipitation. A similar method, usage of an antisolvent (also reducing the solubility product), was not used for crystal synthesis in this study. In detail, small changes in the growth protocol needed to be implemented for the growth of specific crystals, which will be described in the following [Naz17; Hö21]. Note, exemplary the growth protocol for an all inorganic lead halide perovskite $CsPbBr_3$ single crystal is additional given, though the observation of spin dynamics will be not treated explicit in this study, and only refereed on it in Ch. 6 indirectly.

3.1.1.1 $FA_{0.9}Cs_{0.1}PbI_{2.8}Br_{0.2}$ Crystals

The growth of α-phase $FA_{0.9}Cs_{0.1}PbI_{2.8}Br_{0.2}$ is discussed in detail in Ref. [Naz17]. Basically, all salts, CsI, FAI, PbI_2, and $PbBr_2$, are mixed, proceeded as previously described and crystallization was obtained at a temperature of 130°C. The as grown crystals are of deep black colour with a structural size of $\approx 2 \times 3 \times 2$ mm^3. Although the outer sides show rhombic and trapezoid shape, the crystal is of cubic symmetry. The facets correspond to inclined directions within the cubic unit cell, diagonal [110] etc. A figure of the sample is shown in Fig. 3.1.2.

3.1.1.2 $MAPbI_3$ Crystals

The ITC recipe was modified for the growth of $MAPbI_3$. Here, the reacting salts were desolved in a mixture of GBL with an addition of a mixture of alcohols. The admixture of 1-propanol, 1-butanol, 1-pentanol or 1-hexanol alcohols allows one the control of the solvent polarity and, consequently, a lowering of the crystallization temperature. As a drawback, a longer dissolving time of the salts may be present, though not studied in detail. The growth of $MAPbI_3$ single crystals was obtained at a temperature of 85°C. The crystal shape is comparable to $FA_{0.9}Cs_{0.1}PbBr_{0.2}I_{2.8}$, showing mainly rhombic and trapezoid facets. At room temperature $MAPbI_3$ exhibits a tetragonal phase, while at the crystallization temperature, $MAPbI_3$ has a cubic phase. Additional X-ray characterisation measurements are presented in the XRD Sec. 3.2.

3.1.1.3 $CsPbBr_3$ Crystals

For the growth of $CsPbBr_3$ crystals, an ITC receipt as described in Ref. [Dir16] was used. Here, first the salts, CsBr and $PbBr_2$, were dissolved in an aprotic polar solvent, dimethyl sulfoxide. Into the precursor, a mixture of cyclohexanol and N,N-dimethylformamide was given, both also being aprotic solvents. The crystallization occurs at 105°C. In the post

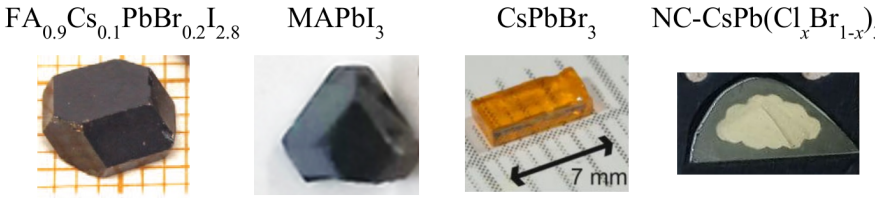

Figure 3.1.2 The samples. From left to right, three single crystals, the fourth nanocrystals (NC).

processing, the crystals were not directly filtered and cleaned but put into a 100 °C warm N,N-dimethylformamide bath and slowly cooled down to 50 °C. The resulting crystals are of cuboid shape with a side length $\approx 3 \times 2 \times 7$ mm^3, whereas the longest side can be identified as c-axis and the both other as $[\bar{1}10]$ and $[110]$ sides [Fen20]. $CsPbBr_3$ exhibits orthorhombic phase already at room temperature.

3.1.2 $CsPb(Cl_xBr_{(1-x)})_3$ Perovskite Nanocrystals Embedded in a Glass Matrix

Nanocrystals embedded in a glass matrix are typically grown in two separate ways [Kol21; Gle13]. One way, is to grow them in a solid glass piece, by phase segregation with above glass transition temperature treatment $(T_g)^*$, i.e. heating of the glass to 400–500°C. Second, to have an supersaturated glass melt, from which nanocrystals are directly formed at the glass quenching process. In this case, the quenching speed and thus the heat transfer is the control parameter for the crystal size. The density of the obtained NCs with the use of post quench heat treatment (first method) is low, therefore the latter method was used.

The synthesis process is sketched in Fig. 3.1.3. First, all ingredients, listed in table 3.1.1, are mixed and heated together in a glassy carbon crucible, at a temperatures of 1000–1050°C. For an amount of 50 g melt, this takes about 20 min. The melt is then cast on a cold glassy carbon plate and immediately pressed to form a glass with a thickness of about 2 mm. The low viscosity of the fluorophosphate glass melt, over a wide temperature range, is favourable to form a thin plate. The presence of nanocrystals can be directly confirmed by the colour of the glass. The glass consists of $60Ba(PO_3)_2 - 15NaPO_3 - 12AlF_3 - 1Ga_2O_3 - 4Cs_2O - 8PbF_2$ (mol%) with a doping of 16 mol% NaCl, 3.4 mol% $BaBr_2$. A nanocrystal size of about 7 nm was confirmed via X-Ray and luminescence analysis, Sec. 3.2.5.2. The shape of the formed

*Not to mix with melting temperature, see e.g. polystyrene thermoplast, which is solid at room temperature, becomes flexible at 100°C, and will melt at higher temperatures.

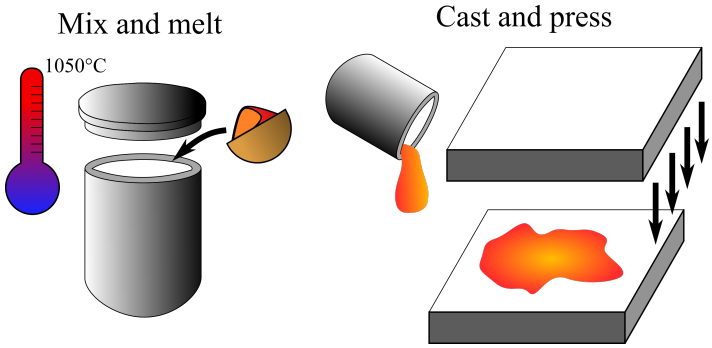

Figure 3.1.3 Proceeding of all inorganic lead halide perovskite nanocrystals embedded in a glass matrix. In essence, the ingredients are mixed by melting, followed by a rapid cast, press procedure on a cold plate vice.

Reactant	Mass
$CsCO_3$	2.0 g
$BaBr_2$	0.5 g
NaCl	0.5 g
PbF_2	1.0 g

Table 3.1.1 Ingredients for the growth of $CsPb(Cl_xBr_{(1-x)})_3$ perovskite nanocrystals. With $BaBr_2$ 297.14 g/mol and NaCl 58.44 g/mol, an initial ratio of 28% Br and 72% Cl is present in the solution. The actual NC composition may differ due to the formation of the initial salts ($BaBr_2$ and NaCl instead forming perovskite), Cl and Br halogens dissolved in the fluorophosphate glass or evaporation.

nanocrystals is assumed to be pseudo spheric, though experimental confirmation is difficult. For the specific samples used in this study no TEM studies were performed. As reference, reports for comparable melt quenched samples, using high resolution transmission electron microscopy (HRTEM) to resolve the nanocrystal structure, can be considered [Ary21; Liu19a; Xu21; Lon21]. In these works, spherical and flake like shapes were observed. With an average nanocrystal size of 7 nm, as studied in this work, the deviations from spherical shape are assumed to be small. A sphere of 7 nm diameters corresponds to an diameter of 14 unit cells, thus a typical size distribution of 10 % would result only in a change of ± 1 unit cell.

The growth of perovskite nanocrystals could be performed, in principle, analogue to the growth of bulk single crystals in a wet chemistry process. In this case, to prevent the formation of bulk crystals and limiting the growth to nanocrystal size, additional chemicals would be needed to be introduced to the precursor [Yin05]. However, nanocrystals grown in such way, colloidal nanocrystals, differ strongly from their bulk counterparts and melt quenched nanocrystals. As in general in nanocrystals, the ratio of volume to surface shrinks in favour to a higher importance of the surface, the added chemicals for growth of colloidal nanocrystals become important. Often the surface of colloidal nanocrystals is covered by ligands. Further, the colloidal nanocrystals are either dispersed in a liquid or deposited on a glass carrier. In the first situation, the floating particles will scatter among each other and in the case of a deposition on a glass carrier, either in a very diluted case, only a coverage of a single layer of nanocrystals is achieved or more likely the nanocrystals may stack and thus could interact with each other. Floating particles, a single layer or stacked layer deposition are all unfavourable for this studies. Last the chemical stability of colloidal nanocrystals is poor.

Hence, the choice was made to use nanocrystals embedded in glass matrix. Nanocrystals in glass exhibit a passivated surface, are (nearly) homogeneously diluted in the glass matrix, i.e. each nanocrystal is well separated from the next neighbours and are chemical stable due to perfect encapsulation.

3.1.3 Perovskite Degradation Channels

Degradation of the perovskite single crystals is a major threat and the main issue to be solved before a commercial roll out could be done. Several degradation channels have been identified. First, the perovskite crystals degrade rapidly in contact with water, like in humidity in ambient condition. Water takes the role of a catalyst for the formation of PbX_2, mainly shown for the formation of PbI_2 for hybrid organic lead halide iodine crystals [Fro14]. To prevent this process, it would be needed to encapsulate the crystals. Several approaches, like

polymer encapsulation, glass barriers etc. have been proposed and implemented, as for NCs. The discussion of pros and cons is out of scope in this work. In this work, the bulk single crystals were stored under vacuum and placed in an inert pure helium atmosphere for optical measurements, which even act as cold trap, ensuring that no water could come into contact with the sample. Within a measurement session, of approximately 1-2 weeks time, no notable degradation was obtained. However, the exchange of the samples from the cryostat gave an inevitable contact of the cold sample to ambient air, leading to a small condensation of water on the sample surface.
A further degradation channel is the ion migration [Mus21]. Especially for hybrid organic lead halide perovskites, this is the next major concern [Wil21]. In this case, the hydrogen atoms of the organic molecule may react or scatter ballistically with different sites of the crystals lattice [Har18]. The process of ion migration, and chemical activity of the organic cation, is assumed to be hindered at low temperatures and no significant changes within time frame of the measurement periods were found.
In sum the results of the mentioned degradation processes can be ruled out to influence the results obtained in this work. In the water catalyst process, yellow PbI_2 or its halogen analogues PbX_2 are formed. PbX_2 has a higher band gap as the corresponding perovskite and would be a transparent layer in the measurements. As the result of the ion migration, additional vacancies and atom interstitials might be present. The vacancies and interstitials are of larger concern, but differ in their energy levels in respect to the, resonantly excited, exciton. Further the energy levels of the defects should mostly be located outside of the band gap [Bra17].

3.2 X-Ray Characterisation

3.2.1 Basic Principle

X-Ray diffraction (XRD) is a method to measure the lattice periodicity. In a nutshell, the lattice acts as optical grating for the X-Ray beam and under certain conditions, one obtains a constructive or destructive interference, Bragg reflexes. The X-Ray diffraction scheme is shown in Fig. 3.2.1. The optical paths length, for the X-Ray beam reflected on the surface and the one on the next layer of atoms, differ by $\Delta s = 2a_0 \sin(\theta)$, with a_0 the lattice constant and θ the angle of incidence. However, if Δs equals a full wavelength period λ_X, the in-phase

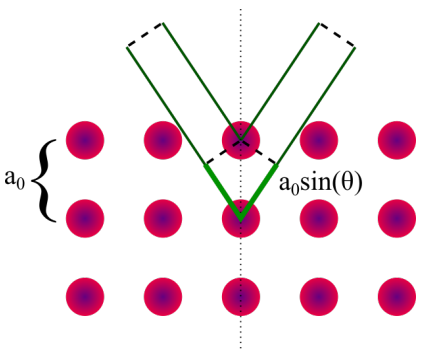

Figure 3.2.1 Sketch of XRD principle. The X-RAY beam (green) is reflected on the crystal surface and beneath laying periodic layers, separated by the lattice constant a_0, (red balls) under normal incidence (dashed line). Constructive interference occurs if the path difference of the scattered beam on surface and layer below equals a multiple of the X-ray wavelength λ_X.

oscillation is restored and one obtains constructive interference,

$$n\lambda_X = 2a_0 \sin(\theta). \tag{3.2.1}$$

In the experiment, a wavelength of $\lambda = 0.154$ nm from copper (Cu K-α) emission is used typically and the angle is scanned.

3.2.2 Powder and Single Crystal XRD

The case given above is suitable to measure the lattice periodicity a_0 for a single crystal, Fig. 3.2.2**a**. In the experiment the X-Ray source and X-Ray detector are rotated together with an opening angle of 2θ towards the sample mount, e.g. the sample surface. If the source is rotated clockwise the detector is rotated counter clockwise by the same amount and vice versa. This configuration allows only to measure crystallographic planes, for which the plane normal, is centred between 2θ. If the crystal has several symmetry directions, e.g. the diagonal planes in Fig. 3.2.2**b**, the plane normal $s\prime$, does not coincide with the rotation centre s, and the constructive interference of the X-Ray beam on this plane would fall outside of 2θ. If to reorient the crystal, Fig. 3.2.2**c**, with the plane normal parallel to the rotation centre $s\prime = s$, the issue is solved. To gain information of all crystal symmetry axis, one would need to manually scan all possible crystal directions. This might be very time consuming. A common method to gain information of all possible crystal orientations at once, is to use a powder of the given single crystal, see Fig. 3.2.2**d**. In a powder, all possible crystal directions, are given at once and one can always find a grain for which the parallelism of crystal symmetry plane and the rotation centre is realized. One should note, that a polycrystalline bulk sample gives, an XRD pattern comparable to the powder XRD spectrum. Thus, the amount of XRD lines obtained for a bulk crystal, in comparison to its powder XRD spectrum, is a good indicator to characterise the amount of the present domains. Again, one should find only peaks of a single plane in a single crystal.

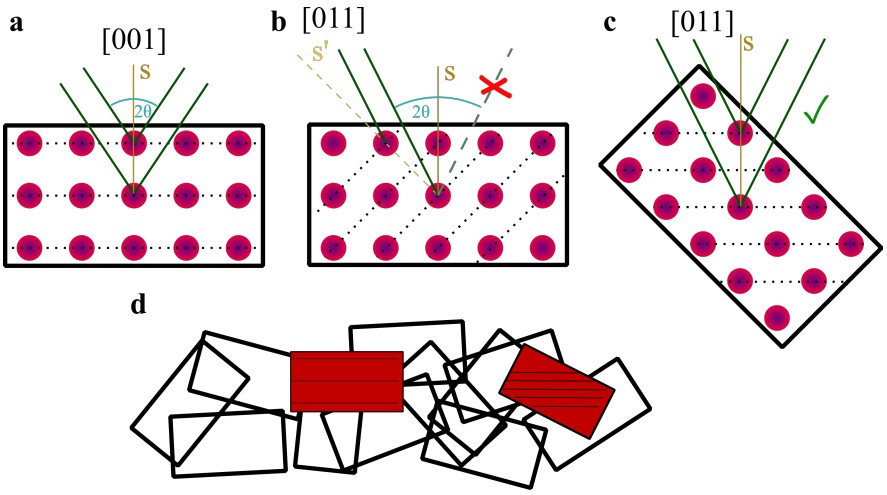

Figure 3.2.2 X-Ray Diffraction. **a-c**, single crystal XRD. **a**, For the [001] direction constructive interference occurs according Eq. (3.2.1). **b**, for the diagonal plane, with plane normal s' =[011], a constructive interference falls outside of opening angle 2θ. **c**, tilting of the crystal resolves this issue. **d**, in powder, all possible orientations are realized at once.

3.2.3 Nanocrystal Size

The line width of XRD measurements is inverse proportional to the crystal size, i.e. for nanocrystals, a significant broadening is observed. While the XRD line width for single crystals is described by the Laue equation, instead for nanocrystals the Scherrer equation is to be used [Sch12]

$$d = \frac{K\lambda}{\beta cos(\theta)}, \tag{3.2.2}$$

with d the average nanocrystal size, K a dimensionless shape factor with a value close to unity and β the full width half maximum of the XRD peak in radian.

3.2.4 Rocking Curve

The Rocking scan technique is a tool to analyse the amount of polycrystalline domains, which converges for our single crystals in a single domain. It is a subdiscipline of the XRD topography. In fact, it is an integral topography, as the topological information is accumulated over the X-Ray beam size, which may cover the full crystal surface. In the rocking curve measurement, the diffraction angle is kept constant, at a Bragg reflex, and the sample is rotated instead. An angular line broadening exceeding the natural X-Ray line width (also called Prins-Darwin width [Dar14]) will occur, if the crystal deviates from a perfect single crystal [Mas14]. For X-Rays, the Darwin-width is typically about 1-10 arc sec. The rocking scan is sensitive to various crystal imperfections like voids, phase boundaries, cracks, stacking faults, dislocation, point defects, strain etc.

3.2.5 XRD Characterisation of Perovskite Crystals

3.2.5.1 $MAPbI_3$ Single Crystal

An X-Ray characterisation of the used $MAPbI_3$ single crystal was performed by Höecker *et al.* [Hö21]. In their work, powder XRD, single crystal XRD and a rocking scan was performed.

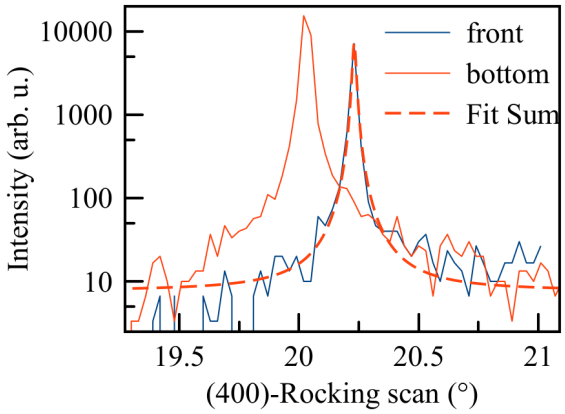

Figure 3.2.3 Rocking scan of the studied $MAPbI_3$ sample at room temperature at (400) Bragg reflex, measured for front (blue) and bottom (red) facet. The bottom facet had contact with the curved beaker base while growing, resulting in a slightly broader peak. Data provided by J. Höcker, University Würzburg.

The rocking scan, Fig. 3.2.3, shows an inhomogeneous line width of 0.016° (57.6 arc sec) for the front and 0.034° (122.4 arc sec) for the bottom facet, where in the Lorentzian fit, the amplitude was fixed to the maximum amplitude of the signal (7240 counts for the front and 19500 counts for the bottom facet). The inhomogeneous line profile, in contrast to a homogeneous, and a narrow line width, confirms that the crystal consist of a single domain. The powder XRD spectrum is not reproduced here and can be found in [Hö21]. It confirms a tetragonal phase for $MAPbI_3$ at room temperature, with $a = b = 0.893$ nm $\neq c = 1.25$ nm. The powder XRD measurement was used as a reference for the angle and the plane assignment of the single crystal measurements.

In the single crystal X-Ray characterisation, the front facet was measured. The scan was only performed in small angle areas close to the predicted peak positions, to keep the exposure time short and a potential damaging of the crystal small. A set of four peaks at $\theta = 19.89°, 40.44°, 62.46°$ and $87.44°$ was found. For these angles, a simulation of XRD peaks in tetragonal $MAPbI_3$ predicts the presence for multiples of the (002) and (112) plane peaks in the vicinity. Note, Miller indices written in square brackets denote a crystallographic direction, while round brackets denote a plane. In comparison of the single crystal measurement, with the powder XRD spectrum, in which distinguishable peaks for the [224] and [400] direction were found, while those peaks for the [112] and [200] direction coincide, leads to the conclusion of a single crystal orientation to match best with the [200] direction. For the following analysis in this study, a [200] orientation of the single crystal is assumed. Still, for completeness, a short discussion of possible concerns should be given.

Doubts concerning the crystal orientation arise, if to compare the given analysis with literature and simulated data. An initial review of the literature, including the reports [Din18; Din17; Lv17; Din16; Lia15; Dan14], is supportive towards the identification of the front facet normal pointing along the [200] direction. Special attention should be taken towards the reports [Dan14; Din16], where the difficulty to distinguish between the two facets, is shown. Another, more theoretically inspired, analysis is presented in Fig. 3.2.4. The single crystal XRD data is compared to a simulated spectrum, obtained with lattice constants given by [Wal20]. In this case, a slightly better separation of the peaks is given. First, the simulation shows an increasing separation between the n-(112) and the n-(200) plane peak with rising integer

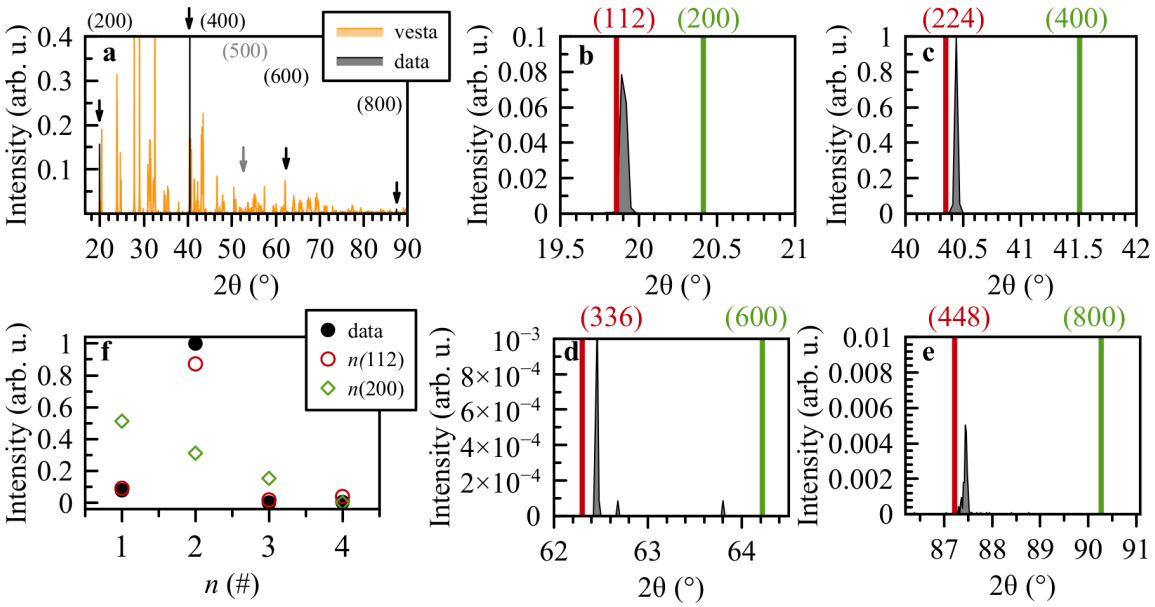

Figure 3.2.4 XRD of $MAPbI_3$. **a**, XRD spectra of the studied $MAPbI_3$ sample at room temperature compared with XRD simulation for tetragonal $MAPbI_3$ via program vesta. **b**–**e** Narrow angle zoom for peaks indicated by arrows in **a**. Position of XRD data (blacked filled curve) is compared with multiple of (112) [red] and (200) [green] plane. **f** Dependence of measured peak intensity (black dots) extracted from **a**–**e** versus peak number n. Red dots and green diamonds give calculated qualitative peak dependence of respective peaks. For $n(200)$ plane a constant drop is expected, for $n(112)$ an increase followed by a drop.

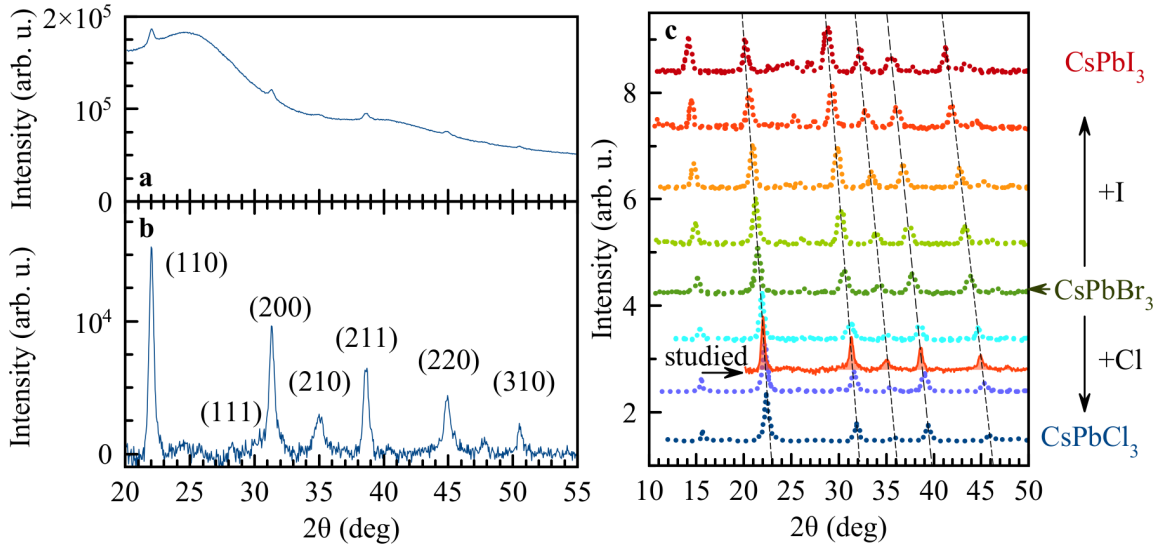

Figure 3.2.5 $CsPb(Cl,Br)_3$ NCs XRD spectrum. **a**, raw XRD spectrum. Measured at room temperature. **b**, XRD spectrum with subtracted background. **c**, Comparison of the XRD spectrum for the studied sample with literature data from Ref. [Ned15] for perovskite NCs grown by colloidal chemistry.

number n. While for $n = 1$, the separation is below 0.5°, it reaches 3° for $n = 4$, see 3.2.4 **b**–**e**. Also, the simulation predicts a small non zero peak for the (500) plane at 52.59°, while no corresponding peak from the (112) plane would be present. Unfortunately, this angle was not measured, see Fig. 3.2.4**a**. Further, the simulation shows a remarkable angular overlap of the n-(112) plane peaks and the measured values. Lastly, the simulation predicts a monotonic decrease of the peak amplitude with increasing n for the [200] direction and a non-monotonic hill like behaviour for n-[112] direction, Fig. 3.2.4**d**. The observed amplitude behaviour matches perfectly the amplitude prediction for the n-(112) planes. However, the XRD peak amplitude is hard to predict and is strongly influenced by the real realization of the carrier orbitals, which may differ significantly form the simulation. The smooth decrease of the amplitude for the [200]-direction was also not observed for any powder XRD spectra in literature.

3.2.5.2 Nanocrystals

The precipitation of NCs in the glass matrix was identified using a Rigaku X-Ray diffractometer with a wavelength of $\lambda = 0.154$ nm (Copper K-α). Two parameters will be accessed via the XRD: the lattice constant, as a measure of the Cl/Br ratio, and the NC size. The lattice constant was extracted explicitly, and compared with other XRD data. In Fig. 3.2.5c, it can be seen, that the XRD data for the sample used in this study falls in between the data for $CsPbBr_3$ and $CsPbCl_3$ NCs grown by colloidal chemistry [Ned15]. It reproduces well the peak behaviour of the 35° peak (Fig. 3.2.5b), which is increasing in amplitude for a higher Br and decreasing for a higher Cl content.

The planes are labelled according to Ref. [Kir19]. It should be noted that the positions of all

characteristic peaks in the range of the angles $2\theta = 20 - 35°$ for the orthorhombic $CsPbBr_3$ and the cubic $CsPbCl_3$ phases effectively coincide and cannot be used to identify the crystal phase of the nanocrystals due to broadening of signals, being characteristic for small nanocrystal sizes. The main difference between the X-Ray diffraction patterns of the perovskite crystals in the cubic and orthorhombic phases is the position of the peaks in the range of angles $37 - 55°$. The peaks at an angle 39.3° (211) and 45.4° (220) are characteristic for $CsPbCl_3$ in the cubic phase. If the orthorhombic phase of $CsPbBr_3$ is formed, these peaks should be shifted towards 43.70° (224) and 37.60° (312). The main argument in favour of the cubic phase in the present NC sample is the presence of the peak at 51.5° (310) which is absent in the orthorhombic phase. Further, one can see that the XRD spectrum shows a comparable peak structure as the powder XRD spectrum of colloidal grown NCs, thus a nearly random orientation of the NC in the glass matrix can be assumed.

The NC size was estimated via the Scherrer equation, Eq. (3.2.2), via the XRD peak at 38.7°. With the given parameters, a dimensionless shape factor $K = 0.9$, $\lambda = 0.154$ nm, FWHM $\beta = 0.012$ rad, and $\theta = 19.35°$ ($\cos\theta = 0.9455$), a NC size of $d = 7 \pm 1$ nm is evaluated.

3.3 Optical Measurements

All measurements were carried out with the crystals placed in an inert atmosphere and mostly in a low temperature regime. For this purpose, the samples were placed in a helium cryostat equipped with superconducting magnets. Two different cryostat designs were used. One with a single solenoid and the other with 3 pairs of superconducting magnets. For temperatures, from room temperature down to 5 K, the samples were cooled down with helium gas, while for 1.6 K, the crystals were immersed in superfluid helium. The single solenoid cryostat can provide magnetic fields of up to 8 T, in either Voigt or Faraday geometry, according to the choice of the optical axis window. In Faraday geometry, the magnetic field points along the optical axis while in Voigt geometry, the magnetic field is set perpendicular to it. The other cryostat is equipped with a set of 3 perpendicular magnet pairs, with individual drivers, and it thus allows one to create a magnetic field in any spatial direction. The total magnetic field value, $B = \sqrt{B_x^2 + B_y^2 + B_z^2}$, is restricted to 3 T. In the following, the cryostats are named by its magnet specifics, so 8 T or 3D magnet. For the 3D magnet, the typical focal distance from outside the cryostat to the sample is 500 mm while for the 8 T magnet, it amounts to 250 mm. A typical laser spot on the sample is ocused to a diameter of 100 μm (3D magnet) or 50 μm (8 T magnet)..

In this work, the optical axis is defined as z-axis which lays in the horizontal plane. In the plane perpendicular to the z-axis, the vertical direction is defined as y-axis and the one in the horizontal plane as x-axis. The angle between the z and x-axis is defined as θ and the angle between z and y as φ. The zero angle axis $\theta = \varphi = 0°$ points along the z-axis. A magnetic field applied along the z-axis refers to the Faraday geometry and, if not stated otherwise, for the Voigt geometry the magnetic field is oriented along the x-axis. An axis cross, as used in the g-factor anisotropy measurements, is sketched in the pump probe setup description, Fig. 3.3.2.

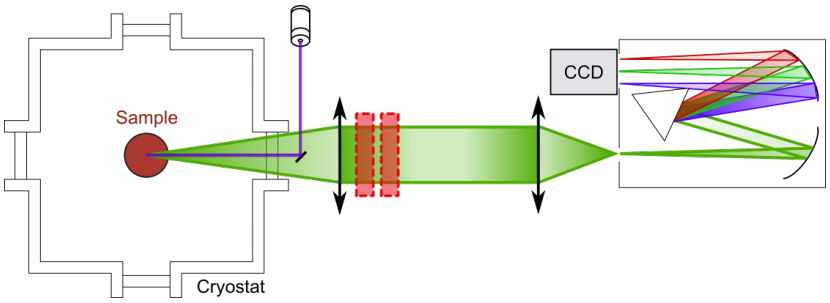

Figure 3.3.1 Illustration of PL setup. The sample (red) is placed into a cryostat (black frame) and illuminated by a laser beam for a PL spectrum or a halogen white light lamp for reflectivity (purple beam). The emitted or reflected light from the sample (green), passes several cryostat windows and is collimated by a lens (double arrow). After the first lens, polarization optics (typically a $\lambda/4$ retarder together with a Glan Prism) can be placed (red dashed squares). Note, if to use a motorized mount for $\lambda/4$, a high distance to the cryostat should be chosen to ensure function if a magnetic field is applied. Afterwards, the emitted light is focused by a lens onto the entrance slit of the monochromator. Inside the monochromator, the light is collimated onto a reflection grating and afterwards focused on a peltier cooled charge-coupled device (CCD) camera array.

3.3.1 Photoluminescence and Reflectivity

The photoluminescence (PL) and reflectivity measurements were performed according to the scheme shown in Fig. 3.3.1. The samples were exited either by a cw laser (the purple beam in Fig. 3.3.1), with an energy higher than the estimated band gap, or, for the reflectivity measurements, with a white light source (typically a [gooseneck] halogen lamp). The emitted or reflected light is collected by a lens and collimated [†]. If the polarization of the PL or reflection spectrum is of interest, a $\lambda/4$ or $\lambda/2$ retarder plate followed by a Glan prism, were placed after the collecting lens. After this, the light is focused onto the entrance slit of a monochromatator, in Czerny–Turner design. If not stated otherwise, a monochromator with a dispersion length of 0.5 m was used. Inside the monochromator, the light is directed via focusing mirrors onto a diffraction grating, dispersing it into its colours. The first order of interference is collected by a focusing mirror and directed towards a peltier cooled charged coupled device (CCD) array.
For measurements of the nanocrystals, a back illumination instead of a front illumination, with the whitelight source (giving a transmission spectrum) or a cw-laser (for PL), was used. The whitelight back illumination allowed one further an easy reference measurement of the whitelight spectrum, maintaining the same optical path, with removed sample. For practical reasons, most of the times the collected light of the sample was not focused directly onto the monochromator entrance slit but guided via a 200 μm optical fiber to the monochromator. Last, the first collimating lens could be placed also out of focus, giving an intermediate image. In this case, an additional lens was used, with the focus set on the intermediate image, to collimate the light.

[†]for adjustment, a monocular can be used

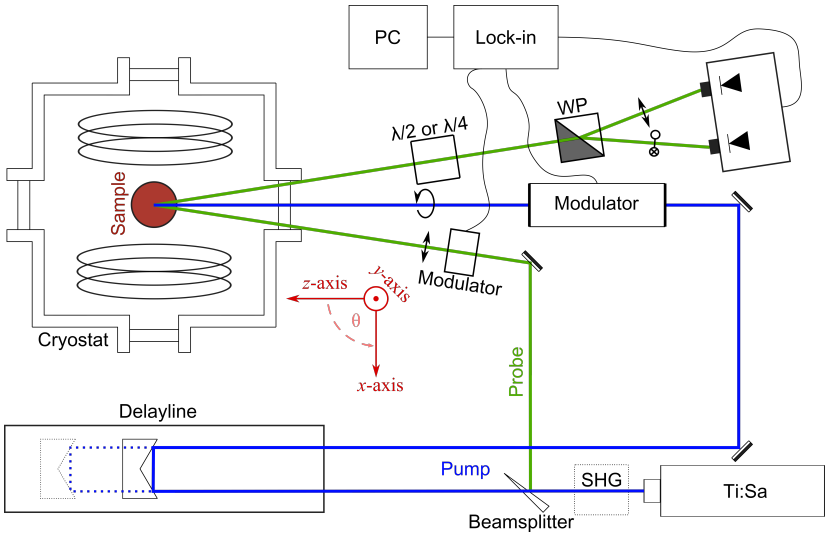

Figure 3.3.2 Time resolved pump and probe setup. Pump and probe (PP) setup is shown here for Kerr spectroscopy. For Faraday spectroscopy and time resolved differential reflection and transmission measurements, the detection arm needs to be replaced as given in text Sec. 3.3.2.6. The PP setup is fed by a ps-pulsed Ti:Sa laser system. If needed, the laser output can be further frequency doubled by a second harmonic generation (SHG) system with a beta-barium borate crystal (closed boxed system). The laser beam is further directed via a beamsplitter, separating it into pump- (blue) and probe- (green) beam. After passing a 1 m mechanical delay line, the pump beam is brought to a modulator stage (typically resulting in a helicity modulated circular polarization) and then directed towards the sample. The probe beam is directed via a modulator, giving an amplitude modulation of a linear polarized beam, to the sample. The reflected probe beam passes a polarization separation stage (retarder [Kerr ellipticity $\lambda/4$ or Kerr rotation $\lambda/2$] plus Wollaston prism) and further detected by a balanced photo diode (BPD). The signal of BPD and the modulators is given to a Lock-In amplifier.

3.3.1.1 Photoluminescence excitation

To analyse the specific coupling of an emission line towards the excitation energy, e.g. through resonant excitation of a coupled energy level, one can fix the recorded wavelength and measure the detected signal strength in dependence of the excitation wavelength. For this purpose, it is needed to suppress the detection of stray light of the exciting laser. This can be achieved, either by crossed polarization of the excitation laser towards the detected polarization, by usage of a bandpass filter or by narrowing the recorded wavelength region by replacing the CCD at the monochromator output with a narrow slit in combination with a diode or photomultiplier tube. The latter approach is typically used. Further, a spectrally tunable laser system for the excitation is needed. A cw titanium-sapphire (Ti:Sa) laser was used.

3.3.2 Time Resolved Pump-Probe Kerr and Faraday Spectroscopy

With a time resolved pump probe setup, ultra fast processes can be measured [Yak08]. In a pump probe setup, two laser beams are used, one for excitation and the second for read out. To gain the temporal information, pulsed lasers are employed and the excitation and read out

pulses are delayed in respect to each other. The realization of a time resolved pump probe setup is shown in Fig. 3.3.2.
A titanium-sapphire laser with a pulse repetition rate of $T_{\mathrm{R}} = 76$ MHz (13.2 ns) and a pulse duration of ≈ 2 ps is used. The Ti:Sa laser can be tuned in the range of $700 - 980$ nm ($1.265 - 1.771$ eV) and can be frequency doubled with the use of second harmonic generation (SHG) in a non-linear β barium borate (BBO) crystal. In the degenerate pump probe scheme, both pump and probe beams are generated by the same laser source. The laser beam was split by a wedged beam splitter, with a ratio of 9:1, pump and probe. The pump beam is guided via a 1 m mechanical delay line.

The delay line is equipped with a retro reflector giving a full time delay span of 6.6 ns (2×1 m $/c$ with c being the speed of light). Potentially, the delay line path can be doubled with an additional retro reflector placed at the entrance of the delay line, for a full extension of $T_R = 13.2$ ns. Afterwards the pump beam is polarized with the use of a photo elastic modulator (PEM), an electro optical modulator (EOM), or a set of Glan prism plus $\lambda/4$ retarder (used together with a chopper), see Sec. 3.3.2.2.

The probe beam is essentially linear polarized, and depending on the amount of stray light collected from the sample, either not modulated or amplitude modulated, see Sec. 3.3.2.2.

The angle of incidence of the pump and probe beams is set to a few degrees, allowing easy spatial separation of the reflected pump and probe beams after reflection (or transmission) from (through) the sample. The polarization of the reflected (or transmitted) probe beam is analysed, named Kerr (or Faraday) effect by a balanced photo diode. The Faraday and Kerr effect will be discussed in Sec. 3.3.2.3. The modulation of the pump and probe beam are demodulated via Lock-In technique. In essence, the signal is multiplied with the modulation frequencies, returning the constant measurement signal $A_{\mathrm{signal}}(\omega_1, \omega_2) \times \cos(\omega_1) \times \cos(\omega_2) = A_{\mathrm{Signal,DC}}$. To compensate different signal propagation delays, the multiplication of the signal with reference signals need to be done with an appropriate phase. The DC signal is additionally filtered by a lowpass filter (LP) reducing further noise components and giving a integration of the signal according to the chosen time constant ($1/f_{\mathrm{LP}} \approx 100$ ms).

3.3.2.1 Laser Pulses

The Ti:Sa laser system used for the pump and probe experiments has a pulse duration of about 2 ps. As a check, one can measure the spectral width of a pulse (FWHM), see Fig. 3.3.3. From the uncertainty principle the pulse duration is given by $\delta\tau\delta\nu = 1/2$ and $\delta\lambda = \lambda^2\delta\nu/c$ thus

$$\delta\tau = \frac{\lambda^2}{2c \cdot \delta\lambda}. \tag{3.3.1}$$

For an exemplary pulse, presented in Fig. 3.3.3, a fit with a Gaussian profile gives a central wavelength of $\lambda = 757.5$ nm and a full width half maximum $\delta\lambda = 0.45$ nm, which corresponds to $\delta\tau = 1.9$ ps.

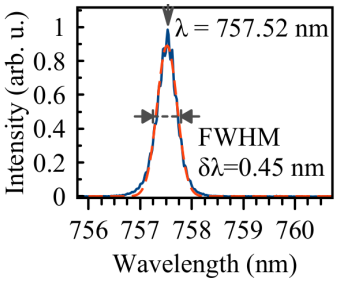

Figure 3.3.3 Example of spectrum of used laser pulses, e.g. used for $MAPbI_3$ bulk crystals. The FWHM is mainly determined by the time duration of a laser pulse, here 1.9 ps.

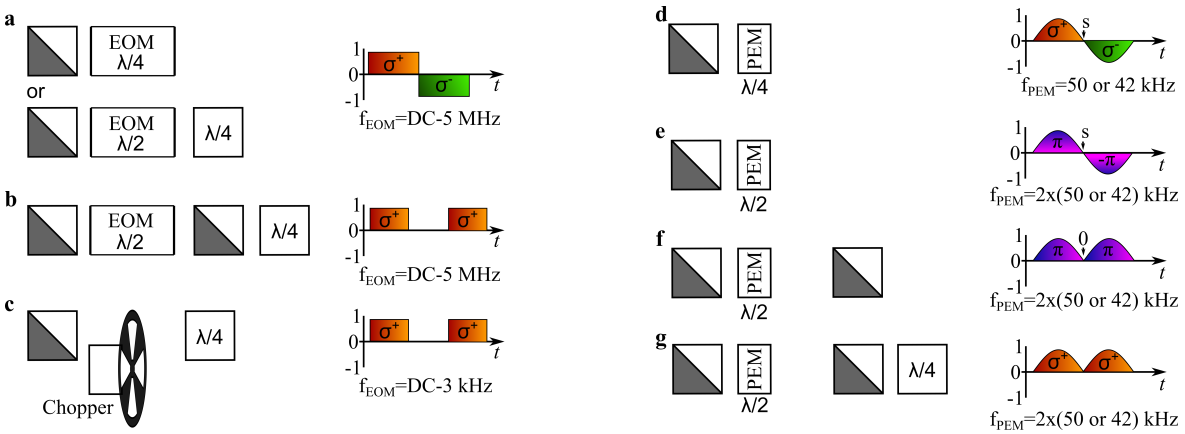

Figure 3.3.4 Configurations of different modulators. a–b, usage of an EOM gives a square like laser beam modulation in **a** full σ^+ to σ^- regime and **b** to one polarization, here σ^+, to zero. Note, typically its more stable to use the EOM in $\lambda/2$ regime and to place a $\lambda/4$ afterwards in order to get a helicity modulated beam. **c**, the chopper gives a square type amplitude modulation between one helicity, here σ^+, to zero amplitude. **d–g**, modulation with PEM gives a sinusoidal signal. **d**, in helicity modulation the PEM modulates between σ^+ and σ^- in maxima with undergoing a change to linear polarization in saddle points. **e**, in $\lambda/2$ regime of PEM modulation, the PEM operates as alternating $\lambda/2$ plate, so gives a polarization cycle of s to π to s to $-\pi$ - linear polarization. As π equals $-\pi$ the PEM modulation frequency is twice the driving frequency (2f). **f** for a linear amplitude modulation one linear polarization (e.g. s) is cut by a Glan prism. **g**, for constant helicity with amplitude modulation, an additional $\lambda/4$ retarder is installed. Note, typically configuration **d** is used for pump (50 kHz) and **f** for probe (2x42 kHz), resulting in a mixed frequency detection on 34 kHz.

3.3.2.2 Laser Beam Modulation

To improve the signal to noise ratio it is useful to use the Lock-In technique. For this, it is needed to modulate the signal, which can be achieved by modulating the pump or the probe beams. In this study, typically both beams were modulated. Further, in order to fulfil the selection rules, Sec. 2.2, it is needed to control the polarization of the pump and probe beam. For the spin excitation, the pump beam needs to be circular polarized and for a measurement of the population dynamics, with use of the time resolved differential reflection and transmission, the pump beam needs to be linear polarized. In all cases, the probe beam is needed to be kept linear polarized. A circular polarization with simultaneous modulation can be achieved in several ways. In this study 3 types of modulators were used, electro optical modulators (EOM), photo-elastic modulators (PEM) and a chopper. The installation of the modulators and the resulting modulated beam profile is sketched in Fig. 3.3.4.

To gain an alternating polarization between σ^+ and σ^-, a helicity modulation, an EOM or PEM can be used. The EOM provides a squared modulation of variable frequency (DC-20 MHz), i.e. a time interval of one circular polarization is instantaneously changed to an equivalent time interval of the opposite circular polarization. For the PEM, the modulation follows a sinusoidal shape. In the maxima (+1 and -1), a full circular polarization is given while in between the change of polarization undergoes a transient via linear polarization at the saddle points (zeros). The PEM operates at a fixed frequency of 50 kHz.

An amplitude modulation of an either circular or linear polarized beam, is created with use of a PEM, EOM or chopper, see Fig. 3.3.4**b-c,f-g**. The use of an EOM or chopper gives an amplitude modulation of squared type, with the driving frequency equal to the modulation frequency. In case of a PEM, the modulation frequency is the double of the driving frequency. The PEM modulation operates as an oscillating λ retarder. An initially vertically polarized beam is rotated plus and minus 90°, so to π and a pseudo "$-\pi$" polarization in the maxima. Thus, results in a periodicity of π to s polarization, twice often as the PEM is driving frequency. With blocking of one polarization, e.g. s, and a downstream $\lambda/4$ retarder an amplitude modulated constant circular polarized beam is created. The PEM used for an amplitude modulation of the linear polarization of the probe beam operated at 42 kHz, i.e. 84 kHz effective.

Note, although the PEM, in $\lambda/4$ mode, is only 50% of the time circular polarized, in contrast to a full time circular polarization of the EOM, typically the PEM has still a better signal to noise ratio, thus it is preferential to work with PEMs.

The double modulation of pump and probe beam can be demodulated in either a tandem or mixed frequency demodulation. The mixed frequency demodulation operates with a difference frequency between pump and probe modulation frequency, e.g. 50 kHz - 84 kHz = 34 kHz for the two used PEMs, allowing to adjust only a single phase between reference and measurement signal. In the tandem approach, the measurement signal is demodulated one after the another, e.g. first by 50 kHz and afterwards by 84 kHz. For both demodulations steps, a proper phase is needed to be set between measurement signal and modulation reference signal, resulting in a difficult alignment.

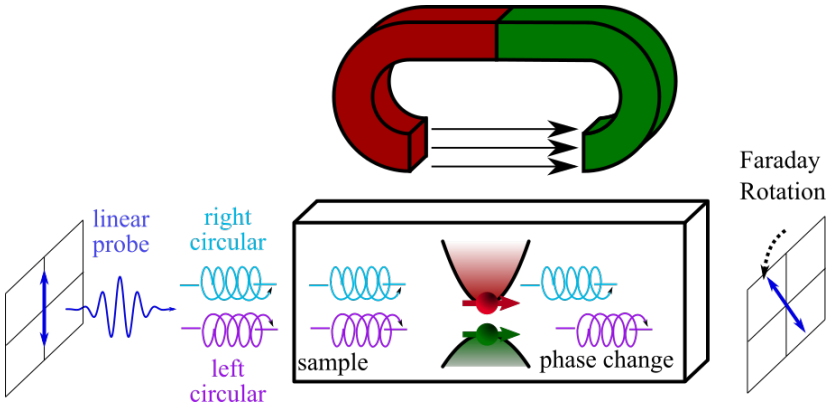

Figure 3.3.5 Scheme of Faraday Rotation/Ellipticity. As the light travels through the sample it is subject to two parameter changes; the first is a change of group velocity for left or right circular polarized light, giving a phase difference proportional to polarization and length of crystal; second, a disbalanced absorption may occur, giving an elliptical polarized beam (not depicted). Inspired by [Mer05]

3.3.2.3 Faraday and Kerr Effect

The Faraday effect and Kerr effect are both magneto optical effects sharing the same principles. Experimentally, it was observed in the year 1845 by Faraday [Far46]. A linear polarized beam transmitted through an optical medium, like glass, changed its polarization if a magnetic field was applied into the direction of the light propagation. A similar effect, a change of polarization of light which was reflected from a metal surface while a magnetic field was applied parallel to the light propagation direction, was found in year 1876 by Kerr [Ker77].

The basic principle of the Faraday effect is shown in Fig. 3.3.5. A linear polarized light beam can be understood as being composed of a phase matched equal amount of circular left σ^- and circular right σ^+ polarized parts. In the light transmitting medium, the magnetic field causes a circular birefringence $n_+ \neq n_-$, with $n_\pm$ the refractive index for respective $\sigma^\pm$ polarized light, via off diagonal terms in the relative dielectric tensor ϵ_r and the relative magnetic susceptibility tensor μ_r ($n = \sqrt{\epsilon_r \mu_r}$). The circular birefringence is proportional to the magnetic field strength B, $n_\pm \propto B$. Consequently, the time of flight $t_\pm = c/n_\pm l$, with l the path in the birefringent medium, differ for different polarization and causes a phase difference of σ^+ to σ^- polarized light, so in total a rotation of the linear polarization axis, which is the Faraday Rotation (FR). Empirically, the strength of the effect is characterised with the Verdet constant $\mathcal{V}$.
Similar to the retardation through the medium, a non equal circular absorption $a_\pm$ may occur, $a_+ \neq a_-$. The unbalanced amount of σ^+ to σ^- polarization causes an elliptical polarization of the transmitted beam, called Faraday Ellipticity (FE). Rotation and ellipticity are coupled via the Kramers–Kronig relation $\tilde{n} = n + \imath\kappa$, with $\tilde{n}$ the total refractive index, n the refractive index, and κ the absorption.
The same principle, an unbalanced intensity and phase, in the polarization of a reflected beam, named Kerr Ellipticity (KE) and Kerr Rotation (KR). Note, the circular and linear polarization of a light beam can be described together as a set of Stokes parameter, a different naming which is sometimes used in literature.

In the time resolved pump probe experiments, the Faraday/Kerr effect is also present in the absence of an external magnetic field. In the experiment, the polarized spins act analogue to the magnetic field, i.e. the z projection of the spin is detected. Further, the Faraday/Kerr effect is only sensitive to the energy band to which the probe beam is tuned $n(\lambda)$, e.g. reflecting an exciton or a trion resonance. For an exciton or a trion resonance, the expected spectral dependencies of the Faraday(Kerr) effect differ. The Faraday (Kerr) ellipticity, signal is following in both cases a bell and the rotation signal a dispersive shape [Gla12a; Fok10]. In detail, exciton and trion resonance are distinguishable. The ellipticity peak for the trion resonance shows a regular bell shape while the exciton resonance peak is following the form of a second derivative of this peak. Also, the signs of exciton and trion resonance differ, though this is difficult to identify in the experiment. In general the spectral dependence of the Faraday/Kerr signal reflects the sum of the excited states and can be of a complex shape [Fok10].

3.3.2.4 Extended Time Resolved Pump-Probe Technique

The extended time resolved pump-probe technique is used to achieve an extended time measurement span exceeding the laser repetition rate $T_R = 13.2$ ns, while maintaining the same temporal resolution. To achieve this, both pump and probe beam need to be pulse picked, with only pulse remaining in an interval of the desired time span, e.g. blocking of 4 pulses and only the 5th pulse being transmitted. If this would be done in the same manner for both pump and probe, one would need a mechanical delay of several tens of meters to probe the full timespan. However, the trick is to implement a trigger delay between the pulse picking of pump and probe. In this case, an integer number of T_R delays between pump and probe pulses can be set. The measurements then can be sequenced in steps of scanning 13.2 ns via the mechanical delay line and a followed increase of the trigger delay by 1 T_R [Bel16].
Experimentally, this is realized by the combined use of a commercial pulse picker, on basis of an AOM, pulse picking the probe together with an EOM pulse picking the pump beam. The EOM can be driven with an arbitrary signal generator and the respective pulse picking signal is triggered with a delay towards the probe pulse.

3.3.2.5 ODNMR Measurements with (TR)KR Detection

For the optical detection of the nuclear magnetic resonance (ODNMR), the time resolved pump probe scheme was extended by a small radio frequency (RF) coil, placed on top of the samples [Hei16; Sli90]. The RF coil consists of about 5 turns, ≈ 1 mm aperture and 5 mm diameter. The RF coil is mounted flat on the sample surface with a magnetic field direction parallel to the z-axis. The impedance of the RF coil is small compared to the internal termination of the RF driver, so nearly frequency independent in the applied frequency range of DC–10 MHz. The RF is driven by a constant voltage driver, whereas a voltage of $V_{RF} = 10$ V$\hat{=}B_{RF} = 1.1$ mT is used.

3.3.2.6 Time-Resolved Differential Reflectivity/Transmission

The time resolved pump probe scheme can also be used for the detection of the time resolved differential reflectivity or transmission. In this case, not the spin polarization but the

population is probed. Essentially, if a photon excites the sample, the sample is transparent for the following photon. With the use of differential reflectivity/transmission, the time which is needed for a followed excitation is probed.
For this, both pump and probe are linear polarized, which prevents spin polarization according to the selection rules. For the pump beam, this is the only change. From the probe beam, a beam is separated by a non polarizing beam splitter and used as a reference beam. It is directed to the balanced photodetector and its intensity is levelled to be equal to the reflected/transmitted probe beam while the pump beam is closed. The settings for the modulation of the pump and probe beams are described in Sec. 3.3.2.

3.3.3 Spin-Flip Raman Scattering (SFRS)

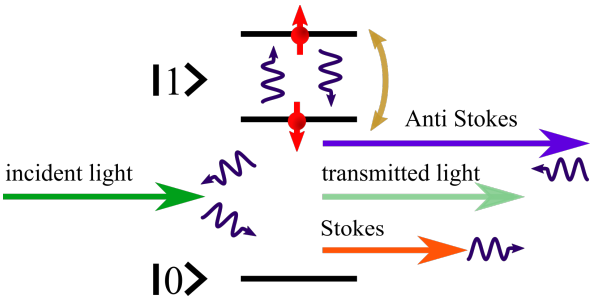

Figure 3.3.6 Spin Flip Raman Scattering. The incident photon (green arrow) with resonant energy to a transition $|0\rangle$ to $|1\rangle$ may cause the resident spin (red ball) to flip under emission or absorption of a phonon (short, curved arrow). The scattered light is either increased (purple arrow) or decreased (orange arrow) in energy.

The basic principle of the spin flip Raman scattering (SFRS) is sketched in Fig. 3.3.6 [Hä91]. If a photon undergoes a scattering event with a spin, the spin may flip under emission or absorption of a phonon. Then, the scattered light energy is either lowered (Stokes) or increased (Anti Stokes) by the amount of energy difference of the two spin states. The SFRS is only efficient for light which is resonant to the energy of a band to band transition in the semiconductor, e.g. the optical band gap energy, which would allow one to observe electron and hole spins. Further, the light needs to be polarized according to the selection rules, circular (linear) for a magnetic field applied in Faraday (Voigt) geometry. While in the ordinary Raman scattering, the shift in energy reaches several meV, in accordance with the involved phonon [Ram28; Lan28], the shifts in SFRS are usually observed in the μeV scale.

4

Carrier Spin Dynamics in $FA_{0.9}Cs_{0.1}PbI_{2.8}Br_{0.2}$ Bulk Single Crystals

As first material of these studies, the carrier spin dynamics in bulk $FA_{0.9}Cs_{0.1}PbI_{2.8}Br_{0.2}$ (FA=formamidinium, $CH(NH_2)_2$) shall be presented. As discussed in the method section, $FA_{0.9}Cs_{0.1}PbI_{2.8}Br_{0.2}$ has a tolerance factor close to one and a high chemical and crystallographic stability [Jeo15; Zha21b]. An image of the sample is shown in Fig. 4.1.1**a** repeated from Fig. 3.1.2. In this section it will be shown, that the carrier spin dynamics in $FA_{0.9}Cs_{0.1}PbI_{2.8}Br_{0.2}$ single crystals are well observable and give a descriptive picture. Both carriers, the electron and the hole spin dynamics will be observed simultaneously, and their underlying couplings will be revealed by application of external perturbations, like a magnetic field or a varied thermal environment. It will be shown, that hyperfine interaction of the carrier spin with the lead nuclear spins is dominant.

The results presented in this section, were published in [Kir21b].

4.1 Basic Optical Properties

The $FA_{0.9}Cs_{0.1}PbI_{2.8}Br_{0.2}$ single crystals are of a deep black colour with a slight metallic shimmer, suggesting a high light absorption in the visible range and a spectrally flat reflection of the remaining light. The single crystals show rhomboid facets with partially not fully evolved corners. The front facet was excited with a 3.05 eV (405 nm) continuous wave (cw) laser for the photoluminescence (PL) excitation (see methods Sec. 3.3.1). The PL, recorded at $T = 6$ K, Fig. 4.1.1**a**, shows a single peak emission, with an emission maximum at 1.495 eV, a FWHM of 6.4 meV, and a broad low energy shoulder with a low intensity. While the main peak can be assigned to the exciton emission, the origin of the low energy shoulder is less clear. If the main emission is related to the recombination of free excitons, the emission at a lower energy might be related to either bound excitons or shallow defects. The close vicinity of the low energy shoulder to the main emission, with approximate only 5 meV separation makes the emission of bound excitons more probable, as the energetic separation of shallow defects is estimated to be higher [Mus21]. The exciton character is further proofed by a measurement of the photoluminescence excitation (PLE). Here, the PL amplitude is studied, in respect to its excitation energy. The PLE profile is shown in Fig. 4.1.1**a**. The PLE profile

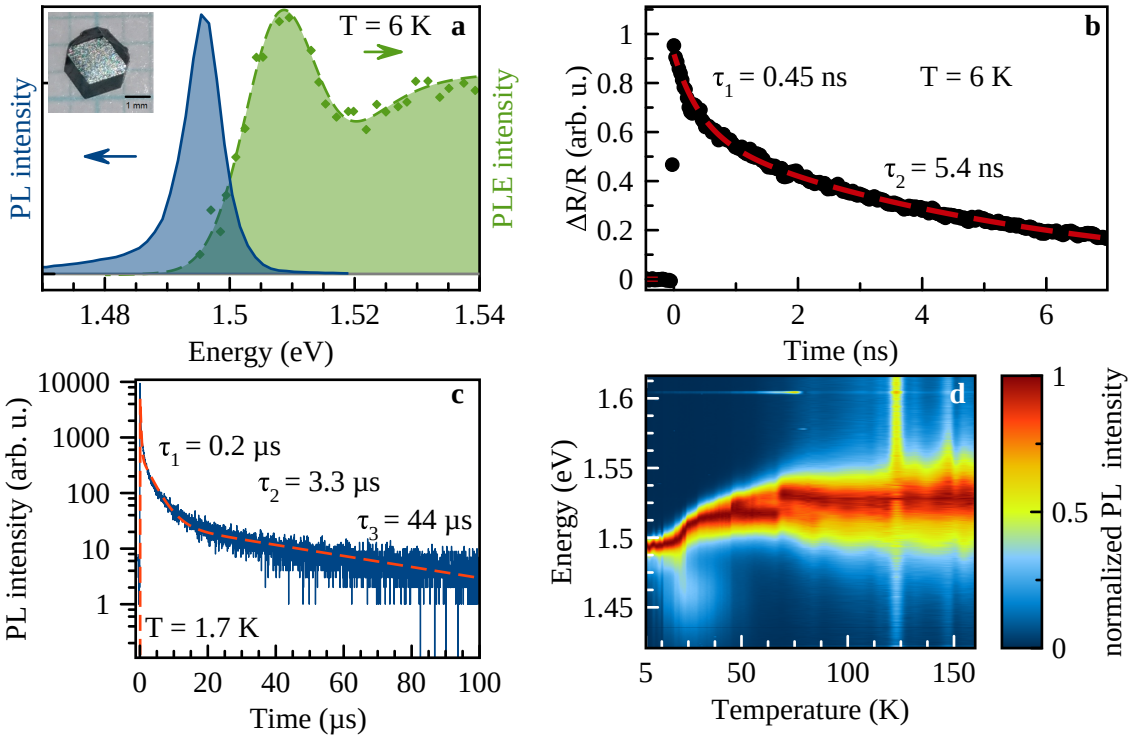

Figure 4.1.1 Linear spectroscopy of $FA_{0.9}Cs_{0.1}PbI_{2.8}Br_{0.2}$. **a**, Photoluminescence (PL) (blue) and Photoluminescence excitation (PLE) (green) spectra at $T = 7$ K in absence of magnetic field. PL spectrum was excited with $\lambda = 750$ nm (1.653 eV) laser power 0.5 mW, while for PLE the excitation energy is tuned and the intensity of emission intensity at 1.495 eV recorded. In upper left corner a photography of $FA_{0.9}Cs_{0.1}PbI_{2.8}Br_{0.2}$ crystal is shown. **b**, Time resolved differential reflectivity $\Delta R/R$ (black dots) for reflected laser energy of 1.514 eV. Bi-exponential fit (dashed line) gives time constants $\tau_1 = 0.45$ ns and $\tau_2 = 5.4$ ns. $T = 6$ K **c**, Time resolved photoluminescence intensity of line 1.49 eV excited with 2.33 eV (10 kHz pulsed) laser (blue line), $T = 1.7$ K. Fit with 3 decaying exponents gives $\tau_1 = 0.2$ μs, $\tau_2 = 3.3$ μs and $\tau_3 = 44$ μs. **d** Temperature dependence of photoluminescence as 2D colour map. Excited with 2.541 nm. All individual spectra are normalized on respective highest measured intensity.

can be described as a single peak on top of a step-like function. The peak maximum is at 1.508 eV and the FWHM is 13.2 meV. The step-like profile can be described with a fit function, inspired by the Fermi–Dirac statistics, $\left(f(E) \propto \frac{1}{\exp(-(E-E_0)/\Delta E)+1}\right)$, with resulting in a central energy of $E_0 = 1.516$ eV, a width $\Delta E = 5.9$ meV, and an arbitrary amplitude A. The difference of 13 meV between the PLE and the PL maximum is related to the Stokes shift (see ≈ 97 cm^{-1}(12 meV) Raman line observed in the orthorhombic phase of $MAPbCl_3$ crystals [TN20]). The differential reflectivity ($\Delta R/R$), giving a measure of the exciton population relaxation time, is shown in Fig. 4.1.1**b**. A double exponential decay is seen, with a fast component with a time constant of 450 ps, and a longer one with 5.4 ns. Further, the dynamics of the photoluminescence was measured, Fig. 4.1.1**c**. The PL dynamics, measured with a fast time of flight card and a pulsed 532 nm, 10 kHz laser source, shows a strong non exponential decay with recombination times between 0.2 and 44 μs, exceeding by far the typical exciton

recombination times, and being a characteristic for a slow recombination of spatially separated carriers. Finally, the temperature dependence of the photoluminescence spectrum in a range of 5–150 K is shown, in Fig. 4.1.1**d** as a colour map. Focusing only on the strongest emission energy, the PL emission energy is for the range of 150 K down to 70 K almost constant and then shifts monotonously from 70 K to 10 K, by about 30 meV, towards a lower energy. In the range of 10 K to 5 K, the shift settles down and the maximum PL emission energy stays constant at 1.49 eV. One should note a signature of a small splitting of the PL line around 70 K (a small drop in intensity in between the peaks, at 1.525 eV, identifies the presence of two peaks), which could be an indicator of an occurred crystal phase change, e.g. as seen in the PL spectrum of $MAPbI_3$, Fig. 5.1.1. However, in the case of $MAPbI_3$ the crystal phase change is much stronger pronounced. Overall, the shift of maximum PL emission energy is stronger than the corresponding thermal energy ($k_BT = 86.17\ \mu\text{eV} \cdot 150\ \text{K} = 12.9$ meV), and can be fully attributed to a change of the crystal lattice, e.g. the lattice contraction leads to an increased chemical bonding energy, which decreases in turn the distance of the valence band anti bonding level (Pb $6s$-I $5p$) to the conduction band lead ($6p$) orbital.

4.2 Coherent Spin Dynamics of Electrons and Holes

With a measurement of the time resolved Kerr rotation or ellipticity, one turns from the dynamics of a population to the magnetic, so carrier spin, dynamics. The measurements of the carrier spin dynamics features several correlated aspects, thus some aspects will be needed to be discussed before the experimental evidence can be shown. First, the general spectral response of the carrier spins shall be shown, followed by a discussion of the spin relaxation in terms of T_1. Then, with a switch to a magnetic field applied in Voigt geometry, the carrier g-factors and dephasing times T_2^* will be discussed. Lastly, the hyperfine interaction will be studied in terms of a dynamic nuclear polarization and related aspects.

4.2.1 Time-resolved Kerr rotation of electron and hole spins

The spectral dependence of the Kerr Rotation (KR) amplitude is shown in Fig. 4.2.1**a**. The KR amplitude represents the amplitude of a time resolved KR (TRKR) signal at a time equal to zero. In the TRKR, for both carrier spins, of electrons and holes, a signal can be found. Both KR amplitudes follow an asymmetric dispersive profile, typical for the KR response [Gla12a]. The KR amplitude maxima coincide for electron and hole, located at 1.512 eV for the maximum and 1.521 eV for the minimum. Though the KR amplitude magnitude is not identical for electron and hole. While they are of the almost same strength in the low energy region, they strongly differ for the high energy region. Interestingly, one can find spectral positions, in between the conversion from positive to negative amplitude sign, where the hole amplitude sign has already flipped but the electron amplitude not. The Kerr Rotation amplitude is taken from measurements in Voigt geometry, as shown in Fig. 4.2.2, which allow the carrier identification. The full spectral series of TRKR signals is not shown here.

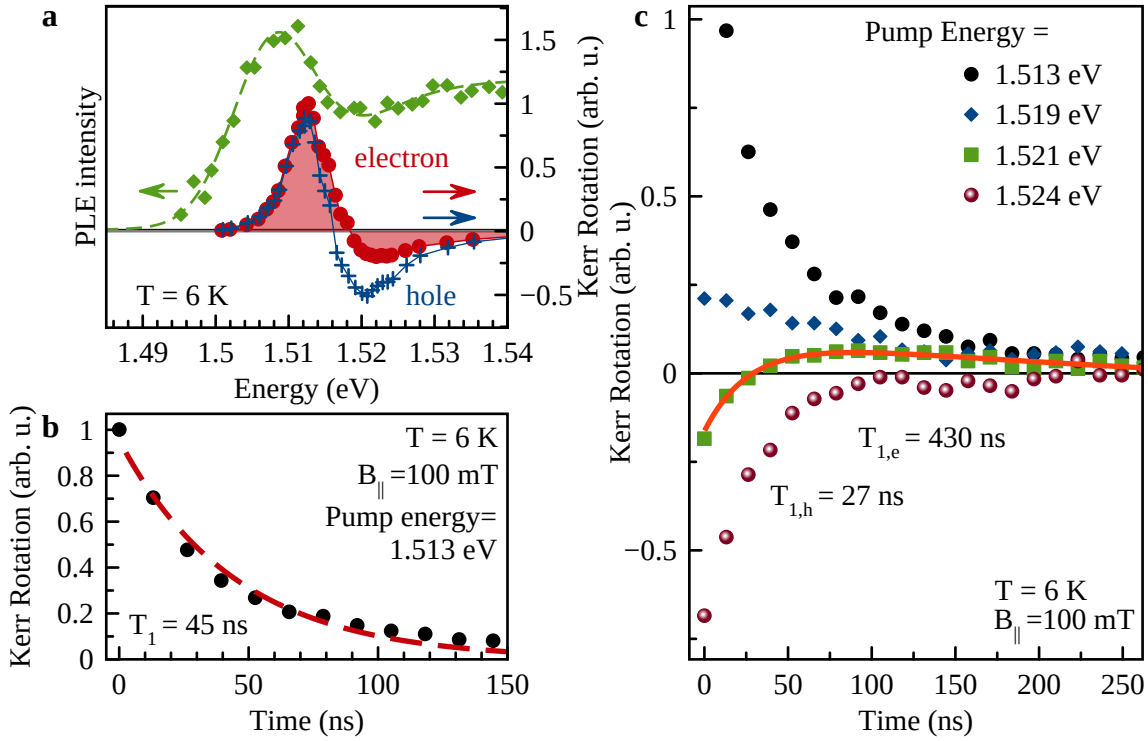

Figure 4.2.1 Carrier spin dynamics introduction - Spectral response and spin lifetime. **a**, Right, spectral dependence of time resolved Kerr Rotation amplitude at $t = 0$ ps with magnetic field in Voigt geometry ($\theta = 90°, \varphi = 0°$), $B = 0.1$ T, for electron (red) and hole beats (blue) at $T = 6$ K. Left, PLE profile as in 4.1.1**a** for reference. **b**, Spin dynamics in a magnetic field in Faraday geometry $B_{\parallel} = 100$ mT (dots) and $T = 6$ K measured with extended pump probe technique (see methods 3.3.2.4). A mono-exponential fit (line) gives $T_1 = 45$ ns. A pump and probe laser energy of 1.513 eV was used. **c**, Spectral series of spin dynamics in Faraday magnetic field $B_{\parallel} = 100$ mT (symbols), as shown in panel **b**. With higher excitation energy, according to the spectral dependence of the Kerr Rotation amplitude, shown in panel **a**, at an energy of 1.517 eV, the hole should show a negative KR amplitude while the electron has positive sign. Indeed, a KR signal is found (green squares) consisting of two components with opposite signs for the components. However, as the magnetic field geometry and the excitation regime (regular pump probe in **a** and extended pump probe in **c**) differs, the components can't unambiguously assigned, but the hole is taken as the earlier flipping and as the a higher amplitude component. The data was fitted giving $T_{1,h} = 27$ ns and $T_{1,h} = 430$ ns.

4.2.2 Spin Relaxation Time T_1

As a next step, the extended pump probe Kerr Rotation technique (exPP KR) was used to determine the spin relaxation time T_1, shown in Fig. 4.2.1**b**. The exPP KR signal was recorded at a magnetic field in Faraday geometry of 100 mT, to ensure that the applied condition is dominant in respect to any other perturbation fields, like nuclear fluctuations or else (see. PRC curve Fig. 4.3.1). This allows a clean separation between T_1 and T_2 in a longitudinal magnetic field, as $T_1 = T_2$ in absence of a magnetic field. A long decay is seen, which can be fitted, in good agreement, with a single exponential curve, giving a carrier relaxation time T_1

of 45 ns at $T = 6$ K. The exPP KR curve was measured with a laser energy corresponding to the maximum KR signal. In absence of a spin oscillation a carrier identification is difficult. However, as it was shown, in Fig. 4.2.1**a**, the carrier amplitude sign changes at different spectral positions for electron and hole spin. Hence, a carrier identification might be possible with the analysis of the spectral dependence of the exPP KR signal, shown in Fig. 4.2.1**c**. The exPP KR signal indeed follows roughly the spectral response as previously shown. The signals have a fully positive amplitude for energies below 1.519 eV, are partially flipping at an energy of 1.521 eV, and are fully negative above energies of 1.524 eV. Interestingly, the signal for an energy of 1.521 eV, shows the presence of two individual components. Both components are exponential damped curves, one with a high amplitude and a short time constant, the other with a lower amplitude but a longer time constant. In comparison to the previously shown KR amplitude spectral response, Fig. 4.2.1**a**, the spectral position of the amplitude sign change, is slightly detuned, and also the total amplitude of the negative signal is higher then before, which makes the comparison not strictly valid. Still, in general, the component, which flips earlier with an increasing energy, shows also a slightly higher signal amplitude. This gives rise to the assumption, that this component can be identified as an hole signal and the second one as originated by electron. Following this assumption, $T_{1,h} = 27$ ns and $T_{1,e} = 430$ ns. As this assignment is not without doubts, a general carrier relaxation time of $T_1 \approx 45$ ns should be considered.

4.2.3 Spin Dynamics in Voigt Magnetic Field Geometry T_2^* and Carrier g-factors

If a magnetic field in Voigt geometry is applied, the spin dynamics undergoes a Larmor precession with an accompanied decay time (spin dephasing T_2^*). An exemplary time resolved Kerr Rotation (TRKR) signal is shown in Fig. 4.2.2**a**, for a magnetic field $B_\perp = 100$ mT at a temperature $T = 6$ K. The signal can be analysed with a Fast Fourier Transformation (FFT), Fig. 4.2.2**b**, giving two distinct peaks. The lower frequency peak can be assigned to originated from the hole spin, and the higher frequency peak from the electron spin beating. A slightly more narrow peak width is seen for the hole spin as compared to the electron spin, suggesting, a slightly longer dephasing time. This can be evaluated more precisely, if one fits the TRKR signal with two damped oscillating components ($TRKR(t) = \sum_{m=\mathrm{e,h}} A_m \cos(\omega_m t) \cdot \exp(-t/T_{2,m}^*)$, with m being either electron or hole, ω_m the magnetic field dependent Larmor frequency, and $T_{2,m}^*$ the magnetic field dependent ensemble dephasing time). For this curve an electron g-factor $|g_\mathrm{e}| = 3.57$ and $T_{2,\mathrm{e}}^*(100\ \mathrm{mT}) = 1.9$ ns and for hole $|g_\mathrm{h}| = 1.21$ and $T_{2,\mathrm{h}}^*(100\ \mathrm{mT}) = 2.4$ ns can be evaluated. Although the KR signal is insensitive to the g-factor sign, the $\mathbf{k} \cdot \mathbf{p}$ theory, as atomistic estimates, suggests a positive electron and a negative hole g-factor sign $g_e > 0$, $g_h < 0$ [Yu16; Nes21].

The dependence of the TRKR signals, with a present spin precession, upon the magnetic field magnitude is shown in Fig. 4.2.2**c**. With increasing magnetic field, the Larmor precession frequency increases and the spin dephasing rate accelerates. The carrier spin Larmor frequencies, Fig. 4.2.2**d**, evolve linearly with the magnetic field and show a vanishing zero field Larmor precession frequency (offset). The dephasing rate ($1/T_2^*$), Fig. 4.2.2**e**, follows a linear dependence upon the magnetic field,

$$1/T_2^* = 1/T_{2,0}^* + \Delta g \mu_B B, \tag{4.2.1}$$

with the spread of g-factor $\Delta g_e = 0.06$ and $\Delta g_h = 0.02$ [Yak08]. The zero field dephasing time is limited, by a non vanishing residual fields such as the nuclear field fluctuation. This is can be seen by the saturating behaviour of T_2^*, if the magnetic field approaches zero, Fig. 4.2.2**f**. For electrons, $T_{2,0}^* = 8$ ns, is longer than for holes, $T_{2,0}^* = 5.5$ ns, as suggested by the higher hyperfine interaction of holes compared to electrons. More on that in Sec. 4.3. Further the long dephasing time, longer than the estimated exciton recombination time, combined with the absence of a zero field Larmor precession frequency offset, and an inequality of the electron and hole Kerr amplitude, denies the signal to be originated by excitons, but rather suggests resident carriers, being weakly localized at different crystal sites, to be the origin [GA21]. The weak localization of the resident carriers will be also evidenced by the relative low thermal activation energy, presented in Sec. 4.2.4.

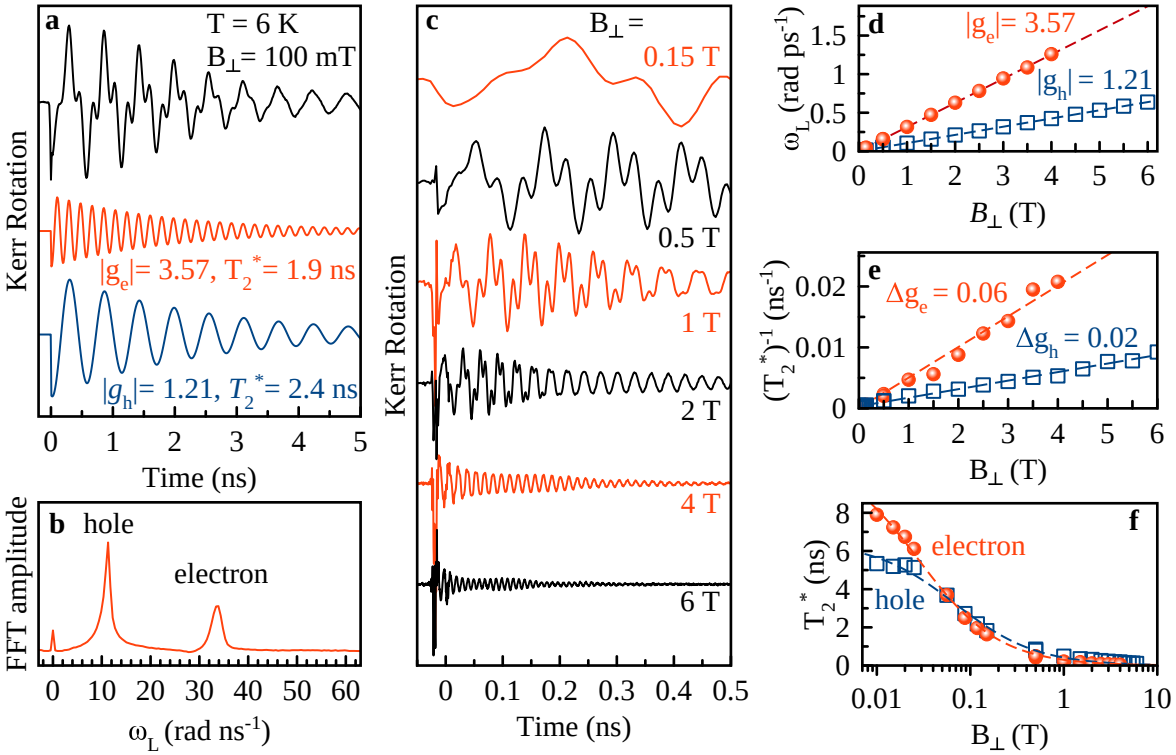

Figure 4.2.2 Spin dynamics of resident carriers in Voigt geometry. **a**, Time-resolved Kerr rotation signal at $B_\perp = 100$ mT (black). Superimposed spin beatings are decomposed by fit and shown vertically shifted below, electron (red) and hole (blue). $T = 6$ K. **b**, Fast Fourier transformation (FFT) spectrum of the KR signal in **a**. Low frequency $\omega_{L,h} = 11.30$ rad ns^{-1} hole- and higher frequency $\omega_{L,e} = 33.90$ rad ns^{-1} electron-peak are labelled correspondingly. **c**, TRKR signals for increasing magnetic field strengths. Signals are shifted vertically for clarity and are not normalized. With increasing field, the Larmor frequency grows and T_2^* shortens. Note slight overtones in the signal which indicate the presence of a minor additional contribution. As it is invisible in FFT, it is neglected in the following. **d**, Larmor frequency dependence on magnetic field extracted by fit from **c** (symbols). Linear fits (lines) give $|g_e| = 3.57$ and $|g_h| = 1.21$. {**f**} **e**, {inverse} T_2^* dependence on magnetic field for electrons and holes (symbols). Note the logarithmic scale for the magnetic field in **f**. Lines are fits along Eq. (4.2.1) with $\Delta g_e = 0.06$ and $\Delta g_h = 0.02$.

4.2.4 Temperature Dependence

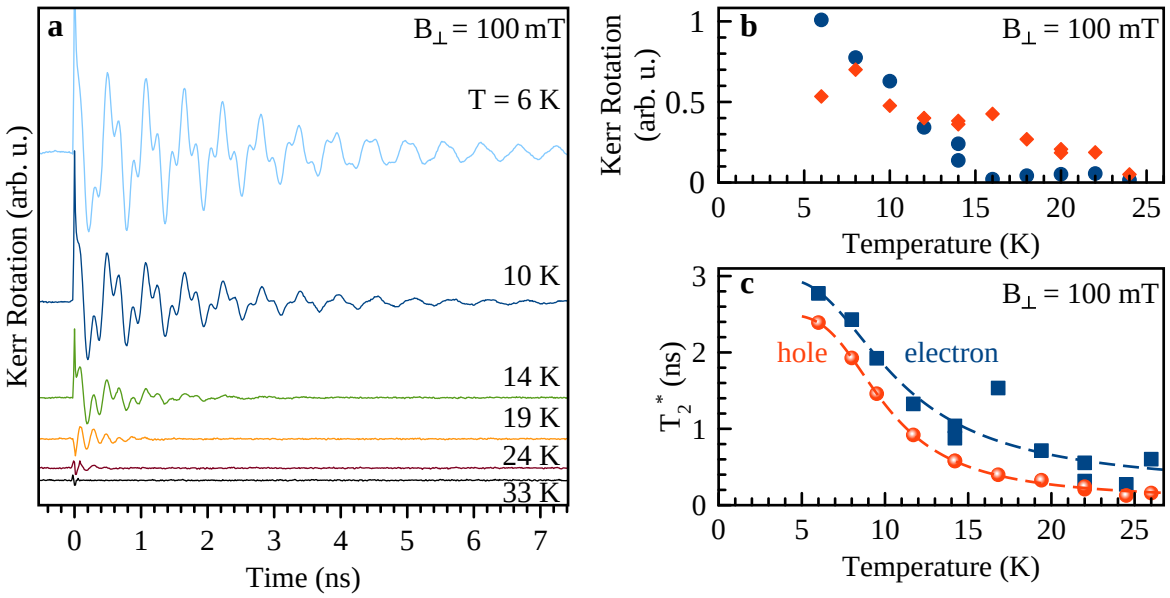

Figure 4.2.3 Spin dynamics temperature dependence. **a**, TRKR dynamics for temperatures from 6 K to 33 K at $B_\perp = 100$ mT ($\theta = 90°$, $\varphi = 0°$). Data are shifted vertically for clarity and are not normalized. Pump power is kept low at 0.5 mW. **b**, KR amplitude at zero time delay versus temperature for electron (red) and hole (blue). The KR amplitude is interpolated via a fit and not phase corrected. **c**, Temperature dependence of T_2^* (symbols). Lines are Arrhenius-fits with $E_{A,e} = 3.8$ meV for electrons and $E_{A,h} = 2.9$ meV for holes.

In a magnetic field in Voigt geometry, a dependence of the TRKR signal on the bath temperature was measured. In Fig. 4.2.3**a**, a corresponding series is shown. Starting from a clearly pronounced signal in low temperatures, $T = 6$ K, the signal decreases and vanishes already at earlier time delays, when the temperature rises. Already at a slightly elevated temperature, of $T = 15$ K, the signal is almost absent. From the series, the KR amplitude and dephasing times were extracted by fits, Fig. 4.2.3**b**–**c**. Indeed, the amplitude drops rapidly, whereas a small discontinuity is seen around $T = 15$ K, which corresponds to a careful sample readjustment. Which was needed, in order to compensate a small thermal expansion of the sample holder. The dephasing time temperature dependence can be described by an Arrhenius-like function $1/T_2^*(T) = 1/T_{2,0}^* + w \exp(-E_A/k_B T)$, with a constant w characterizing the strength of the carrier-phonon interaction (0.03 ps^{-1} for electrons and 0.06 ps^{-1} for holes), E_A the activation energies ($E_{A,e} = 3.8$ meV and $E_{A,h} = 2.9$ meV), and k_B the Boltzmann constant. The activation energies quantify the carrier localization in shallow potential fluctuations. In order to keep the influence of the pump laser-induced heating of the charge carriers and the lattice low, the pump power was set to 0.5 mW.

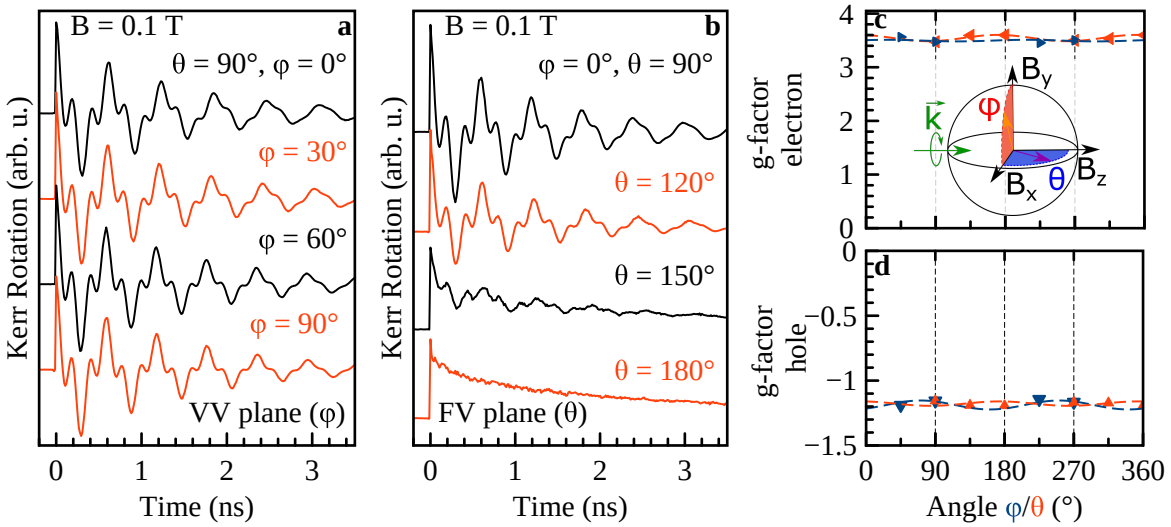

Figure 4.2.4 Carrier g-factor anisotropy. a {**b**}, TRKR signals within the Voigt-Voigt (VV) {Faraday-Voigt (FV)} plane (B = 100 mT, $\theta = 90°$, φ scanned {B = 100 mT, $\varphi = 90°$, θ scanned}), T = 1.6 K, P = 10 mW. All curves are shifted vertically for clarity. **c**–**d**, g-factor dependence on solid angle φ (blue), θ (red). **inset**, Sketch of magnetic field orientation with respect to the incident light vector **k**. Red (blue) plane corresponds to Voigt-Voigt (Voigt-Faraday) plane. $\varphi = \theta = 0°$ corresponding to $\mathbf{B}_{\parallel,z}$.

4.2.5 Carrier g-factor Anisotropy

Perovskite crystals undergo several phase changes when they are cooled down, e.g. leading to an asymmetry in the lattice periodicity distance of the a, b and c-axis, Sec. 2.1.4. Thus, also an anisotropic carrier g-factor might be expected, see theory Sec. 2.1.3. A measurement series was performed, where the magnetic field vector length ($B = \sqrt{B_x^2 + B_y^2 + B_z^2}$) is kept constant and only the angle towards the exciting beam direction **k** is rotated. The laboratory spherical coordinate system is fully described by the following three coordinates: the magnetic field vector length B, the horizontal angle θ, and the vertical angle φ, see sketch in Fig. 4.2.4**c**. An angle of ($\theta = 0°, \varphi = 0°$) equals a magnetic field aligned in Faraday geometry and the Voigt geometry is given in the plane with $\theta = 90°$ under variable φ. The special Voigt field direction $B_\perp$ corresponds to ($\theta = 90°, \varphi = 0°$).

Series of TRKR signals for the Voigt-Voigt plane (VV-plane) and Faraday-Voigt plane (FV-plane) are shown in Fig. 4.2.4**a-b**, respectively. Remarkably, the TRKR signal stays almost identical for the VV-plane and only shows a change in the FV-plane. In the FV-plane the TRKR signal turns from two exponentially damped oscillatory signal (in Voigt geometry) into a simple exponential damped signal (in Faraday geometry). The rise of an non oscillatory signal is expected, as with inclining the magnetic field, the spin exhibits a constant projection onto the z-direction, see Sec. 2.3.1 and Sec. 3.3.2.3. From the extracted Larmor frequencies, the corresponding g-factors were directly calculated, assuming a vanishing magnetic field offset and linearity of the Larmor frequency upon the magnetic field, Fig. 4.2.4**c**–**d**. However, as the magnetic field vector length was chosen to be 100 mT, for the sake of long spin dynamics, already small imperfections in the magnetic field installation, could give rise of a relatively high

error. Thus, it is remarkable, that the g-factor anisotropy is not exceeding 3% for electrons and 4% for holes. The results were additionally confirmed by spin flip raman measurements, presented in [Kir21b]. The results show, that the orthorhombic phase of $FA_{0.9}Cs_{0.1}PbI_{2.8}Br_{0.2}$ single crystals, is only small distorted towards a cubic phase realization. Furthermore, the knowledge of an isotropic g-factor and the knowledge of its spin dynamics in tilted magnetic fields, will be used if one wishes to identify the presence of a dynamic nuclear polarization, seen in the next section.

4.3 Carrier Nuclear Spin Hyperfine Interaction

One of the major spin interactions, even the dominant one, for localized carrier spins is the hyperfine interaction. In particular for the hole spins, which exhibit an s-type orbital, the hyperfine interaction with lead spins is supposed to be strong. In a first, step the nuclear spin surrounding is measured via its passive influence, as providing a nuclear spin fluctuation field B_{NF}. This is seen as a remaining magnetic field spin perturbation, in the absence of an external magnetic field. Next, a protocol will be applied to create a dynamic nuclear polarization (DNP), giving rise to a net effective nuclear magnetic field, acting on the carrier spins, the Overhauser field. Last, while a dynamic nuclear polarization is present, a radio frequency is applied and tuned in resonance with the nuclear Zeeman splitting, which will perpetuate the dynamic nuclear polarization, giving a nuclear isotope specific signature, and enables one to identify the interacting nuclear spin species.

4.3.1 Nuclear Spin Fluctuations

Even in long time delays, the spin dynamics don't vanish. The method of polarization recovery and resonant spin amplification can be applied to gather clean informations about a long prevailing spin system, even of time scales exceeding the laser pulse repetition time, without overlap of short time scale signals and perturbation, e.g. photo generated carriers, complex spin excitation protocols etc., see Sec. 2.5 and 2.7.
The resonant spin amplification (RSA) curve is shown in Fig. 4.3.1**a** (turquoise curve). The RSA curve, measured in Voigt geometry, shows a complex shape, clearly composed of several components. First, no sharp peaks are found but rather sinusoidal beatings, as assumed from spin dephasing times below the laser repetition period. A combined analysis, with a fitting of the RSA with four RSA curves (Eq. (2.7.1)), combined with a Fast Fourier Transformation (FFT), Fig. 4.3.1**b**, reveals the presence of multiple contributing signals, of whom one can be identified as originated from electron and one as hole signal by the respective g-factors. In good agreement, with previous high field TRKR measurements, only a rather small spread of g-factor magnitude is needed to be taken into account. In fact, for the electron and hole signals, it was set to zero. However, at least two more components are superimposed to the RSA signal, one with a g-factor of 1.37 and another with 1.94, both with a high spread of g-factor, $> 10\%$. Due to high spread of g-factor, they vanish at small magnetic fields and are fully hidden in the TRKR signals. Further experiments need to be carried out, to identify their origin.
The polarization recovery curve (PRC), obtained in Faraday geometry, shows a shape of two superimposed Lorentzian type dips. The width of the PRC curves is proportional to the

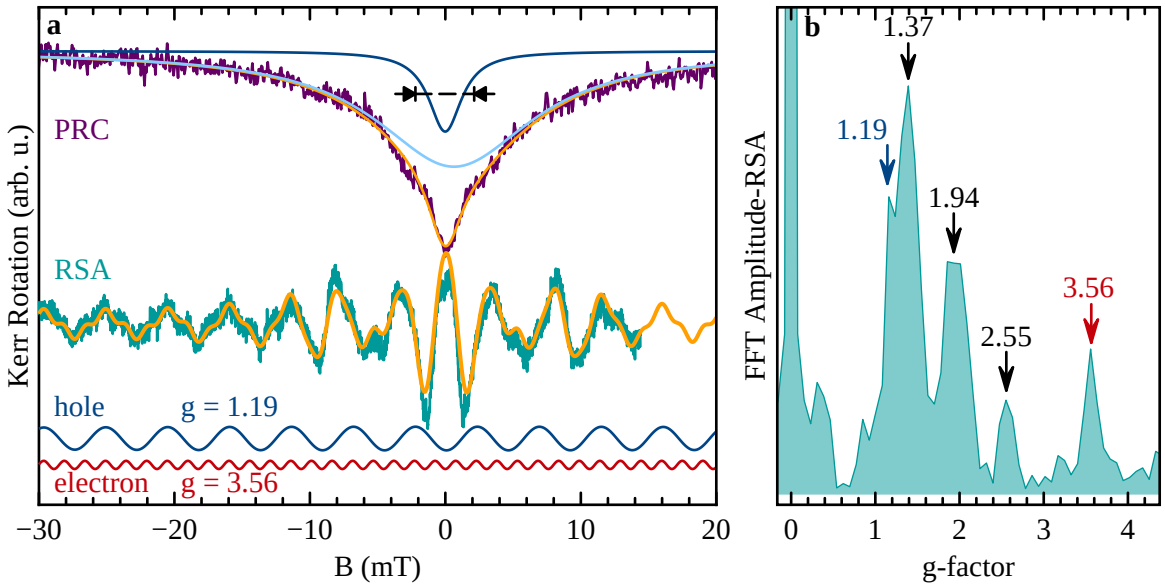

Figure 4.3.1 Resonant spin amplification (RSA) and Polarization Recovery Curve (PRC). a, Kerr rotation signal at small negative time delay $t - 10$ ps, with swept magnetic field in Voigt (RSA) and Faraday (PRC) geometry. **Top**, the PRC curve (purple) is fitted by two Lorentzian dips (yellow line), with one narrow (HWHM= 1.4 mT) (dark blue curve), and one broader (HWHM= 7 mT) (light blue curve). An indicator of the FWHM is shown by the arrows. Both fitting components (light and dark blue) were shifted vertically to the PRC curve amplitude maximum for clarity. The classification of PRC components to a carrier type is not clear. Still, due to the smaller amplitude and smaller hyperfine interaction of the electron in typical TRKR experiments, the narrow component (2.9 mT) could be assigned to the electron while the broader with higher hyperfine interaction and amplitude (14 mT) might originate from the hole. **Bottom**, RSA curve (turquoise) with best agreement fit (yellow). The fit is composed from several RSA curves. The hole component (blue) and electron component (dark red) are separately plotted and shifted vertically for clarity. **b**, Fast Fourier Transform (FFT) of RSA signal (**a**). The FFT axis of a RSA curve is natively in scale of B^{-1}, here directly converted with $g = h/T_R\mu_B B$, with $1/T_R = 13.2$ ns, the laser repetition frequency, into a g-factor scale. A complex peak structure is visible, while peaks for electron and hole ($g = 3.56$ and $g = 1.19$) are coloured. Note, the peaks at $g = 1.37$ and $g = 1.94$ correspond to additional RSA components with a high spread of g-factor ($> 10\%$), also used in the fit in **a**. The peak at $g = 2.55$ was not found as separate component in the TRKR fitting, but is marked for its clear separation.

strength of the nuclear fluctuation field B_{NF}, thus the broad one can be related to holes and the narrow one to electrons, $B_{NF,h} = 7$ mT and $B_{NF,e} = 1.4$ mT. One needs to note, the PRC Kerr rotation amplitude and RSA KR amplitude don't share the same amplitude scale in Fig. 4.3.1. They have been measured, as for experimental reasons, * on a slightly different spot on the sample, and a slightly different quality of the reflected probe beam.

*rotation of 7 T cryostat

4.3.2 Dynamic Nuclear Polarization

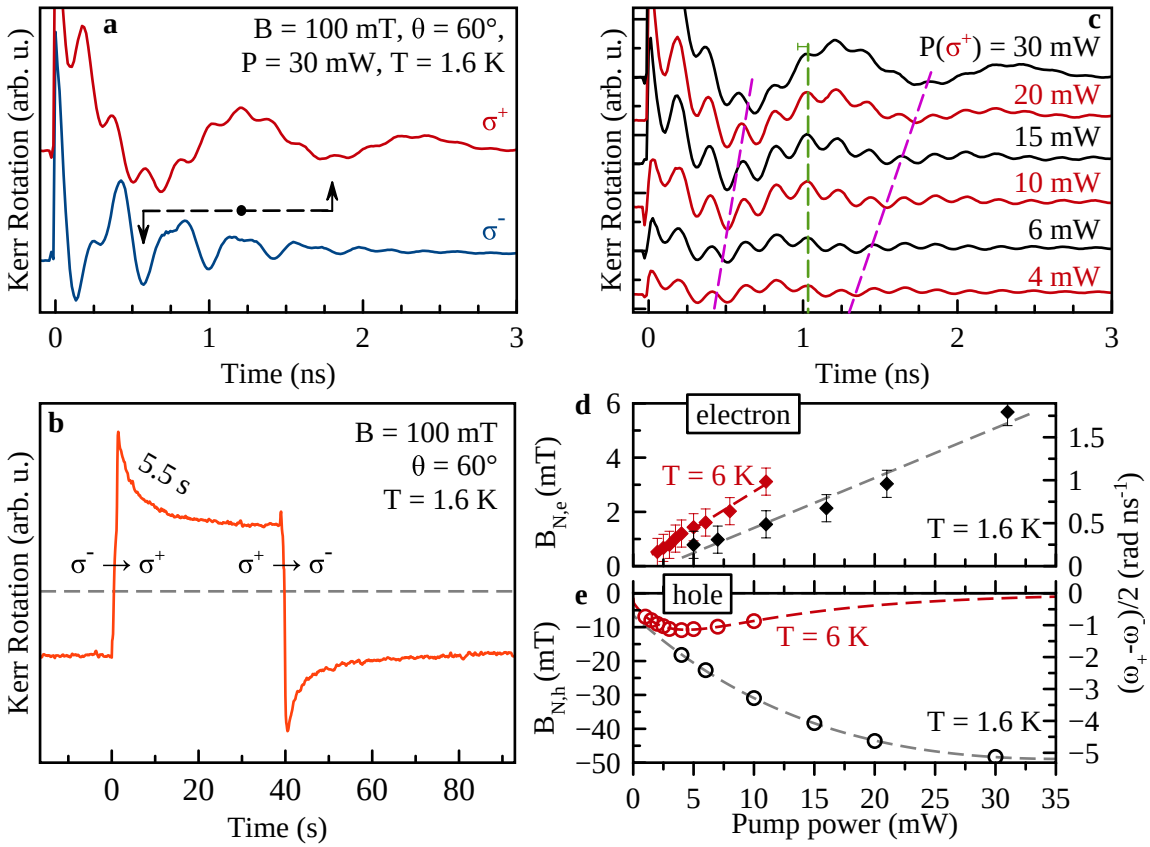

Figure 4.3.2 Dynamic nuclear polarization. **a**, TRKR signals in regime of dynamic nuclear polarization (DNP), constant helicity excitation with σ^+ (red) and σ^- (blue) at high pump power $P = 30$ mW, $T = 1.6$ K and oblique magnetic field $B = 100$ mT, $\theta = 60°$, $\varphi = 0°$. Both signals show pronounced differences in the hole beating frequency. The 2nd minimum is indicated by an arrow. Note, naturally the Kerr Rotation angle would show an opposite sign for σ^+ and σ^- excitation. For easier comparison, the signals were calculated to show both positive $t = 0$ ps Kerr angle. Both curves were shifted vertically for separation. **b**, KR signal for a fixed time delay of $t = 0.5$ ns and conditions as in **a**, only slightly lower pump power of 20 mW. The signal represents the dynamics of the hole Larmor frequency change with build up of an Overhauser field due to DNP. Sequence of polarization: 2 min σ^-, 40 s σ^+, 2 min σ^-. Repolarization of nuclei occurs with a time of 5.5 s. **c**, TRKR measured at pump powers of 4–30 mW. The change of Larmor frequency ω_L is traced for the 1st and 2nd minima with purple dashed lines for the hole precession, and for the 5th maximum for the electron with the green line. $T = 1.6$ K. Note, the opposite sign for the change of the Larmor frequency of electrons and holes. For the holes the Larmor frequency is decreasing while it is increasing for the electrons. **d-e**, Dependence of $B_{N,e(h)}$ on pump power at $T = 1.6$ K (black) and 6 K (red), with magnetic field conditions as prior. Right scale shows the change of Larmor frequency. Dashed lines give lines for the eye.

In the presence of a carrier spin polarization, not only an influence of the nuclear spin bath on the carrier spins is present, but also the carrier spin polarization can lead to a nuclear

spin polarization, the dynamic nuclear polarization (DNP), by carrier nuclear spin flip flop processes. The nuclear spin polarization $\langle \mathbf{I} \rangle$, see also theory Sec. 2.4, reads

$$\langle \mathbf{I} \rangle = l \frac{4I(I+1)}{3} \frac{\mathbf{B}(\mathbf{B} \cdot \langle \mathbf{S}_{\mathrm{e(h)}} \rangle)}{B^2}, \tag{4.3.1}$$

with $\mathbf{I}$ being the nuclear spin, $\mathbf{S}_{\mathrm{e(h)}}$ the steady-state polarization of carriers induced by the optical orientation, and l the leakage factor characterizing the losses of the nuclear polarization due to relaxation processes other than the hyperfine coupling [Mei84; Abr94]. As seen, by the scalar product $\mathbf{B} \cdot \langle \mathbf{S} \rangle$, a perpendicular configuration of the magnetic field and the carrier spin polarization (Voigt geometry) would not result in a build up of a nuclear spin polarization. In a semiclassical picture, the carrier Larmor precession averages to zero, from the perspective of the, far slower, nuclear spin dynamics. The maximal nuclear spin polarization could be achieved in a pure Faraday configuration. However, in a pure Faraday geometry no Larmor precession occurs, and one could not measure the amount of the Larmor frequency change, as a result of the build up of an Overhauser field. Hence, as compromise, the magnetic field is inclined from the Faraday geometry towards the Voigt direction, by an angle of $\theta = 60°$. Further, the sign of the nuclear polarization depends on the sign of the carrier polarization, i.e. the helicity of the pump beam. Thus, in order to avoid an effective averaging effect, it is needed to install a constant helicity excitation and avoid, as commonly used, an excitation with an alternating helicity. In Fig. 4.3.2**a**, two TRKR signals are shown, measured in similar conditions, with only a changed helicity of the pump beam. While for the right circular polarized light, σ^+, within 3 ns, only two and a half oscillations for the hole spin precession are observed. In case of the left circular (σ^-) polarized light, the amount of oscillations is tripled, seven and a half full oscillations are observed. For the electron spin precession, the effect is weaker. A fit of the TRKR curves confirms a change of the hole Larmor frequency, $\omega_{\mathrm{L,h}} = 16$ rad ns^{-1} for σ^- and 5 rad ns^{-1} for σ^+, and for electrons $\omega_{\mathrm{L,e}} = 28$ rad ns^{-1} for σ^- and 32 rad ns^{-1} for σ^+.

The nuclear spin dynamics is assumed to be slow, and can be directly measured, when the helicity of the pump beam is changed. In Fig. 4.3.2**b**, a slow exponential change of the DNP with a time constant of $\tau = 5.5$ s is shown. For this experiment, the KR signal was recorded at a constant time delay of 0.5 ns and the pump helicity abruptly switched. The repolarization time of nuclei is comparable to the times observed in III-V or II-VI semiconductors [Vla17; Hei16].

According to Eq. (4.3.1), the nuclear polarization is further proportional to the carrier spin polarization magnitude. An increase in the pumping power, as shown in Fig. 4.3.2**c**, leads to an increase of the carrier spin polarization and thus also to an increase of the nuclear spin polarization. In turn, it increases the Larmor frequency, due to the rising Overhauser field. The change of the TRKR signal from a low pumping power of 4 mW towards high pumping power of 30 mW is traced by dashed lines, Fig. 4.3.2**c**. A strong decrease of the hole Larmor frequency is seen, while for the electron, it slightly increases.

From the Larmor frequency, the Overhauser field can be calculated, as halved Larmor frequency difference between the helicities normalized with the corresponding g-factor

$$B_{\mathrm{N,h(e)}} = \frac{\hbar}{g_{\mathrm{h(e)}} \mu_B} \frac{\omega_{+,\mathrm{h(e)}} - \omega_{-,\mathrm{h(e)}}}{2}. \tag{4.3.2}$$

The calculated values are shown in Fig. 4.3.2**d**–**e**. The Overhauser field for holes approaches a value of up to 50 mT while for electrons, it reaches ten times less, up to 5 mT. This is in accordance with the theoretical assumption of a higher nuclear interaction of holes as compared to electrons. Further, the opposite directionality ($\mathrm{sgn}\,(B_{\mathrm{N,h}}) = -\mathrm{sgn}\,(B_{\mathrm{N,e}})$) of the Overhauser field is in line with the opposite carrier g-factor sign $g_e > 0$ and $g_h < 0$ for $FA_{0.9}Cs_{0.1}PbI_{2.8}Br_{0.2}$, see Sec. 2.4.
Interestingly, the Overhauser field build up with excitation power is almost linear for electrons while it shows a saturating dependence for holes. Further, an increase of the bath temperature from $T = 1.6$ K to $T = 6$ K, leads to a damping of the Overhauser field experienced by the hole spin after its saturation point. The damping of the Overhauser field is given by a change of the leakage factor, depending on the temperature and the pumping power, see Sec. 2.4. The different dependencies of the Overhauser field for electrons and holes show clearly, that different nuclei affect them. Either the nuclear type needs to be different, or if the type is identical, at least the electrons and holes need to be localized on different sites. Both scenarios seem likely, therefore, in a next step, the nuclear type will be identified.

4.4 Optically-Detected Nuclear Magnetic Resonance

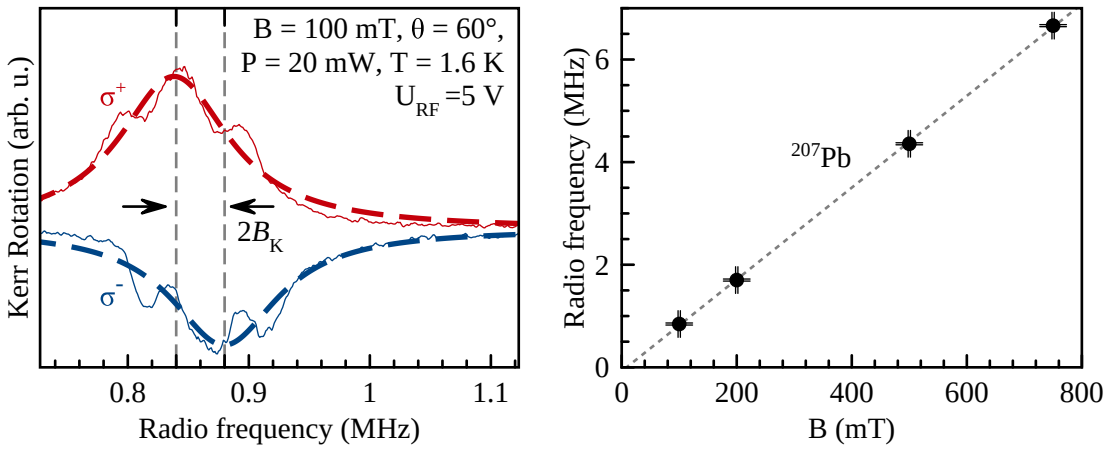

Figure 4.4.1 Optically detected nuclear magnetic resonance (ODNMR). a, ODNMR resonance of ^{207}Pb for σ^+ (red line) and σ^- (blue line) pump measured at time delay of $t = 960$ ps and pump power of 20 mW, $T = 1.6$ K, $B = 100$ mT ($\theta = 60°$ and $\varphi = 0°$) and radio frequency driving with $U_{\mathrm{RF}} = 5$ V. Curves are fitted (dashed lines) with single Lorentzian peaks, neglecting the visible comb like structure on the ODNMR signal. The difference in central RF frequency for σ^+ and σ^- ODNMR curves are indicated by vertical dashed lines and arrows show the Knight field B_{K}. **b**, ODNMR resonances (average value between σ^+ and σ^-) (dots) with linear fit (dashed line). The fit gives a slope of 8.80 MHz/T in accordance with the nuclear magnetic resonance frequency of ^{207}Pb.

The polarized nuclear spins also exhibit a Zeeman splitting. As it is three orders smaller than the carrier Zeeman splitting, $\mu_B = 57.65$ μeV/T $\gg \mu_N = 0.03152$ μeV/T, it ranges, in a magnetic field of hundreds of millitesla, in the radio frequency range of kHz to MHz. Such frequencies can be easily applied by small coils, giving a radio frequency excitation

of the sample, see also Sec. 3.3.2.5 and the illustration in Fig. 4.4.2**a**. In the case if the radio frequency is resonant to the specific Zeeman splitting of an isotope, these nuclear spins get depolarized. Thus, the Overhauser field acting on the carrier spins decreases, and in turn, a change of the carrier Larmor frequency can be observed. In Fig. 4.4.1, the signal of such an optically detected nuclear magnetic resonance (ODNMR) experiment is shown. A time delay of 960 ps was installed under conditions, where a DNP is present ($\theta = 60°$, $B = 100$ mT, pump 20 mW either σ^+ or σ^-) and the radio frequency, with an amplitude of 5 V, swept. A pronounced peak at 0.840 MHz for σ^+ and at 0.880 MHz for σ^- pump helicity is observed. In average, the resonance occurs at 0.860 MHz, whereas the 20 kHz difference can be attributed to the polarized carriers, providing an effective magnetic field, the Knight field, of $B_K = 2$ mT to the nuclear spins. The radio frequency peak, corrected for B_K, shifts in the magnetic field linearly, Fig. 4.4.1**b**, with a slope of 8.880 MHz/T. From the abundant isotopes in $FA_{0.9}Cs_{0.1}PbI_{2.8}Br_{0.2}$, lead (^{207}Pb) and iodine (^{127}I) have a vacuum nuclear magnetic ratio in the vicinity to the observed value, ^{207}Pb of $\gamma = 8.882$ MHz/T (natural abundance of 22.1%, $I_{Pb} = 1/2$) and ^{127}I with $\gamma = 8.578$ MHz/T (natural abundance of 100%, $I_I = 5/2$) [Dra83]. The gyromagnetic ratio of lead is closest to the experimental value but also doesn't match exactly. It is known that the gyromagnetic ratio, in a material, may differ to the value in vacuum, e.g. shielding of the nuclear spins, known as chemical shift, needs to be taken into account. For metallic lead, the chemical shift reaches values up to -11 kppm, giving an effective gyromagnetic ratio of 8.784 MHz/T [Wra90]. Further, in Fig. 4.4.2, it is shown, that the nuclear resonance occurs for hole spins. For hole spins, a dominant interaction with lead, rather then with iodine, is predicted from the respective orbital contribution, see Sec. 2.4.1. In conclusion, lead ^{207}Pb spins can be identified as major nuclear hyperfine interaction contributors. In the ODNMR signal, side peaks are seen. In the magnetic field dependence, those side peaks show a constant separation towards the central peak position, and don't shift with the increase of the RF power, and only change if the RF signal is amplitude modulated. As ^{207}Pb has a spin 1/2, quadrupole effects and also, from the absence of an RF power dependence, Rabi oscillations can be excluded. The satellite peak distance is stable in all measured magnetic fields, so a specific RF resonance of the coil is excluded. Overall, the origin of those side peaks is not clear yet. A comparable, but not equal, phenomenon was discussed in the literature in the framework of a nuclear scalar coupling [Aeb20]. The scalar coupling shows a much smaller separation of the side peaks and seems not to be the origin for the side peaks observed in this work.
The full width half maximum (FWHM) of the ODNMR peak, Γ_N, is not a result of the narrow RF line width, but rather originating by the inhomogeneous broadening by the nuclear spin dynamics. The nuclear spin dynamics can be estimated to $T^*_{2,Pb} = 1/(\pi\Gamma_N) \approx 3$ μs [Jam75].

4.4.1 Time-Resolved Kerr Rotation Signals with Applied RF

The effect of a, carrier specific, depolarization of the DNP can be visualized by recording of time resolved Kerr Rotation spectra with and without an applied resonant RF field, Fig. 4.4.2**a**. Here, in a higher magnetic field of $B = 750$ mT, $\theta = 60°$ the ODNMR resonance is obtained at higher frequencies of 6.66 MHz. The corresponding ODNMR spectrum is shown in Fig. 4.4.2**b**. It was recorded for a time delay of 320 ps. The TRKR spectra, Fig. 4.4.2**a**, were fitted and both electron and hole components separately plotted in Fig. 4.4.2**c-d**. The Overhauser field acting on holes is significantly reduced with the

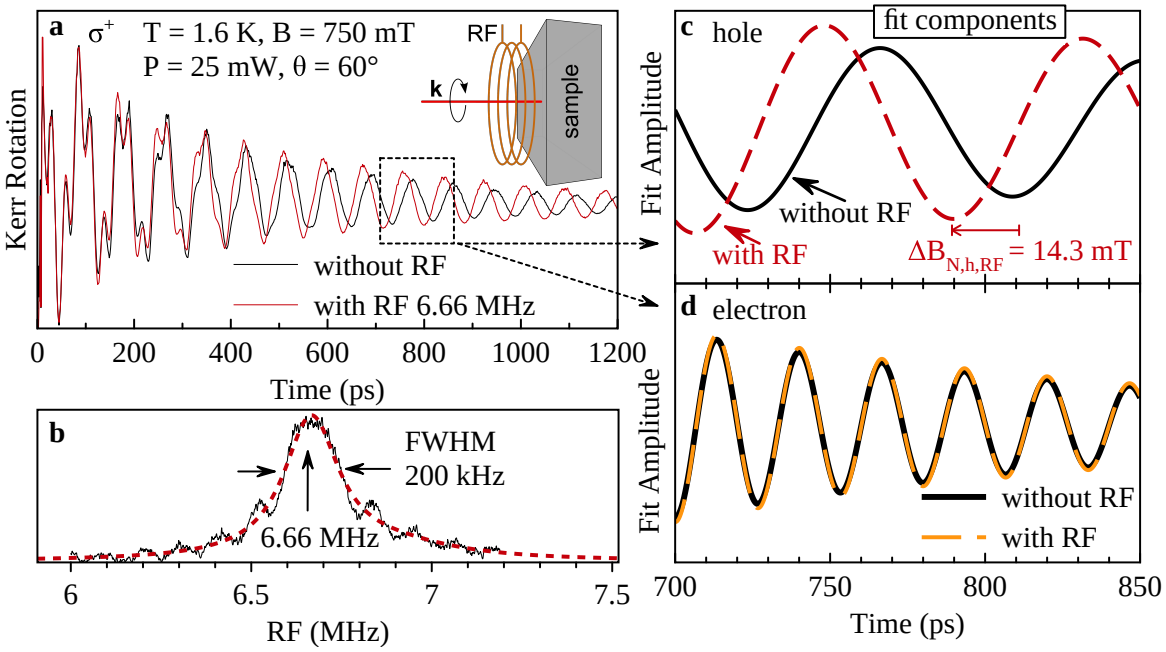

Figure 4.4.2 Effect of RF on DNP. a, Example of time-resolved KR signals with (red) and without (black) resonant RF radiation at 6.66 MHz for $B = 750$ mT and $P = 25$ mW of σ^+ polarized pump. $T = 1.6$ K. **b**, ODNMR resonance at given field, 200 kHz FWHM. $t = 320$ ps. RF amplitude was amplified. **c-d**, Fit components after decomposition for hole (**c**) and electron **(d)** at long time delays. For the hole (dashed red and black lines) the difference is evident, while for the electron (solid black and dashed yellow line), no change is visible. Dashed lines are with RF applied, solid without.

applied RF field, $\Delta B_\mathrm{N} = B_\mathrm{N}(\mathrm{no\,RF}) - B_\mathrm{N}(\mathrm{with\,RF}) = 14.3$ mT, from an Overhauser field $B_\mathrm{N}(\mathrm{no\,RF}) = -37.3$ mT, corresponding to a change of 40%. For the Overhauser field acting on the electron spins, the change is nearly invisible. The Overhauser field changes by 5% from $B_\mathrm{N,e} = 3.8$ mT by an amount of $\Delta B_\mathrm{N,e} \approx 0.18$ mT.

The results suggest that the DNP arises from different isotopes. In the pump probe scheme, a repetitive spin excitation is present. With a certain probability, a carrier spin excitation affects a carrier close to a nucleus site where previously a carrier of the opposite type was excited. For instance, an excited hole could flip with a lead isotope, relax and within the long lifetime of the nuclear spin, an electron could be excited at a similar place, now interacting with the excited nuclear spin and being affected by an Overhauser field. As the RF is affecting all lead spins, and if the Overhauser field for an electron spin would be given by lead, the same relative decrease of the Overhauser field with applied RF power should be observed as for the hole spins. As this is not the case, it can be assumed, the Overhauser field experienced by electron spins is most likely originated by the small *s*-orbital admixture of the halogen, here iodine, spins.

The iodine spins are most likely less sensitive to a RF field as to their spin is higher than 1/2 and thus obtain a non zero quadrupole moment [Dra83; Piv20].

4.4.2 ODNMR Anisotropy

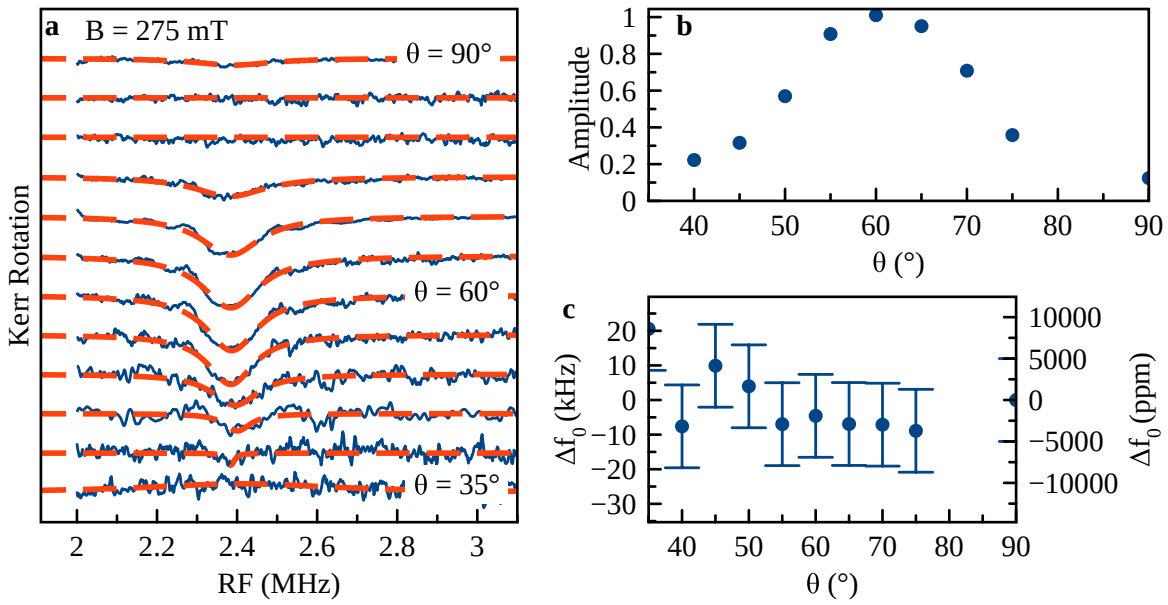

Figure 4.4.3 ODNMR anisotropy. **a**, ODNMR signals (blue line) for different angles θ of the external magnetic field, in horizontal plane $\varphi = 0°$. $B = 275$ mT, $T = 1.6$ K, $P = 25$ mW, 613 ps time delay and σ^- pump polarization. All curves are shifted vertically for clarity. The red dashed line shows a fit of the resonance with a Lorentz dip on top of an offset. Resonance FWHM is 170 kHz. **b**, Amplitudes of the ODNMR signal normalized to the maximum. **c**, Relative shift of the central ODNMR peak positon $\Delta f_0 = f_\theta - f_{90°}$, $f_{90°} = 2.39$ MHz. Right axis is linear scaled in parts per million (ppm).

Analogue to the g-factor anisotropy of carrier spins, also the nuclear spin gyromagnetic ratio might be anisotropic, e.g. an anisotropic chemical shift might be present [Sha87; Nol77]. In Fig. 4.4.3**a**, a series of ODNMR curves under rotation of the magnetic field angle, between the Faraday and the Voigt geometry, in horizontal plane is shown. The set of curves was measured at a time delay of 613 ps, with a magnetic field vector length of 275 mT, a bath temperature of 1.6 K and a constant helicity of σ^- 25 mW pumping. The curves were fitted with a single Lorentzian type dip and the dip amplitudes and the central positions plotted versus the magnetic field angle in Fig. 4.4.3**b-c**, respectively.
The amplitude shows a pronounced dependence over the magnetic field angle, peaking around an angle of $\theta = 60°$, and decreases for both increasing and decreasing angles. This dependence reflects the optimum, which needs to be found between Faraday and Voigt configuration for a high DNP together with a good ODNMR detection. For the highest achievable DNP an angle close to Faraday magnetic field is preferential, while for an optimal readout, an angle close to Voigt magnetic field is optimal [Kal91].
The ODNMR anisotropy is shown as a difference to the ODNMR frequency at $\theta = 90°$, $\Delta f_0 = f_\theta - f_{90°}(2.391$ MHz), in Fig. 4.4.3**c**. Within an estimated experimental accuracy range, the resonance frequency is nearly isotropic. As comparison, the ODNMR FWHM is 170 kHz broad and the magnetic field reproducibility better then 0.5 mT (0.2%). However, with the estimated ODNMR anisotropy, in the order of hundreds or thousand parts per million (ppm),

a certain deviation from the isotropic behaviour is found. Still, no clear trend is visible, thus one can consider the ODNMR resonance, and therefore also the nuclear gyromagnetic ratio, as isotropic. This is in agreement with an isotropic s-type hole orbital and a lead spin of 1/2.

4.5 Summary/Discussion

For the first time, the carrier spin dynamics in a hybrid organic FA based lead halide perovskite was observed. Both carrier spins of the electron and the hole were observed and show relatively high g-factors. For the hole spins, $g_h = -1.21$ and for the electron spins $g_e = 3.57$. The absolute values will be explained in Ch. 6 with the use of the modified Roth equation (Ch. 2). The relatively long spin precession, $T^*_{2,0,e} = 8$ ns and $T^*_{2,0,h} = 5.5$ ns, exceeds the exciton life time and can be attributed to resident carriers. The dephasing time was shown to be affected by a magnetic field applied in Voigt geometry, with a characteristic spread of g-factor $\Delta g \approx 1.7\%$ and by temperature with a relatively low activation energy of $E_A = 2.9 - 3.8$ meV. Further, in this study the hyperfine interaction was explored. A pronounced dynamic nuclear polarization for holes and electron spins was observed. A measurement of an optically detected nuclear magnetic resonance lead, to the identification of the lead nuclear spin as dominant contribution. While the linear combination of the atomic orbitals suggests that the energy level of the valence band is dominated by the halogen atoms, the observations of a dominant hole spin interaction with lead spins suggest the dominant role of the lead $6s$ orbital at the top of the valence band.

Interestingly, the gyromagnetic ratio of lead, observed by the ODNMR experiment, shows a high chemical shift, which is absent in conventional NMR experiments [Aeb20]. Signatures of the influence of the carrier surrounding onto the nuclear resonance were found, for instance by the presence of a Knight field, shifting the nuclear magnetic resonance.

5

Carrier Spin Dynamics in $MAPbI_3$ Bulk Single Crystals

The discovery of the high quantum efficiency of methylammonium (MA, CH_3NH_3) lead iodine bulk crystals ($MAPbI_3$) motivated the proposal of lead halogen perovskites as solar cell material [Koj09; Jeo21], and initial studies on the spin dynamics in polycrystalline $MAPb(Cl_{1-x}I_x)_3$ and $MAPbI_3$ crystals [Ode17; GA21]. In this chapter, the carrier spin dynamics in single crystalline $MAPbI_3$ will be studied in a comprehensive manner. The spin dynamics of electrons and holes will be identified, the g-factors determined and a pronounced g-factor tensor anisotropy characterised. The spin dynamics exceeds nanoseconds and will be discussed in terms of the times T_2^* and T_1. Interestingly, a pronounced dynamic nuclear polarization was observed, with minute long dynamics. The findings for carrier spins will be supported by an exciton g-factor and lifetime characterization. For the measurements three samples were used. Two were of a high quality (1^{st} and 2^{nd}) while the 3^{rd} showed a tendency of polycrystalline domains. If not stated otherwise the results discussed in this chapter, were obtained with use of the high quality 1^{st} and 2^{nd} sample. The results of the spin inertia and temperature dependence of the T_2^*, were measured on the 3^{rd} sample. Historically, the 3^{rd} sample was the initial one which was studied. The results of the spin inertia and temperature dependence of the T_2^* for localized carrier spins assumed to be not strongly affected by a possible multi domain structure of this sample. However, for the g-factor anisotropy and other measurements a multi domain structure would have been crucial and thus were measured on the 1^{st} and as control on the 2^{nd} sample. The results are submitted for publication [Kir22].

5.1 Basic Optical Properties

For the measurement of the spin dynamics, it is needed to cool down the crystals to low temperatures. For $MAPbI_3$, it is known that a phase transition occurs with cooling down. Hence, as a first step it is important to understand the link between the reported room temperature crystal characteristics and the low temperature regime. A robust tool is the investigation of the photoluminescence (PL). In Fig. 5.1.1**a**, a series of PL measurements for varying bath temperature is shown. The PL was excited with a 405 nm (3.05 eV) laser, using an average power of 1.2 mW and dispersed with a grid with 1800 lines per mm, methods Sec. 3.3.1. For a high temperature (e.g. $T = 234$ K), the PL signal shows a single bell shaped

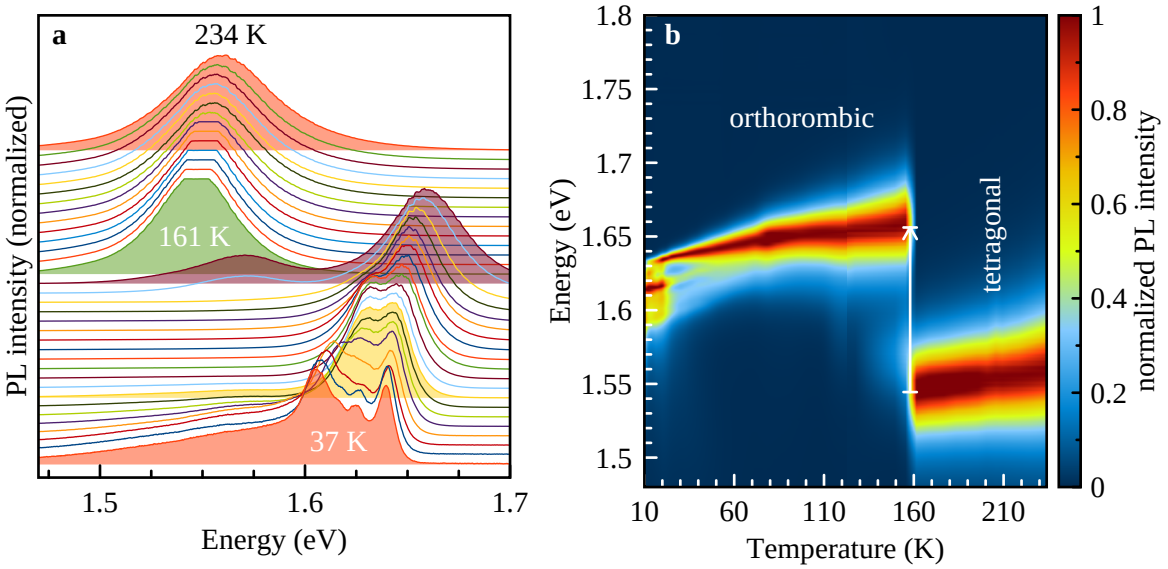

Figure 5.1.1 Temperature dependent PL. a, Photoluminescence spectra recorded for $T = 234 - 37$ K. The spectra are shifted vertically for clarity. Spectra for 234, 161 and 37 K (orange, green and red) are filled and labelled. All curves were normalized to their respective highest count. **b**, 2D colour map of PL spectra. The temperature regions of high temperature, tetragonal, and low temperature, orthorhombic crystallographic phase, are on the right and left side of the arrow and labelled respectively. Measured on the 2nd sample.

peak centred at 1.560 eV with FWHM 58 meV. The shape is neither fully Gaussian nor fully Lorentzian, but best represented by a Voigt profile, which numerically can be approximated by a linear combination of both peak shapes with equal width and central line position $f_{\text{Voigt}} = \eta \exp\left[-\ln(2)(E - E_0)^2/\Delta E^2\right] + (1-\eta) + (1-\eta) \cdot 1/(1 + (E - E_0)^2/\Delta E^2)$, reflecting a composition of numerous homogeneous and inhomogeneous line broadening effects. With decreasing the temperature, the PL central position red shifts from $T = 234$ K to $T = 161$ K by about 13.1 meV towards $E_0(161\text{ K}) = 1.547$ eV. At a temperature of $T = 155$ K, an additional peak at 1.659 eV appears, according to the 1st order phase transition of the tetragonal to the orthorhombic phase. Indeed, both phases seem to exist simultaneously in the crystal close to the transition temperature [Whi16]. For lower temperatures, the PL peak originating from the tetragonal phase vanishes and only the orthorhombic one prevails. The orthorhombic peak also red shifts with decreasing temperature, with a comparable rate of 0.16 meV/K, with an end at $T = 10$ K at 1.634 eV. With decreasing temperatures, the PL width narrows with a rate of 0.2 meV/K and a set of side peaks, located at lower energies, appears. The origin of the side peaks is most likely from shallow defects, as it will be shown, that no polarization in magnetic field will be observed for them. For illustration, a colour map representation of the PL temperature dependence is shown in Fig. 5.1.1**b**. Note, the measurements below 40 K have been carried out at a following day of those above, and thus a small mismatch in the amount of sidepeaks is observed. It might happen that another spot on the sample was used, an certain amount of defects, or stress relaxed over the time.

5.1.1 Degree of Circular Polarization

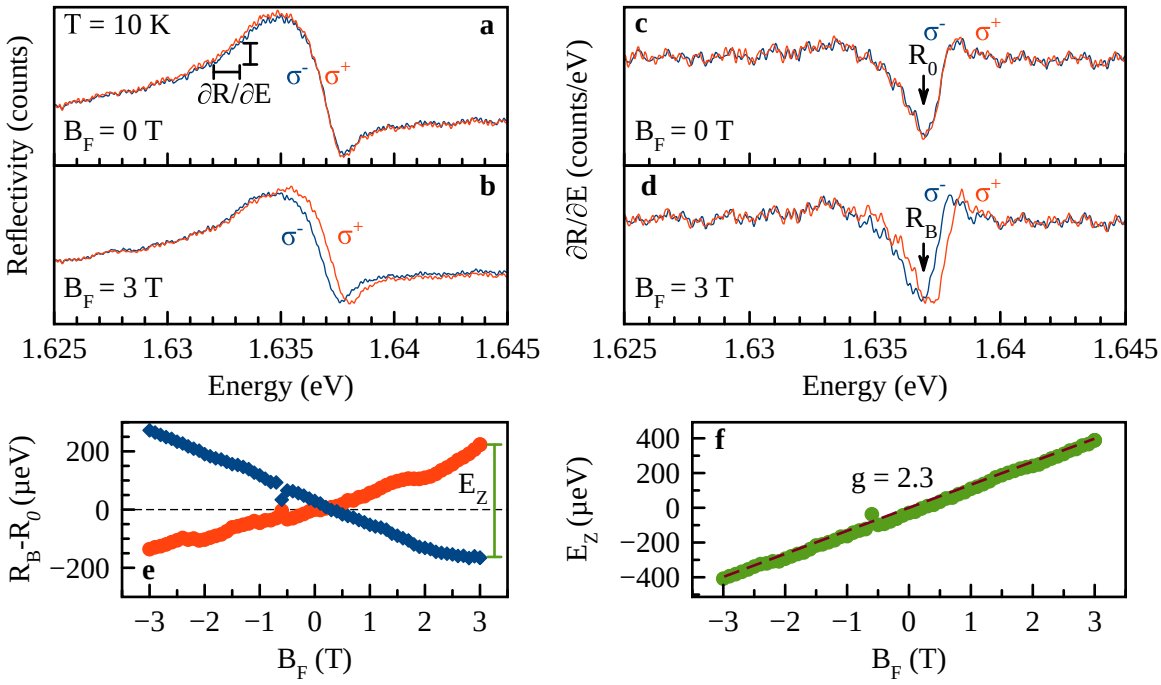

Figure 5.1.2 Magneto Reflectivity. **a**, Reflectivity spectrum recorded at $T = 10$ K using an unpolarized white halogen lamp and polarization resolved for reflected σ^+ and σ^- polarized light (red/blue). Arrows with label $\partial R/\partial E$ symbolize the numerically differentiation used for the curves in **c-d**. **b**, Signals of **a** split in Faraday magnetic field of $B_F = 3$ T. **c-d**, Signal shown in **a-b** were numerical differentiated to suppress (pseudo) linear white light background emerging from the halogen lamp and to get higher contrast for the saddle point identification. The dip maxima are labeled R_0 and R_B for zero and non-zero magnetic field. **e**, Shift of energy positions $R_0 - R_B$ versus magnetic field. Splitting of energy lines is proportional to the Zeeman splitting E_Z. The lines go linear and show no visible quadratic term arising from a diamagnetic shift. **f**, Linear Zeeman splitting (green dots) with linear fit (red dashed line). The fit gives a g-factor of 2.3. Measured on the 2nd sample.

A reflectivity spectrum for $T = 10$ K is shown in Fig. 5.1.2**a**. A characteristic dispersive profile is observed, with a width of 3 meV. For a simple and robust analysis, it is useful to numerically differentiate the curve, shown in Fig. 5.1.2**c**. In this way, the signal converts into a narrower single dip (the saddle point of the dispersive curve) which central position R_0 can be easily determined, $R_0 = 1.6369$ eV. The measurements were carried out helicity sensitive, either detecting only σ^+ or σ^- polarized light being reflected from the unpolarized, halogen lamp, source. For zero magnetic field, the amount of light which is reflected in σ^+ or σ^- is exactly the same. However, if a magnetic field in Faraday direction B_F is applied, a splitting between σ^+ and σ^- polarized reflection is appearing, shown for $B_F = 3$ T in Fig. 5.1.2**b** and the numerical differential in Fig. 5.1.2**d**. If the shift of the lines $R_B - R_0$, where R_B is the magnetic field depended numerically differentiated reflectivity dip, is traced via the magnetic field a nearly linear rise for σ^+ and a decrease for σ^- is observed, Fig. 5.1.2**e**. The

energy difference between σ^+ and σ^- reflects a Zeeman splitting with corresponding g-factor $g = E_Z/(\mu_B B_F) = 2.3$, Fig. 5.1.2**f**.

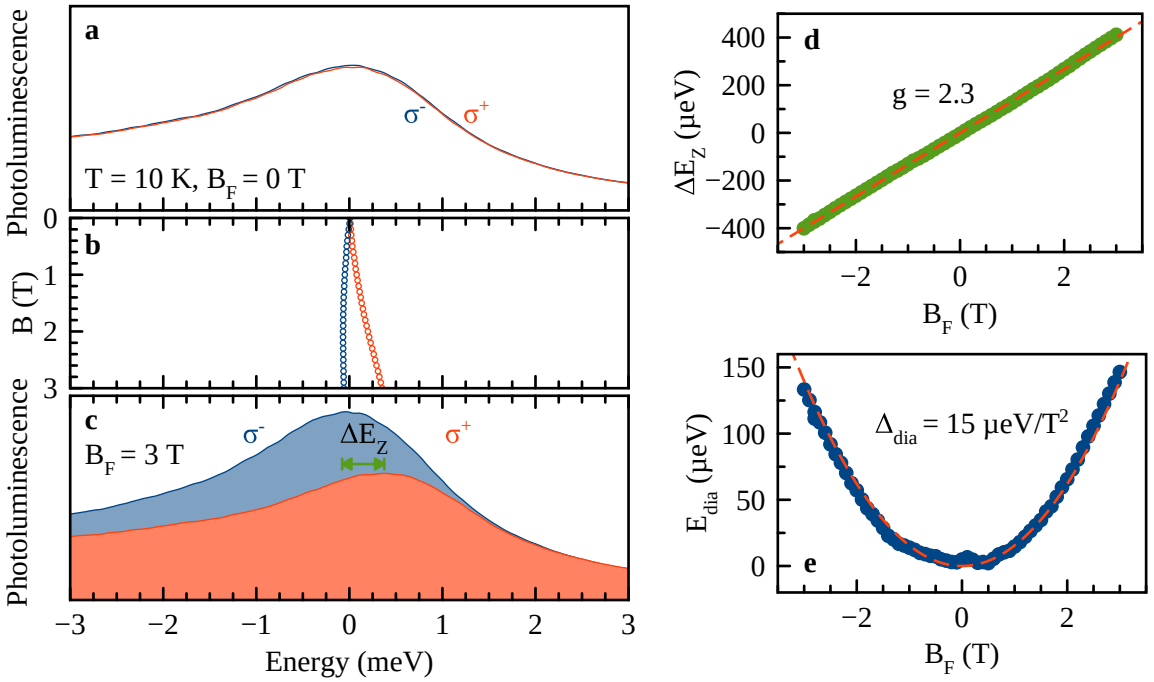

Figure 5.1.3 Magneto Photoluminescence. **a**, Photoluminescence spectrum for $T = 10$ K resolved for σ^+ and σ^- polarized light (red and blue). The spectra are shifted by energy of PL peak maximum $E_0 = 1.63485$ eV, for an easier identification of the Zeeman shift. **b**, Evolvement of PL peak maximum with rise of magnetic field B_F. Note for σ^+, the parabolic diamagnetic shift adds to the linear Zeeman term while for σ^-, the Zeeman term has reversed sign, hence both parts compensate each other resulting only in a small shift. **c**, The PL spectra for σ^+ and σ^- polarization show a splitting of their energy maxima (green arrow) and a difference in amplitude. The amplitude difference, i.e. the degree of circular polarization (DCP), is treated in Fig. 5.1.4. The linear (Zeeman splitting E_Z) and parabolic term (Diamagnetic shift, E_{dia}) in **d** and **e**. **d**, The Zeeman splitting (green line) versus magnetic field is in good agreement with a linear fit with g-factor $g = 2.3$ (red dashed line). **e**, The diamagnetic shift, calculated as the mean value of the polarization resolved PL maxima, was fitted with a diamagnetic constant $\Delta_{\text{dia}} = 15$ μeV. Measured on the 2$^{\text{nd}}$ sample.

The method of polarization resolved photoluminescence was applied for comparison. The helicity resolved detection was kept in the same configuration, but instead of excitation with a halogen white light lamp, a linear polarized 405 nm (3.06 eV) cw laser was used. The excitation energy of the laser is so high, that all polarization characteristics initialized by the excitation laser are assumed to be lost by the carrier relaxation down to the vicinity of the band gap. In Fig. 5.1.3**a**, first a PL spectrum for σ^+ and σ^- detection for a zero magnetic field $B_F = 0$ is shown. Here, only on the small range in the vicinity of the main PL emission ($E_0 = 1.6348$ eV) is zoomed, giving a rather clean but broad peak. With increasing magnetic field strength in Faraday direction (B_F), the peak splits and the amplitudes become uneven.

The difference in emission amplitudes is treated in the next paragraph, here the splitting is analysed. The non-linear shift of each peak is shown in Fig. 5.1.3**b**, reflecting a linear splitting according to the Zeeman splitting and a quadratic shift according to the diamagnetic shift. As the first is helicity dependent and the latter not, one can easily separate both effects by calculation of the average drift $E_{\mathrm{dia}} = (E_{\sigma^+} + E_{\sigma^-})/2 - E_0$, with $E_{\sigma^\pm}$ the respective peak energies (Fig. 5.1.3**e**), and the difference $\Delta E_{\mathrm{Z}} = E_{\sigma^+} - E_{\sigma^-}$ (Fig. 5.1.3**d**). The average drift is originated by the diamagnetic shift with a characteristic constant $E_{\mathrm{dia}} = \Delta_{\mathrm{dia}} B^2$, $\Delta_{\mathrm{dia}} 15\ \mu\mathrm{eV/T}^2$. The observed diamagnetic shift value is an order higher than the reported values by absorption measurements [Bar20; Hir94; Tan03], with the most recent value of $3.5\mu\mathrm{eV/T}^2$ [Miy15]. A diamagnetic shift of about $3\pm1\ \mu$eV can be also received from a fit of the previously shown reflectivity data, Fig. 5.1.2, but is not shown explicit, as it is to inaccurate.

The discrepancy between the diamagnetic shift obtained in the PL and the reflectivity could show that one resonance doesn't originate from the exciton absorption or emission but rather from something else, though a possible candidate is the appearance of an exciton with higher radial quantum number ($2s$ or $2p$) [Bla18; Bar20]. As the diamagnetic shift is influenced by several more factors only a deeper structure analysis could give an answer and is neglected here [Bug86; Gal17; Gal16; Yu16]. Still more important, and experimentally remarkable, the exciton g-factor of 2.3 for $MAPbI_3$ single crystals, was confirmed even with usage of small magnetic fields only.

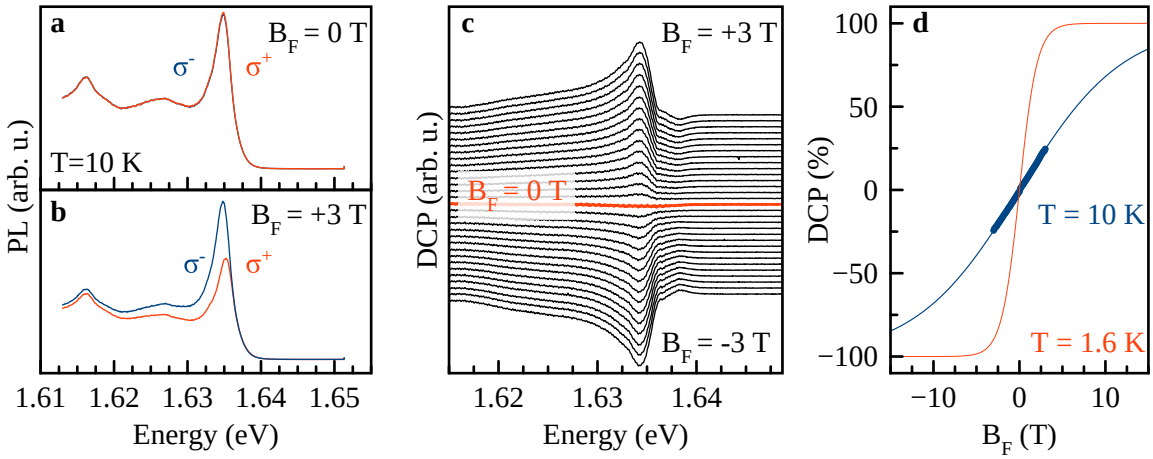

Figure 5.1.4 Degree of circular polarized photoluminescence emission. **a**, PL spectra for $T = 10$ K resolved for σ^+ and σ^- emission. **b**, In a magnetic field, the polarized PL emission splits and differs in amplitude. **c**, Spectral dependence of the DCP. From zero DCP at $B_{\mathrm{F}} = 0$ T (red line), the DCP is growing with positive sign for $B > 0$ and negative for $B < 0$. Each line represents a step of 0.2 T. The lines are shifted vertically for clarity. Note, in the DCP peaks, which were present in the PL spectrum vanished. **d**, The maximum amplitude of the DCP versus the magnetic field (blue dots). Two lines give a theoretical estimate of evolving DCP according to Eq. (5.1.1) for $T = 10$ K and 1.6 K (blue/red) with used g-factor 2.3 and $\kappa = 1$. Measured on the 2nd sample.

In Fig. 5.1.4, the magneto luminescence, previously shown in Fig. 5.1.2, is further analysed for its amplitude dependence over the magnetic field, the degree of circular polarization (DCP).

The DCP is calculated as DCP$= (I_- - I_+)/(I_- + I_+)$. One finds for zero magnetic field an absence of an amplitude difference, so no DCP, Fig. 5.1.4**a**, while for an increasing magnetic field in Faraday geometry, an amplitude difference becomes apparent, Fig. 5.1.4**b**. Interestingly, the low energy shoulder shows a much smaller difference, and also no relation to the specific peaks is present. In Fig. 5.1.4**c**, the DCP for various magnetic fields is shown. The DCP shows a smooth dependence in both, its magnetic field change, as well as its energetic dependence. The lower energy features fully vanish and thus seem to originate from unpolarized trap states or are phonon replica. The maximum DCP value is extracted and plotted in Fig. 5.1.4**d**. A linear dependence is found which is in good agreement with the expected dependence according to

$$\mathrm{DCP} = \kappa \tanh\left(\frac{g\mu_\mathrm{B}B}{2k_\mathrm{B}T}\right) \tag{5.1.1}$$

, with κ being a fitting parameter, which could take into account the exciton lifetime, but is set here to 1. $\kappa = \frac{\tau}{\tau+\tau_s}$, with τ_s the exciton spin-relaxation time and τ the exciton lifetime [Liu14; Ivc18], typically $\tau_s \ll \tau$ ($\tau_s < 10$ ns). With a decreasing temperature, the slope of the DCP should rise and saturate at smaller magnetic fields, which could be reached by the used magnet. However, a measurement series performed at $T = 1.6$ K was not successful, and needs to be further investigated.

5.2 Carrier Spin Dynamics

To turn to the spin dynamics in bulk methylammonium lead iodine, first of all, the Kerr amplitudes derived from time resolved Kerr spectra are anticipated. In Fig. 5.2.1**a**–**b**, the Kerr amplitude is shown for electron and hole spins, each taken with a time resolved Kerr measurement, like those shown in Fig. 5.2.3, with a magnetic field applied in Voigt geometry $B_\mathrm{V} = 0.5$ T and a helicity modulated $\sigma^\pm$ excitation at low temperatures $T = 5 - 10$ K. The electron and hole spin amplitudes vary from series to series and are normalized on their respective absolute amplitude maximum. The amplitude scale of a spectral series depends on the specific measurement point on the sample, the chosen pump power and other factors. However, the general spectral shape is independent on such factors and reflects the excited states. For the electron spin, in Kerr Rotation, a 2.8 meV narrow (FWHM) bell shaped dependence with a central resonance at 1.637 eV is obtained, just at the minimum of the reflectivity spectrum, i.e. at energy of highest absorption, shown in the panel below. For the hole spins, Fig. 5.2.1**b**, the Kerr Rotation shows a dispersive like profile. The ellipticity shows a bell shape with a slight expression of M-shape. The spectral amplitude dependence of the hole spin resonance is in good agreement with the theory, see Fig. 4 in [Gla12a], while the electron resonance differs. The spectral dependence of both Kerr signals reflects a full set of Stokes parameters. For the experiment, it is important to consider, that at a maximal hole signal, the electron signal is minimal and vice versa. It is beneficial to use a slightly detuned laser energy for the experiments and to optimize it according to the chosen experiment. The presented results were obtained with use of the 2$^{\mathrm{nd}}$ sample, but are in good agreement with similar measurements on the 1$^{\mathrm{st}}$ sample, which will be presented in [Kir22]. The 3$^{\mathrm{rd}}$ sample showed a superposition of multiple oscillating signals, a signature of a multi domain structure, which will be not discussed in detail.
In Fig. 5.2.1**c**, a time resolved differential reflectivity measurement is shown recorded for a

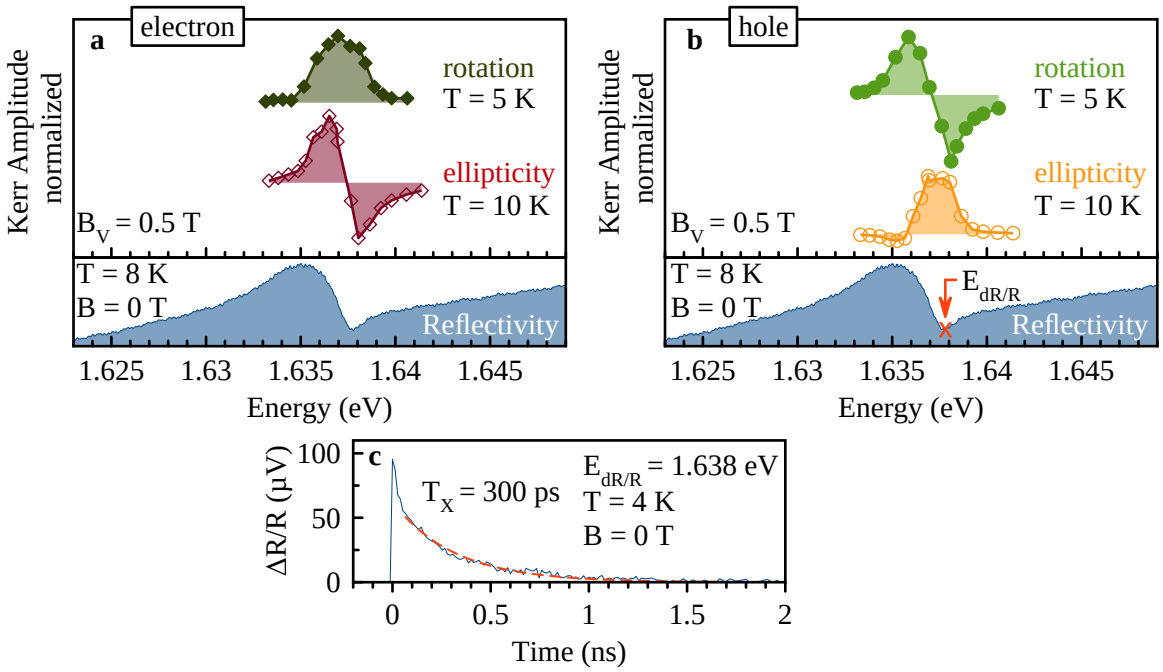

Figure 5.2.1 Carrier spin dynamics - Introduction. a-b, Spectral dependence of electron (**a**) and hole (**b**) spin Kerr amplitude in terms of rotation (green) and ellipticity (reddish). The amplitude corresponds to a spin beating at $t = 0$ ps in a Voigt magnetic field of $B_V = 0.5$ T at temperature $T = 5$ K and 10 K for TRKR and TRKE respectively. Below, the reflectivity spectrum recorded at $T = 8$ K is given as reference. **c**, Time resolved differential reflection $\Delta R/R$. The experimental data (blue line) was fitted (red dashed line) with a mono-exponential decay with an exciton lifetime $T_X = 300$ ps. The laser was set to $E_{dR/R} = 1.638$ eV, indicated by the red arrow in the lower panel of **b**. Measured on the 2^{nd} sample. The spectra are comparable to those obtained on the 1^{st} sample [Kir22].

pump and probe energy of 1.6377 eV. A single exponentially damped curve is observed with a time constant $T_X = 300$ ps, associated with the exciton lifetime.

5.2.1 Spin Relaxation Time T_1 by Spin Inertia

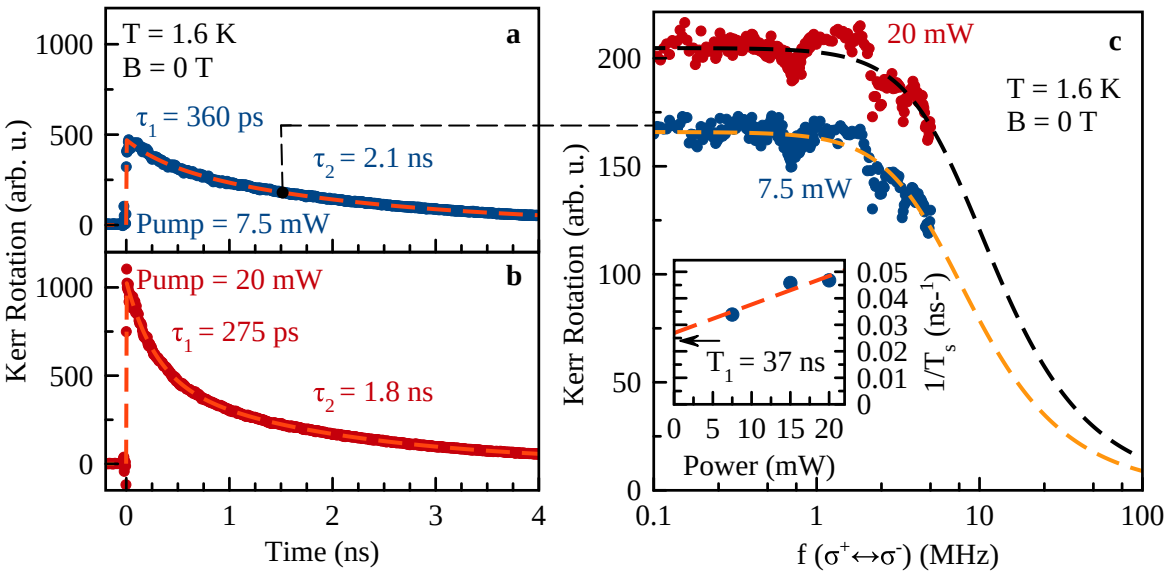

Figure 5.2.2 Spin Inertia. **a-b**, TRKR in zero magnetic field for pump powers of $P = 7.5$ mW (**a**) and 20 mW (**b**) at $T = 1.6$ K. Experimental data (symbols) were fitted with double exponential decaying curves (dashed lines). **c**, Spin Inertia curves for fixed time delay (indicated by black dashed line in panel **a**) of 1.5 ns and pump power of 7.5 mW and 20 mW (blue and red dots). Curves were fitted with Eq. (2.6.1) (dashed lines) and respective times T_s inverted and plotted in the **inset**. **inset**, inverse T_s^{-1} times versus pump power P (blue dots) with linear fit (red dashed line). The offset of linear fit is indicated by arrow and gives $T_1 = 37$ ns. Measured on the 3rd sample.

The spin relaxation time T_1 was measured with the spin inertia technique, Fig. 5.2.2. A positive time delay of 1.5 ns was installed, higher than the exciton lifetime but still short enough to not lack in sufficient signal amplitude, see Fig. 5.2.2**a**–**b**, where a double damped exponential signal is observed, with time constants $\tau_1 = 360$–275 ps and $\tau_2 = 2.1$–1.8 ns, depending on the respective pump excitation power [†]. The external magnetic field was turned off, $B = 0$ T, and the temperature set to $T = 1.6$ K. Up to the MHz range of the pump modulation frequency ($f(\sigma^+ \leftrightarrow \sigma^-)$), nearly no amplitude change is observed. A further increase of the modulation frequency, up to the limit of the electro optical modulator of 20 MHz, leads to a decrease of the signal amplitude. According to the spin inertia theory, the signal can be fitted with use of Eq. (2.6.1),

$$|L(f_m)| = \frac{2}{\pi} \frac{n_0 |S_0|}{\sqrt{1 + (2\pi f_m T_s)^2}}, \tag{5.2.1}$$

[†]Note, for reasons unknown, in the used 3rd sample a slightly higher excitation energy of 1.6489 eV was used instead of 1.638 eV. A detuning of 4 nm.

giving a power dependent relaxation time T_s of 29.5 ns and 21.8 ns for 7.5 mW and 20 mW pump power, respectively. The dependence of the inverse relaxation time T_s^-1 over the power P is $T_s(P)^{-1} = GP + T_1^{-1}$, with the spin generation rate G and the time T_1. A generation rate of $G = 1$ mW$^{-1}\mu$s^{-1} and $T_1 = 37$ ns is fitted.

5.2.2 Spin Precession - Dephasing Time T_2^* and Carrier g-factor Characteristics

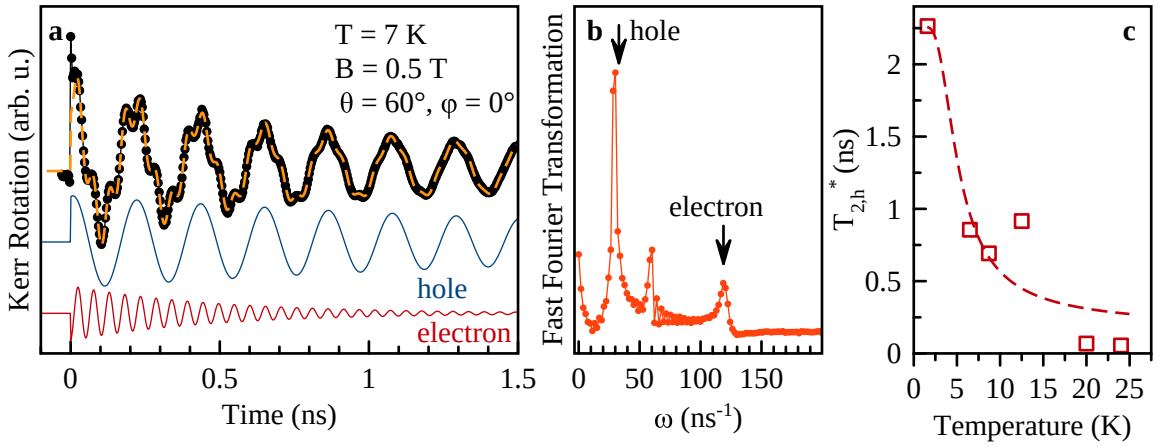

Figure 5.2.3 TRKR resolved spin precession. **a**, TRKR signal (black dots) for a magnetic field of vector length $B = 0.5$ T and an angle towards the light propagation direction $\theta = 60°$ and $\varphi = 0°$ (tilted 30° out of pure Voigt geometry at $T = 7$ K). The observed superimposed spin beatings are decomposed by fit (orange dashed line) in hole and electron beatings (blue and red line). The curves are shifted vertically for clarity. The fits give for holes $\omega_{\mathrm{L,h}} = 29.33$ rad ns^{-1}, $T^*_{2,\mathrm{h}}$=2.26 ns while for electron $\omega_{\mathrm{L,e}} = 119.94$ rad ns^{-1}, $T^*_{2,\mathrm{e}}$=0.48 ns. **b**, Fast Fourier Transform (FFT) of TRKR signal shown in **a** (red dotted line). Arrows indicate hole and electron Larmor precession frequencies. FFT and fit are in good agreement. Note, the observed peak at 60.26 ns^{-1} is a FFT artefact, originating by the finite measurement interval which gives rise to components resulted by FFT of square like signals (the second harmonic 2ω of $\omega_{\mathrm{L,h}}$). **c**, Temperature dependence of T_2^* of hole spins for $B = 0.5$ T in Voigt geometry ($\theta = 90°$, $\varphi = 0°$) (red open squares). The data is fitted with an Arrhenius-like function (dashed line). **a-b**, Measured on the 1$^{\mathrm{st}}$ and 2$^{\mathrm{nd}}$ sample with an identical result and on 3$^{\mathrm{rd}}$ with a comparable result. **c** Measured on the 3$^{\mathrm{rd}}$ sample.

The electron and hole spins can be distinguished by their specific coupling to magnetic fields via their characteristic g-factors. In a pump probe experiment, with a magnetic field aligned in Voigt geometry, the spin precession can be made visible. In Fig. 5.2.3, a time resolved Kerr Rotation spectrum is shown. Anticipating the main g-factor anisotropy axis, the magnetic field solid angle is rotated out of the Voigt geometry horizontally by 30° towards the Faraday geometry, $\theta = 60°$. Two oscillating components can be observed. A decomposition by a fit gives a hole spin component with $\omega_{\mathrm{h}} = 29.33$ rad ns^{-1}, $T^*_{2,h}(B = 0.5\ \mathrm{T}) = 2.26$ ns and an electron spin component with $\omega_{\mathrm{e}} = 119.94$ rad ns^{-1}, $T^*_{2,h}(B = 0.5\ \mathrm{T}) = 0.48$ ns. The finding can be further emphasized by a Fast Fourier Transformation (FFT), Fig. 5.2.3**b**. In the FFT (absolute of real and imaginary part), two clear resonance are found, in accordance with the fitted frequencies and widths (being proportional to inverse T_2^*). Further, a third peak in

between at $\omega = 60$ rad ns^{-1} is seen. For this frequency, no oscillation is present in the TRKR signal and the peak in the FFT disappears, as soon the damped oscillatory sinus of the hole spin is subtracted from the TRKR signal (baseline operation). The $\omega = 60$ rad ns^{-1} peak in the FFT can be fully attributed to a harmonic of the hole frequency ($\omega_\mathrm{h} = 29.3$ rad ns^{-1}), which appears from the step like ending of the TRKR signal. Further, in Fig. 5.2.3**c**, the temperature dependence of the hole spin dephasing time is shown. The drop of T_2^* follows an Arrhenius-like activation function, $\frac{1}{T_2^*(T)} = \frac{1}{T_{2,0}^*} + R\exp\left(\frac{-E_\mathrm{A}}{k_\mathrm{B}T}\right)$, with $T_{2,0}^*$ the spin relaxation time without temperature effects, R the relaxation rate, and E_A the activation energy. The corresponding TRKR series was measured a bit different than the previous in TRKR example. The 3$^{\mathrm{rd}}$ sample was used, the magnetic field was set to $B_\mathrm{V} = 0.5$ T in pure Voigt geometry and as consequence of the temperature dependence the signal was less stable. Hence, the absolute numbers of the dephasing time are a bit smaller and the relaxation time without temperature effects reaches only $T_{2,0}^* = 2.3$ ns. More important is the observation that, as like in bulk $FA_{0.9}Cs_{0.1}PbI_{2.8}Br_{0.2}$, again the TRKR signal vanishes for temperatures above 30 K, which is expressed by an activation energy of $E_\mathrm{A} = 1.3$ meV. The activation energy for the electron spin was not analysed, due to the low signal quality.

Additionally, on 1$^{\mathrm{st}}$ and 2$^{\mathrm{nd}}$ sample, a magnetic field series with an azimuthal angle of $\theta = 60°$ and one with $\theta = 150°$, with a zero altitude $\varphi = 0°$ for both were performed, at $T = 7$ K, Fig. 5.2.4. To start with $\theta = 60°$, Fig. 5.2.4**a**, the magnetic field series shows an acceleration of the spin precession beatings and an earlier disappearance of the signal with rising magnetic field. Motivated by the 90° symmetry of g-factor, a second series an azimuthally rotated field $\theta = 150°$ was performed. The TRKR signals were fitted and the corresponding Larmor frequencies for electron and hole spins plotted in Fig. 5.2.4**c**–**d** and the corresponding T_2^* in Fig. 5.2.4**e**. The non oscillating components, damped exponentials, arising from a magnetic field vector component along the z-axis are neglected here. The Larmor frequency shows a strict linear dependence in the measured magnetic field range. The extrapolation to a zero magnetic field shows a vanishing frequency offset, which was also proven by additional measurements under different magnetic field angles, not presented here. The minimal measured Zeeman splitting is as low as 9.5 μeV at 0.5 T for $\theta = 150°$. The linear dependencies of the Larmor frequency gives for the hole spin $g_{h,\theta=60°} = 0.68$ and $g_{h,\theta=150°} = 0.33$, while for the electron spin $g_{e,\theta=60°} = 2.78$ and $g_{e,\theta=150°} = 2.56$. The drop of T_2^* with an increasing magnetic field is best expressed by the linear dependence of the inverse $(T_2^*)^{-1}$, Fig. 5.2.4**f**, according to $(T_2^*)^{-1} = (T_{2,0}^*)^{-1} + \Delta g \mu_\mathrm{B} B$. The value $T_{2,0}^*$ expresses here the extrapolated time at a zero magnetic field, which needs to be taken with care, as the natural zero magnetic field limit is provided by a non vanishing nuclear fluctuation field. Thus, in Fig. 5.2.4**e**, instead of an unlimited rising of T_2^*, a saturation should be observed. The spread of g-factor is found to depend also on the magnetic field angle. For the hole spin $\Delta g_{h,\theta=150°} = 0.003$ and $\Delta g_{h,\theta=60°} = 0.008$, while for the electron spin $\Delta g_{e,\theta=150°} = 0.03$ and $\Delta g_{e,\theta=60°} = 0.04$. It is worth to note, the relative spread of g-factor $\Delta g/g$ is isotropic and for both carriers about 1%.

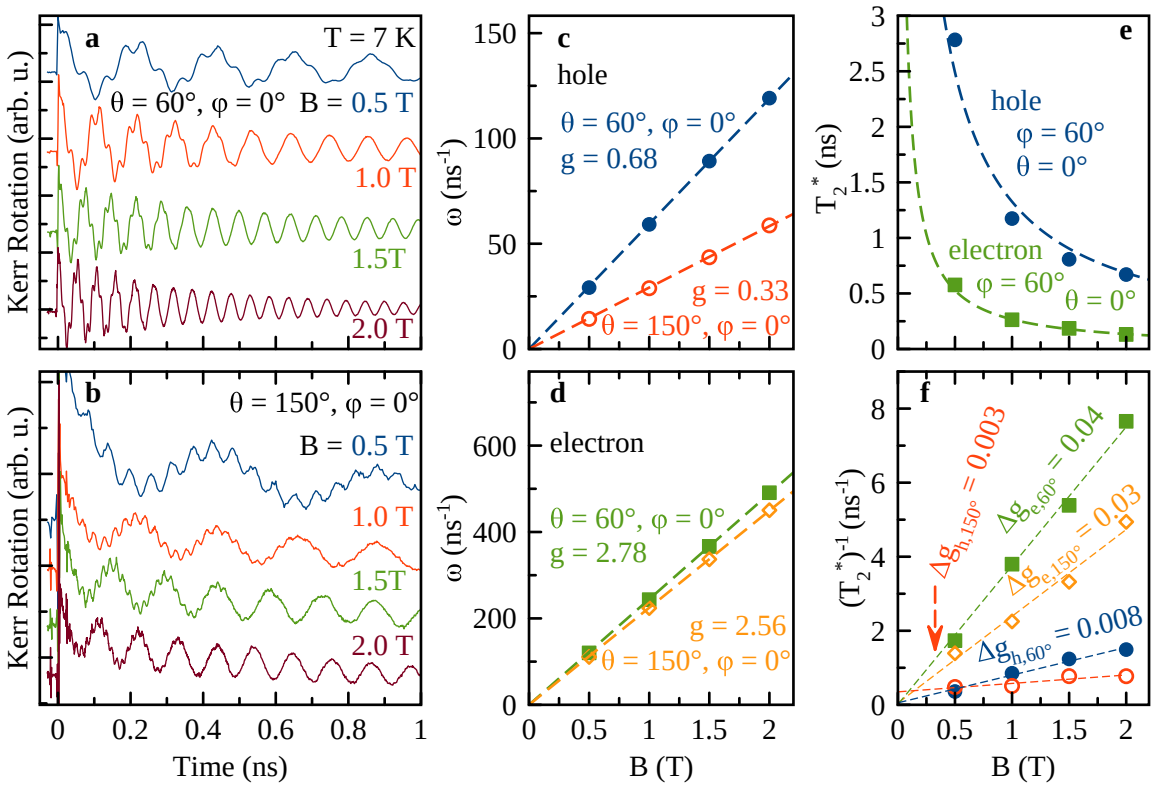

Figure 5.2.4 Carrier spin dynamics - Magnetic field dependence. a-b, TRKR spectra for rising magnetic field magnitude under an angle of $\theta = 60°$ and $\theta = 150°$ respectively, with each $\varphi = 0°$ (horizontal plane). For both measurement sets, $T = 7$ K. **c-d**, Dependence of Larmor frequency on magnetic field for (**c**) hole, (**d**) electron, with symbols for experimental data (full symbols for $\theta = 60°$, open for $\theta = 150°$) with linear fits (dashed lines). Values of fitted g-factors are given in panel (colour coded). **e** {**f**}, {inverse} dephasing time T_2^* over magnetic field (symbols) and fits (dashed lines). From the linear dependence of inverse T_2^*, a more precise evaluation can be performed. Values for the spread of g-factor $\Delta g_{e(h)}$ noted in panel. Measured on the 1st sample with an additional control series on the 2nd sample.

5.2.3 g-factor Anisotropy

In the previous section, in Fig. 5.2.4, a g-factor anisotropy in the azimuthal plane between $\theta = 60°$ and $\theta = 150°$ was observed. Indeed a smooth transition of the g-factor values between this angles exist. In Fig. 5.2.5**a**, a TRKR series for different horizontal angles is shown. Starting from a signal with two oscillating components, with an increase of the magnetic field tilt angle closer to the Faraday geometry, a non oscillating component becomes dominant. The non oscillating component does not affect the precession frequency and is neglected. More important, a significant change of the Larmor precession frequency of the slower oscillating component, the hole, is observed. If to trace the third negative beating over the magnetic field angle, it continuously shifts from >1 ns at $\theta = 150°$ towards ≈0.5 ns at $\theta = 240°$, see the circular markers in Fig. 5.2.5**a**. As optimum between the magnetic field accuracy (less sensitive to small perturbations if it is higher) and a reasonable signal strength (accelerated

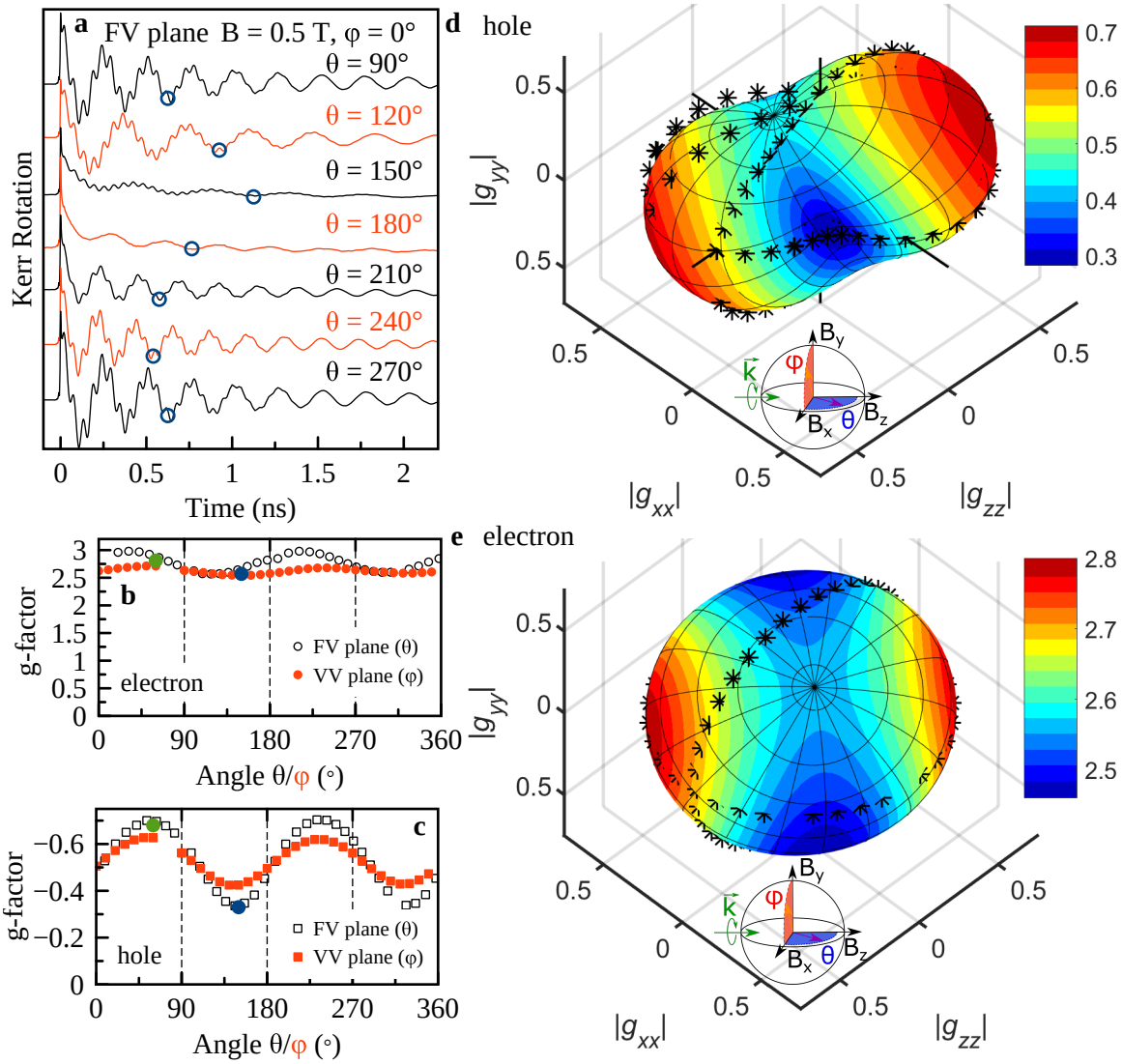

Figure 5.2.5 *g*-**factor anisotropy. a**, TRKR series with different angles (θ in Faraday Voigt plane [FV]) and $\varphi = 0°$ constant. Magnetic field magnitude $B = 0.5$ T and Temperature $T = 7$ K. The minima of the 3rd hole beating are indicated by open circles for each curve. The curves are shifted vertically for clarity. **b-c**, *g*-factors of electron and hole spins collected from the respective TRKR series like presented in **a** via fit. With black open symbols for, θ horizontal Faraday Voigt plane (FV) (azimuthal angle), and φ vertical Voigt Voigt plane (VV) (altitude angle). Note, angles of VV plane where shifted by an offset of 90° in order to have the same Voigt x-axis for both curves at angles 90 and 180°. Green and blue symbols referring to *g*-factors evaluated from series in Fig. 5.2.4**a**. **d-e**, three dimensional representation of *g*-factors for hole and electron, with stars measurement data and coloured volumes best approximation calculations representing the measurement data for illustration. With radius and colour proportional to *g*-factor value. A sketch of experimental geometric configuration is given inside, with $\vec{k}$ the direction of light incident, $B_{x,y,z}$ the laboratory frame magnetic field directions. Measured on the 1st sample with an additional control series on the 2nd sample

dephasing with increasing magnetic field) a vector length of $B = 0.5$ T was chosen. The measurements were carried out at a temperature $T = 7$ K.
The curves were fitted and the corresponding g-factors depicted versus the respective magnetic field angle, the open markers in Fig. 5.2.5**b**–**c**. Simultaneously the g-factor values for a Voigt (x-axis) to Voigt (y-axis) magnetic field rotation series are included (full markers, the respective TRKR series is not shown). For both electron and hole spins, an anisotropic g-factor dependence is found

$$g = \sqrt{(g_{\mathrm{zz}} \cos(\theta) \cos(\varphi))^2 + (g_{\mathrm{xx}} \sin(\theta) \cos(\varphi))^2 + (g_{\mathrm{yy}} \sin(\varphi))^2} \tag{5.2.2}$$

. Remarkably, the g-factor symmetry does not coincide with the laboratory frame axis defining Voigt geometry, Faraday geometry and so on. Instead, the horizontal angle $\theta_{\mathrm{e(h)}}$ needs to be rotated by $\theta_{\mathrm{h}} \to \theta + 57°$ in order to match the hole g-factor maximum and $\theta_{\mathrm{e}} \to \theta + 33°$ for electron g-factor maximum. In the Voigt Voigt plane, further $\varphi_{\mathrm{e(h)}}$ needs to be replaced by both $\varphi_{\mathrm{h}} \to \phi + 54°$ and $\varphi_{\mathrm{e}} \to \varphi + 54°$.
A three dimensional interpolation surface, Fig. 5.2.5**d**–**e**, illustrates the g-factor anisotropy. For the hole, a peanut like shape with oblique symmetry axis is observed while for electron the shape is more sphere like and only slightly elliptical. The g-factor tensors

$$g_e = \begin{pmatrix} 2.56 & - & - \\ - & 2.46 & - \\ - & - & 2.80 \end{pmatrix}, \quad \text{and} \quad g_h = \begin{pmatrix} -0.71 & - & - \\ - & -0.44 & - \\ - & - & -0.28 \end{pmatrix} \tag{5.2.3}$$

were found.

5.2.4 Dynamic Nuclear Polarization (DNP)

For low temperatures, in the regime of a localized carrier, the interaction with nuclear spins is dominant. While for most situations, a build up of nuclear polarization is suppressed, to study the nuclear spin interaction, it is also possible to drive the nuclear spins out of equilibrium and to induce a dynamic nuclear polarization (DNP). The DNP can be achieved if a constant helicity for the carrier spin excitation is used and the magnetic field is rotated towards Faraday direction. In Fig. 5.2.6**a**, an experiment is shown where the magnetic field angle was rotated out of Faraday geometry to horizontal Voigt geometry by an angle of $\theta = 60°$, magnetic field vector length 0.1 T, 15 mW pump excitation, whereas the corresponding helicities are colour-coded. The signals for σ^+ and σ^- excitation show both two oscillating components of roughly a similar amplitude and enveloping damped exponential curve. The smaller frequency beating, from hole spins, however, shows a significant change between the two helicities, for σ^+ it is slower than for σ^-. For the faster oscillation, the electron spin, the frequency dependence is reversed, slower for σ^- than for σ^+. All four frequencies are extracted by fitting and plotted separately. The frequency difference $\Delta\omega = \omega_+ - \omega_-$ can be directly related to the appearance of an Overhauser field B_{N} due to the presence of a dynamic nuclear polarization. The Overhauser field adds or subtracts to the external magnetic field, increasing or lowering the carrier Larmor precession. The Overhauser field can be calculated to $B_{\mathrm{N,e(h)}} = \Delta\hbar\omega/(2g_{\mathrm{e(h)}}\mu_{\mathrm{B}})$, with $g_{\mathrm{e(h)}}$ the absolute electron and hole g-factors $g_{\mathrm{e}} = 2.7$ and $g_{\mathrm{h}} = 0.5$. Note, for calculation, the g-factor sign was not taken into account in order to

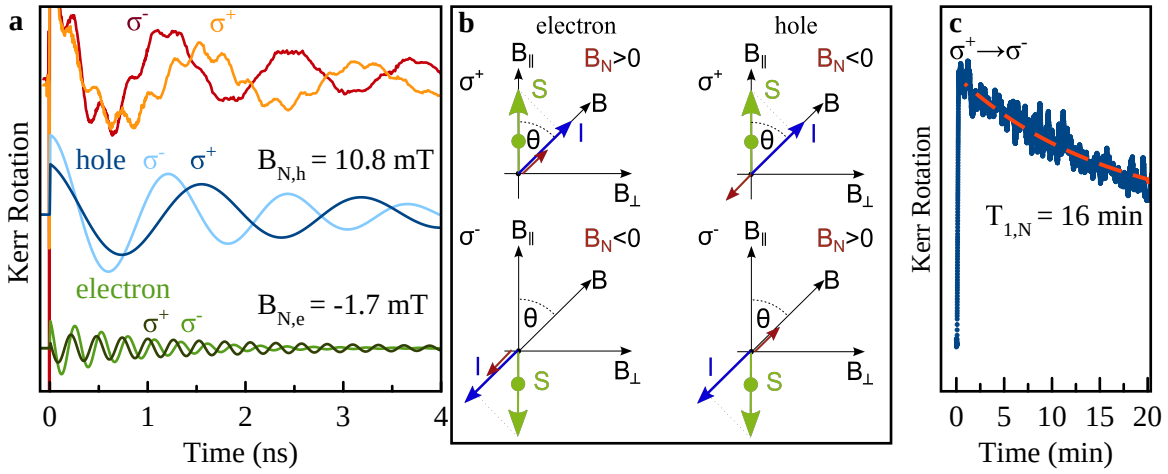

Figure 5.2.6 Dynamic nulcear polarization (DNP). a, TRKR signals (red, orange) for constant σ^- or σ^+ polarization of pump beam, respectively. Magnetic field is inclined $B = 100$ mT, $\theta = 60°$, $\varphi = 0°$, $T = 1.6$ K, under strong pump beam intensity with $P = 15$ mW. The curves were fitted with two superimposed oscillating components, which are plotted individually, vertically shifted below. The difference in oscillation frequencies for σ^- to σ^+ (hole light blue and dark blue, electron light green and dark green) originates from dynamic nuclear polarization. The DNP gives rise to an Overhauser field $B_{\mathrm{N,e(h)}}$ increasing or lowering the Larmor precession, see sketch in panel **b**. The calculated Overhauser fields are $B_{\mathrm{N,h}} = +10.7$ mT and $B_{\mathrm{N,e}} = -1.7$ mT. **b**, sketch of the process of DNP. If the carrier spin polarization S (green arrow) has a non zero projection onto the magnetic field direction B (black arrow) with azimuthal angle $\theta \neq 90°$, a nuclear spin polarization I occurs (blue arrow) in direction of B. If the carrier g-factor is positive (electron case) a nuclear polarization parallel to B, for σ^+ pump polarization, gives rise to an additive Overhauser field B_{N} and to a subtractive one in the anit-parallel case. The situation is vice versa for a negative g-factor, hole case, for parallel I to B, the Overhauser field is subtractive while it is additive for anti-parallel orientation. **c**, a constant time delay was installed, $t = 3.4$ ns, with conditions as in **a** and the pump polarization rapidly changed by rotation of a $\lambda/4$ retarder from σ^+ to σ^-, while the Kerr signal was recorded. The change of the polarization causes a rapid flip of the polarization sign accompanied by a slower continuous shift as the nuclear polarization reverses. The curve follows a mono exponential decay with a time constant $t = 16$ min, being representative for the nuclear lifetime under illumination. Note, the KR zero amplitude level is in the middle of the graph but likely originates from scattered light and is not shown. Measured on the 2nd sample.

illustrate the directionality of the Overhauser field, and the values taken as average values between the anisotropy axis.

The sketch how the DNP builds up, is shown again in Fig. 5.2.6**b** for convenience and a detailed explanation is given in the theory Sec. 2.4.

The nuclear dynamics is assumed to be much slower than the carrier dynamics, and may even reach minutes or hours. In a simple experiment, it can be measured for the present case. A time delay of 3.43 ns was fixed and, rapidly, the laser polarization changed from σ^+ to σ^- while the Kerr signal is recorded over time. A rapid change, as for the carrier polarization change, is observed, followed by a slow decaying signal, as the Larmor frequency of the hole spins change when the DNP builds up. The time constant was fitted with an exponential,

giving a time constant of $T_{1,N} = 16$ min, which can be assumed as longitudinal nuclear relaxation time. Note, in literature, typically the nuclear relaxation time is distinguished between a relaxation time in darkness and one under illumination, i.e. in presence of a carrier polarization background. The relaxation time in darkness was not measured here [Hei16].

5.3 Summary/Discussion

A pronounced carrier spin dynamics in $MAPbI_3$ single crystals was observed. In fact, the spin dynamics are comparable with $FA_{0.9}Cs_{0.1}PbBr_{0.2}I_{2.8}$ single crystals. Both show a spin relaxation T_1 of tens of nano seconds and a dephasing on the nanosecond scale. For both, a low activation energy and about 1% spread of g-factor were observed. Also, the dynamic nuclear polarization was achieved, giving rise to an Overhauser field of 10.8 mT and -1.7 mT for hole and electron spins, respectively. Interestingly, the build up time of a the DNP is on a scale of minutes in $MAPbI_3$, and significantly prolonged in respect to the seconds time scale observed for $FA_{0.9}Cs_{0.1}PbBr_{0.2}I_{2.8}$ single crystals.

The most astonishing aspect arises from the carrier g-factor anisotropy. Both carrier g factors show a pronounced anisotropy, being close to each other in absolute numbers between 0.3 – 0.5, but strongly differ in relative terms. Further, the main g-factor symmetry axis are tilted in respect to the laboratory frame. While a theoretical estimate, eqs. (2.1.12-2.1.15), suggests an interconnected g-factor anisotropy between the electron and hole by a conduction and valence band mixing, and can provide an understanding of the similar absolute g-factor anisotropy values (the tilting of the g-factor symmetry axis need to originate from a different source, not clarified yet). One reason might be a hidden crystallographic phase transition to a monoclinic system, or the misidentification of the front facet pointing along (200) and in fact being (112), as discussed in Sec. 3.2.5.1, or it might originate from a non orthogonal reorientation of the crystallographic axis, in the phase transition from tetragonal to orthorhombic system. The latter is backed from observation of [Whi16], where it was shown that from the tetragonal case with $a = b < c$, the axis configuration changes to $a \approx b \gg c$ and an explicit rotation matrix is even given in [Swa03]. Still, this matrix could not fully explain the transition. One still would need to assume, that the crystal had an initial rotation of 45° in the vertical plan. This is plausible, as the crystal was oriented with a corner pointing upwards. To conclude, no scenario could be ruled out yet. Still the experimental evidence is solid, and the g-factor anisotropy needs to be taken into account if to consider the carrier spin dynamics in $MAPbI_3$ single crystals.

6

Unified Perovskite Lead Halide Carrier g-factor

On basis of the measured single crystals, a prove of the modified Roth equation, describing the g-factor dependence in perovskites (Eqs. (2.1.8,2.1.9)), can be given. For the analysis, additional evaluations of the carrier g-factor values in other materials, e.g. of $CsPbBr_3$ [Bel19], were taken into account. The results will unify the all inorganic and hybrid organic inorganic lead halide perovskites via a shared value of the spin orbit coupling and value of the interband momentum. The results will be published in [Kir21a].

6.1 Experimental Results

The obtained g-factor values for several perovskite materials, in a wide range of visible band gap energies, are summarized in table 6.1.1. To start with the electron g-factors, the values for all compositions are above or close to the free electron g-factor of $g = 2.0023$, with a trend of decreasing g-factor with an increase of the band gap energy. The hole g-factor instead rises with increasing band gap energy, starting from negative values in the infrared region, crossing zero at about 1.8 eV (red), to a positive value. The assignment of the g-factor sign was backed by DNP measurements and the analysis of the exciton g-factor, composed of the sum of the electron and hole g-factor.
The anisotropy of the electron and hole g-factors in perovskite lead halide crystals tends to

Table 6.1.1 Electron and hole g factors for lead halide perovskite crystals at cryogenic temperatures. Minimum and maximum values are presented together with the degree of anisotropy defined as $P_{\mathrm{e(h)}} = 100\% \times (g_{\max} - g_{\min})/(g_{\max} + g_{\min})$. Note, the values for $MAPbBr_{1.5}Cl_{1.5}$ and $FAPbBr_3$ are so far unpublished and should be taken with care.

Material	E_g (eV)	g_{e}	P_{e}	g_{h}	P_{h}	Comments
$FA_{0.9}Cs_{0.1}PbI_{2.8}Br_{0.2}$	1.527	+3.48 to +3.60	2%	−1.15 to −1.22	<4%	isotropic
$MAPbI_3$	1.652 [Gal16]	+2.46 to +2.98	10%	−0.28 to −0.71	43%	anisotropic, tilted
$FAPbBr_3$	2.189	+2.47 to +2.49	0.4%	0.37 to +0.39	2.6%	isotropic
$CsPbBr_3$	2.352 [Bel19]	+1.69 to +2.06	10%	+0.65 to +0.85	13%	anisotropic
$MAPbBr_{1.5}Cl_{1.5}$	2.592	+1.47	–	–		SFRS
$CsPb(Cl_xBr_{(1-x)})_3$	2.8	–		+1.1	–	Nanocrystals

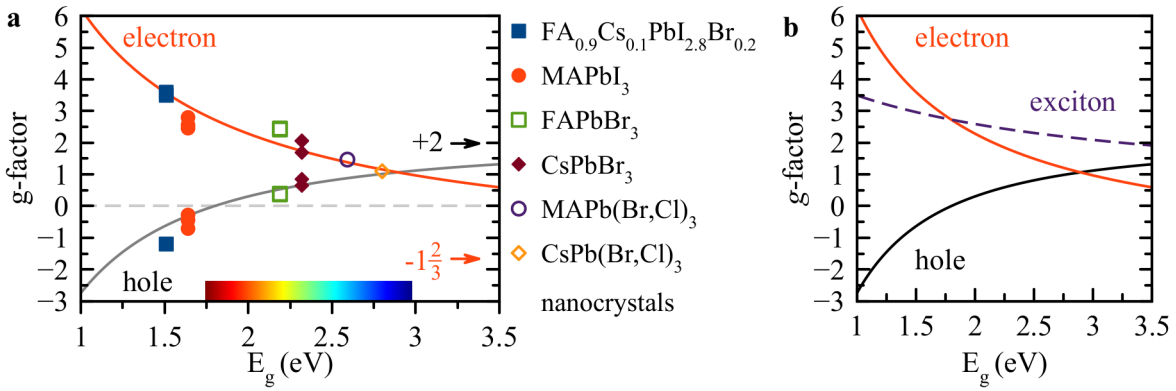

Figure 6.1.1 Unified lead halide carrier *g*-factor. **a**, Electron and hole *g*-factors versus band gap energy. For each material, the larger value corresponds to electrons the lower to hole *g*-factor. Theory curves of *g*-factor band gap dependence, after Eq. (2.1.8) and Eq. (2.1.9), are indicated by lines. **b** Theory curves as in **a** together with sum the curve of electron and hole *g*-factor, representing the exciton *g*-factor (purple dashed line).

depend on the first cation, A side of $A\mathrm{Pb}X_3$ composition, though for a precise evaluation, more perovskite compositions would be needed to be taken into account. One can see a remarkable isotropy of the *g*-factors, for FA based materials both in absolute and relative numbers. For caesium as the A cation, only data for one single crystalline sample is available, which shows the next higher anisotropy compared to FA and MA. The highest anisotropy values are observed for MA based crystals, where even the axis of the *g*-factor symmetry can tilt, see the discussion in Sec. 5.3. Note, the samples $\mathrm{MAPbBr}_{1.5}\mathrm{Cl}_{1.5}$ and $\mathrm{CsPb}(\mathrm{Cl}_x\mathrm{Br}_{(1-x)})_3$ were not included in the considerations as for the first, only a single magnetic field axis spin flip Raman scattering measurement is available and the second is a nano crystalline sample which will be discussed in next section.
The obtained values are shown in Fig. 6.1.1**a**. For illustration, the colour code was chosen to identify the material, while the marker was chosen to represent the A cation (FA,MA,Cs), the spin species, either electron or hole, and anisotropic value is only indicated by its value. Theory lines, following the equations (2.1.8) and (2.1.9)

$$g_{vb} = 2 - \frac{4p^2}{3m_0}\left(\frac{1}{E_g} - \frac{1}{E_g + \Delta}\right) \tag{6.1.1}$$

$$g_{cb} = -\frac{2}{3} + \frac{4p^2}{3m_0}\frac{1}{E_g} + \Delta g \tag{6.1.2}$$

, with parameters $\hbar p/m_0 = 6.8$ eV Å, $-\frac{2}{3} + \Delta g = -\frac{5}{3}$ and $\Delta = 1.5$ eV, are depicted[†]. The measured values are in good agreement with the theory curve. The anisotropy of each material gives a value range for the *g*-factors of each material, which is small compared to the general trend of *g*-factors.. The theory curves are also summed to form the exciton *g*-factor value, with $g_\mathrm{X} = g_{vb} + g_{cb}$. Interestingly, the strong bending of electron and hole *g*-factors upon the energy slightly cancels each other in the combined exciton *g*-factor, giving a flat, pseudo

[†] $\frac{4p^2}{3m_0} = 7.9169$ eV

linear, dependence of the exciton g-factor within values of +3 to +2 in the visible energy range. The same cancellation, of non linear terms, can be also seen in the theoretical analysis of the exciton g-factor anisotropy (Sec. 2.1.3), but is not investigated in detail.

6.2 Summary/Discussion

In this chapter, the results of the carrier spin dynamics of several single crystals were combined by their characteristic g-factors. It was shown that in the range of the visible energy spectrum, the g-factors of this materials are in good agreement with the developed theory, presented in theory Ch. 2. The theory further relies on a minimal set of parameters, the interband momentum, spin orbit splitting and, for electron spins, the remote band contribution. The general description is close to the established Roth equations, valid for a broad range of II-VI and III-V semiconductors.

It is worth to note that with this description, the perspective of an individual description of spin orbit effects in individual lead halide persovkite crystals turns to a description of a class. While it might be assumed, that the spin orbit effect differs between hybrid organic and all inorganic lead halide perovskites, now the limits for such deviations are set. For both classes, the values need to fulfil the same trends.

An individual description of those crystals is still needed, in terms of the observed g-factor anisotropy. As trend, the FA based lead halide perovskites show nearly isotropic carrier g-factors, while the all inorganic Cs and hybrid organic MA based perovskite crystals give rise to an anisotropic carrier g-factor.

7

Spin Dynamics in $CsPb(Cl_xBr_{(1-x)})_3$ Nanocrystals

So far, the carrier spin physics in bulk single crystals, in different stoichiometry, has been discussed. Another important approach to investigate the fundamentals of carrier spin dynamics in perovskites is the use of nanostructures. In this chapter, the carrier spin dynamics in $CsPb(Cl_xBr_{1-x})_3$ nanocrystals embedded in a phosphorous glass matrix is discussed.

Nanocrystals embedded in a glass matrix offer, not only, an additional path towards a fundamental understanding of the spin dynamics in lead halide perovskites, but further are also motivated by advantageous application aspects. Nanocrystals show a high quantum yield in their luminescence. While for bulk crystals, the carrier separation leads to a high light to current conversion efficiency, beneficial for solar cells, in nanocrystals, it is prohibited by the carrier confinement, which in turn enhances an efficient luminous recombination. In nanocrystals, a high luminescence quantum yield of above 90% was obtained [Kri21].

Another major advantage arises from this particular chosen nanocrystal system. While even fully inorganic lead halide perovskites, in general, are already chemically more stable, than the hybrid organic counterparts, this nanocrystals are further nearly inert, due to the surrounding glass matrix. No degradation by water can take place and also the ion migration in the about thousand atoms sized crystals is limited.

In fact, the spin dynamics in this perovskite nanocrystal system are well observable. While in general, many aspects of the spin dynamics can be already derived from the bulk properties, an important difference will be shown. In nanocrystals, a revival of a dephased spin ensemble is observed, the spin modelocking. This gives the opportunity to access T_2 and inspires for application, as the main disadvantage of nanocrystals, namely the crystal inhomogeneity in size, orientation and other aspects, can be turned into an advantage of a collective behaviour, with the use of the spin modelocking.

7.1 Linear Spectroscopy

The sample of perovskite nanocrystals in glass (internal number EK3-3), shown in Fig. 7.1.1**c**, is a below one millimetre thin, 12 mm wide, hard, yellow, glossy slab, in contrast to the relatively soft frosted single crystal samples. A sample sketch, Fig. 7.1.1**c**, illustrates the

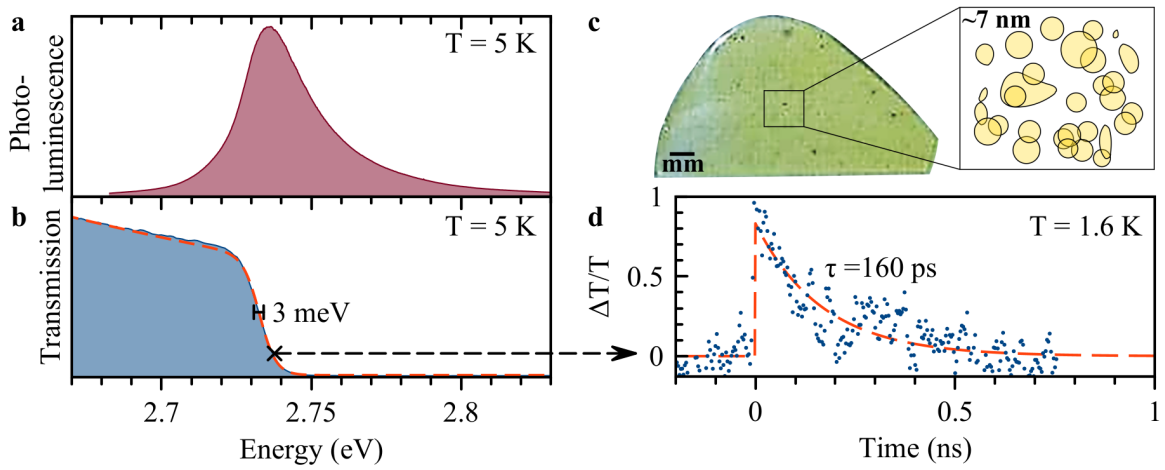

Figure 7.1.1 Linear spectroscopy. **a**, photoluminescence (PL) and **b**, Transmission spectra of the $CsPb(Cl_xBr_{(1-x)})_3$ nanocrystal sample. Transmission edge at 2.733 eV coincides with the PL maximum at 2.736 eV. Transmission edge stiffness is 3 meV, PL FWHM 27 meV. Red dashed line gives a fit according to Eq. (7.1.1). **c** Photography of the sample, length of lower edge 12 mm. Sketch illustrates nanocrystal size and shape. Average nanocrystal size of 7 nm (see Sec. 3.2.5.2). **d**, Differential transmission dynamics (blue dots) with fitted exponential curve (red dashed line) with time constant 160 ps. Note the amplitude scale is normalized to the maximum and does not represent percentage of transmission change. Laser energy is set to 2.738 eV, which is indicated by a cross and arrow in **b**.

implementation of the embedded nanocrystals in glass. In the process of melt quenching, a patternless stochastic distribution is formed. Nanocrystals don't align in a grid and will differ in size, shape and orientation. A characterisation could be performed with the use of high resolution transmission electron spectroscopy (HRTEM) but is difficult to perform for non conductive samples where a charge accumulation distract the electron beam. For this study, the characterisation is less important and only an estimate by references is used [Ary21; Liu19a; Xu21].

The yellow colour of the sample is well expressed by the transmission spectrum, Fig. 7.1.1**b**, showing a high absorption in the blue part of spectrum, with an sharp absorption edge at an energy of $E = 2.733$ eV for $T = 5$ K. This estimate of the band gap energy is, for instance, close to the one of ZnSe being also a yellowish crystal [Zhu18]. The transmission line is well described by a Fermi function

$$T = \left(\frac{A}{\exp \frac{(E-E_0)}{\Delta} + 1} \right), \tag{7.1.1}$$

with Δ being proportional to the slope of the edge (indicated by the bar in Fig. 7.1.1**b**). The stiffness of 3 meV represents a relatively short interval of the edge, the full width of the edge is approximately ≈ 15 meV.

In the photoluminescence (PL), Fig. 7.1.1**a**, one peak is observed, with the amplitude maximum at 2.737 eV. The PL maximum lays slightly higher in energy than the transmission edge,

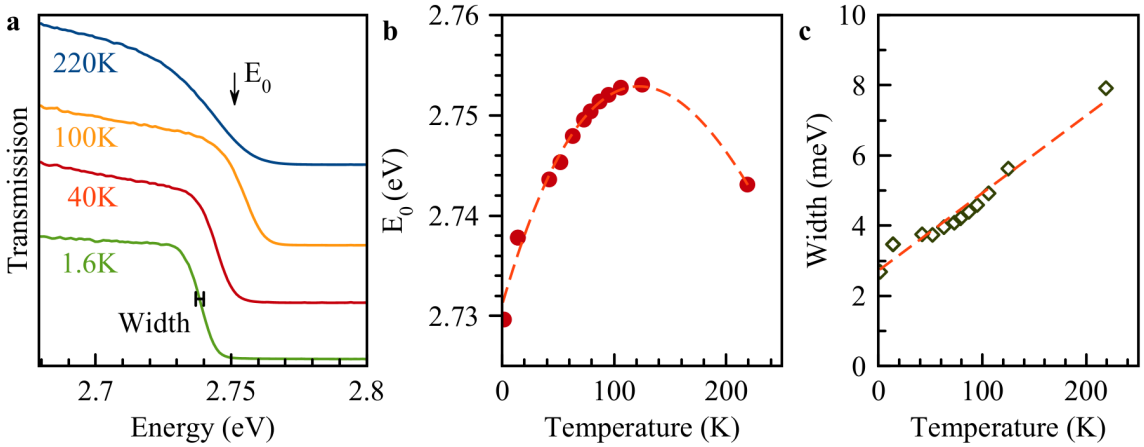

Figure 7.1.2 Temperature dependence of transmission of $CsPb(Cl_xBr_{(1-x)})_3$ NCs. **a**, Transmission spectra for various temperatures, shifted vertical for clarity. Vertical arrow indicates central energy E_0, horizontal bar stiffness of transmission line. **b**, Dependence of central energy over temperature. Data (red dots) and line for the eye (red dashed line, spline). **c**, Dependence of the stiffness of the transmission line over temperature. Data (green diamonds) and linear fit (red dashed line).

which is in contrast to an expected red shifting (Stokes shift), but however reflects the fact, that the drop in the transmission is due to the absorption by exciton states, which is then remitted as PL.

The dynamics of the transmission, measured as time resolved differential transmission ($\Delta T/T$), is shown in Fig. 7.1.1**d** with laser an energy of 2.7377 eV and $T = 1.6$ K. The differential transmission shows a single exponential decay, with a time constant of $\tau = 160$ ps. Interestingly, for this sample, no additional long decay is observed as compared to the bulk $FA_{0.9}Cs_{0.1}PbBr_{0.2}I_{2.8}$, Fig. 4.1.1**b**.

The temperature dependence of the transmission spectrum is shown in Fig. 7.1.2**a**. For a decreasing temperature, the transmission curve shifts slightly in energy and becomes more stiff. All curves were evaluated with Eq. (7.1.1) in respect of the stiffness Δ, and central energy E_0. The width narrows with decreasing temperature, Fig. 7.1.2**c**. The decrease is almost linear with a value of 3 meV at 1.6 K, up to 8 meV at 220 K and mostly originated by a decrease of the thermal line broadening.

The central energy E_0 shifts non monotonic with decreasing temperature, Fig. 7.1.2**b**. With lowering of the temperature, it first blue shifts down to 130 K and then red shifts. These findings are similar to those observed for similarly produced, pure $CsPbBr_3$, nanocrystals embedded in a glass matrix measured by G. Qiang et al. * and by [Sar17] observed for colloidal $CsPbX_3$ nanocrystals, and may indicate a phase transition of 2^{nd}-order of the nanocrystals. The transition temperature is close to the tetragonal-orthorhombic phase transition in MA-based bulk lead halide perovskite single crystals, which occurs at 160 K (see Sec. 5.1), but in contrast to observations of the phase transition temperature in Cs-based bulk lead halide perovskite single crystals [He21; Ala21; Ito79; Fuj74], for which the tetragonal to orthorhombic

*private communication, unpublished

phase transition is already observed at room temperature. In fact, several indicators suggest a significant different morphological behaviour for bulk single crystals and nanocrystals [Liu19b; Zha20b; Ala21]. For this study, it is mostly important, to understand up to which temperatures the spin dynamics might be extrapolated, to give indicators to estimate the real nanocrystal chemical composition, and further, to consider that the nanocrystals are randomly oriented in two aspects. First, by a random growing direction, so lattice orientation, and second, by the respective octahedral tilting. Even if a pseudo alignment of the crystallographic nanocrystal axis along an axis of the laboratory frame exists, e.g. for cubic nanocrystals on a flat carrier, two of the a, b, c-axis will lay in the horizontal $x - z$ plane of the laboratory system, but an octahedral tilting, e.g. $a^0a^0c^+$ in direction of c-axis, will break this axis alignment.

7.1.1 Estimate of Bromide to Chlorine Ratio

As for melt quenched grown nanocrystals, due to different evaporation points of bromide to chlorine, in the melting process an unequal amount of the halogens get lost, the ratio of bromide to chlorine, forming the nanocrystals, should be estimated by the accumulated spectral information.
For pure $CsPbBr_3$ and $CsPbCl_3$, the respective band gaps for bulk crystals are known to be 2.3274 eV at 10 K [Bel19]) (at room temperature 2.254 eV [Dir16]) and 3.056 eV at 2 K [Bar20]. A linear transition of the band gap on the halogen ratio is assumed. From the obtained transmission edge (2.733 eV) of the nanocrystal sample, a pseudo bulk value can be calculated by subtracting an amount of 86.4 meV, due to the confinement of 7 nm nanocrystals. With this numbers a chlorine concentration of 44% is calculated, which is rounded up, to 50% for simplicity. The non linear dependence of the band gap energy on the temperature is here not included, though a better estimation would be obtained in a high temperature cubic crystallographic configuration, instead of an orthorhombic (or lower one), at which the band gap energies were obtained. Further, a better analysis of the transmission edge e.g. to take into account the exciton binding energy, stokes shift etc. should be done, but for a rough estimate, this analysis is sufficient.

7.2 Hole Spin Dynamics

The nanocrystal sample is transmissive enough to avoid working in reflection geometry for the probe beam and to use a transmission configuration instead. First, the spectral response of the time resolved Faraday rotation (TRFR) and ellipticity (TRFE) is investigated. The TRFR signal, Fig. 7.2.1**a**, shown as a time resolved colour map, shows a high amplitude around 2.738 eV, with a simple beating pattern, slowly decaying in time. The Faraday Rotation amplitude and ellipticity amplitude for $t = 0$ is shown, in Fig. 7.2.1**b**, with a transmission spectrum for reference. Both, TRFE and TRFR, follow a simple Gaussian profile, with FWHM 13.2 meV. The Gaussian profile width reflects the size distribution of the nanocrystals. For 7 nm nanocrystals, a range of ± 0.3 nm can be estimated, according to the confinement energy, see Sec. 2.9.1. The curves lay slightly higher in energy than the transmission edge, but coincide perfectly with the PL spectrum (see Fig. 7.1.1). Anticipating the upcoming analysis, it is worth to note, that the observed spin beating will be attributed to the precession of hole spins.

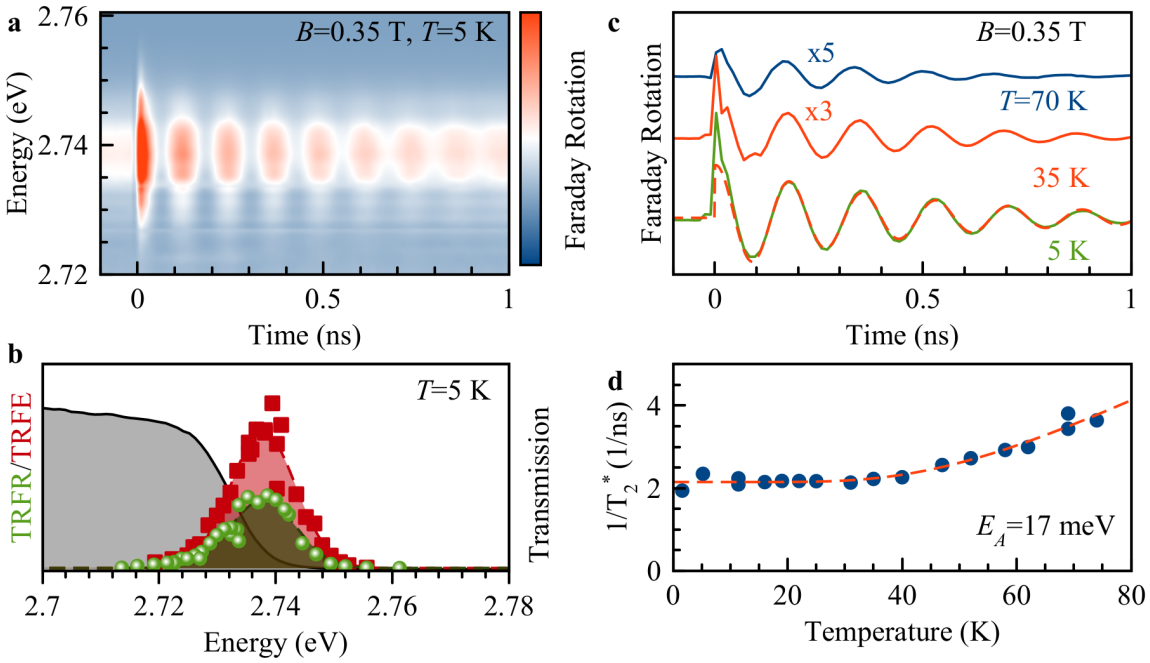

Figure 7.2.1 Hole Spin Dynamics. **a**, Spectral dependence of TRFR spectrum at $T = 5$ K and magnetic field in Voigt geometry, $B = 0.5$ T. **b**, Amplitude of Faraday rotation (ellipticity) signal, green (red) markers as a function of energy. Dashed line with filling under curve show Gaussian fits. Both peaks have maxima at 2.738 eV and widths of 7 meV. **c** Selected TRFR measurements for $T = 70, 35$ and 5 K at a Voigt magnetic field of $B = 0.35$ T, laser energy was set to 2.738 eV. Red dashed line gives fit of curve at 5 K. All curves are shifted vertically. **d**, Temperature dependence of dephasing rate at $B = 0.35$ T (dots). Arrhenius fit (dashed line) gives an activation energy $E_A = 17$ meV.

The spin dynamics is shown for increasing temperatures in Fig. 7.2.1**c**. With increasing temperature, the TRFR signal drops in amplitude, but is still well resolved up to the liquid nitrogen temperature of about 80 K. The spin dephasing, the envelope of the signal, for a huge ensemble needs to be described with a Gaussian function, $\mathrm{TRFR(E)} = A\cos(\omega_L t)\exp(-(t/T_2^*)^2)$, instead of an exponential decay. While for $T = 5$ K $T_2^* = 478$ ps, the dephasing time decreases for increasing temperatures down to a value of $T_2^* = 290$ ps at $T = 75$ K. As the spin dephasing time exceeds the decay time of the differential transmission in Fig. 7.1.1**d**, the spin dynamics are attributed to resident carriers. As will be shown in Sec. 7.3, these carriers can be identified as holes. The temperature dependence of $1/T_2^*$, Fig. 7.2.1**d**, is flat below $T < 40$ K, and shows a moderate increase for higher temperatures. The dependence can be described by an Arrhenius function, giving an activation energy $E_A = 17$ meV. Comparing the temperature dependence with bulk perovskites, one can find a significant increase from about $E_{A,\mathrm{bulk}} \approx 4$ meV to $E_{A,\mathrm{NC}} = 17$ meV [Bel19; Ode17], due to the strong carrier localization within the nanocrystals.

Tuning of the magnetic field strength, B, increases the Larmor precession frequency ω_L and shortens T_2^*, the envelope, with rising B, Fig 7.2.2**a**. The dependence of ω_L on B is linear, and without a notable offset at a zero magnetic field. With a fit of $\omega_\mathrm{L} = |g|\mu_B B/\hbar$, a hole

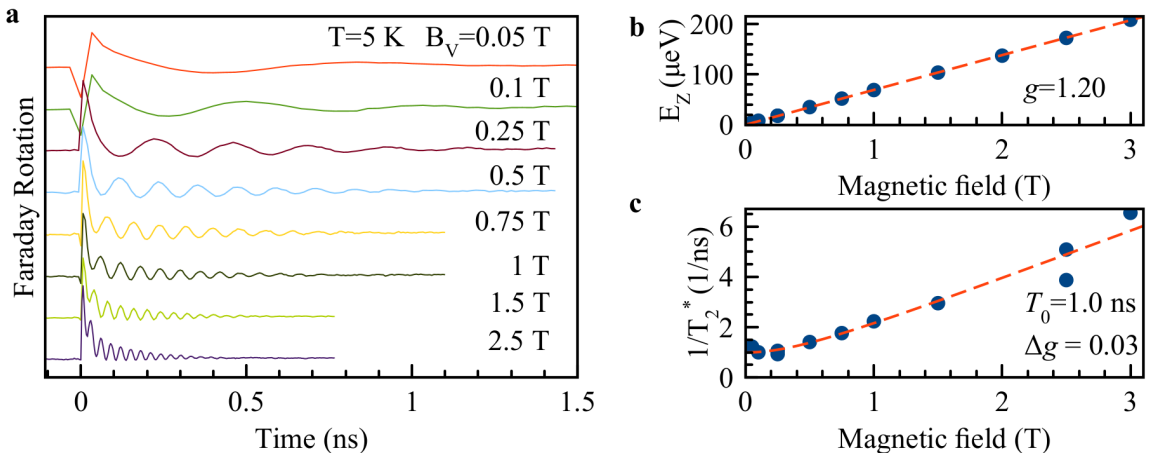

Figure 7.2.2 Magnetic field dependence. **a**, Time-resolved Faraday rotation (TRFR) signals for increasing magnetic field of 50 mT to 2.5 T, $T = 5$ K. All curves are shifted vertically. **b** Zeeman energy, taken from Larmor frequency, dependence on magnetic field (dots). Fit with linear dependence (dashed line) gives $|g| = 1.20$ at $T = 5$ K. **c**, Dephasing rate $1/T_2^*$ (dots) as a function of magnetic field with fit (dashed line). Fit parameters give $T_0 = 0.5$ ns and $\Delta g = 0.03$ at $T = 5$ K.

g-factor of +1.2 was determined for these $CsPb(Cl_xBr_{1-x})_3$ NCs. The sign of the g-factor is positive, according to **k**·**p** theory, see Fig. 6.1.1. The characteristic damping, the dephasing time T_2^*, shortens with increase of B, due an increased precession phase mismatch, caused by the spread of g-factor Δg (Fig. 7.1.1**g**). This dephasing time can be described by the equation $1/T_2^* = 1/T_{2,0}^* + \Delta g \mu_B B/\hbar$, from which a spread of g-factor $\Delta g = 0.03$ is determined. From the energy to g-factor relation, presented in Fig. 6.1.1, for the size distribution of ± 0.3 nm, one can determine a g-factor distribution of $g_{NC} = 0.008$ within the ensemble width of 13.2 meV. As, only a small selection of NC sizes is covered by the limited energy width of the exciting laser pulse, the spread of g-factor needs to originate from another source than the size distribution. A suggestion would be the g-factor anisotropy.

7.2.1 Modelocking of Spin Coherence

The TRFR signal changes dramatically, when the temperature is lowered towards $T = 1.6$ K, Fig. 7.2.3**a**. Surprisingly, before the pump pulse appearance time, for $t < 0$, a pronounced oscillation with a rising amplitude is observed. The rising signal, at negative delays $t < 0$, occurs as a result of spin modelocking, sketched in Fig. 7.2.3**b**. The signal is a sum of a huge ensemble of NCs. While the ensemble spins dephase rapidly (T_2^*), each individual NC is neither relaxed (T_1) nor has lost coherence (T_2). Hence, for nanocrystals which have a Larmor precession frequency equal to a multiple of the laser repetition frequency, i.e. the precession is in phase with the train of re-excitations, the phase synchronization condition (PSC) is fulfilled, described in detail in the theory Sec. 2.8. A train of periodic laser pulses leads to a build-up of a spin polarization for those NCs fulfilling the PSC. Taking, for instance, a spread of g-factor of $\Delta g = 0.03$, in a magnetic field of $B = 0.35$ T, precession frequencies of $\nu = (g \pm \Delta g)\mu_B B/h = 8.19 - 8.61$ GHz are present. This corresponds to $n = 107.7 - 113.3$ times the laser repetition frequency of 76 MHz, giving the main contributions of the spin

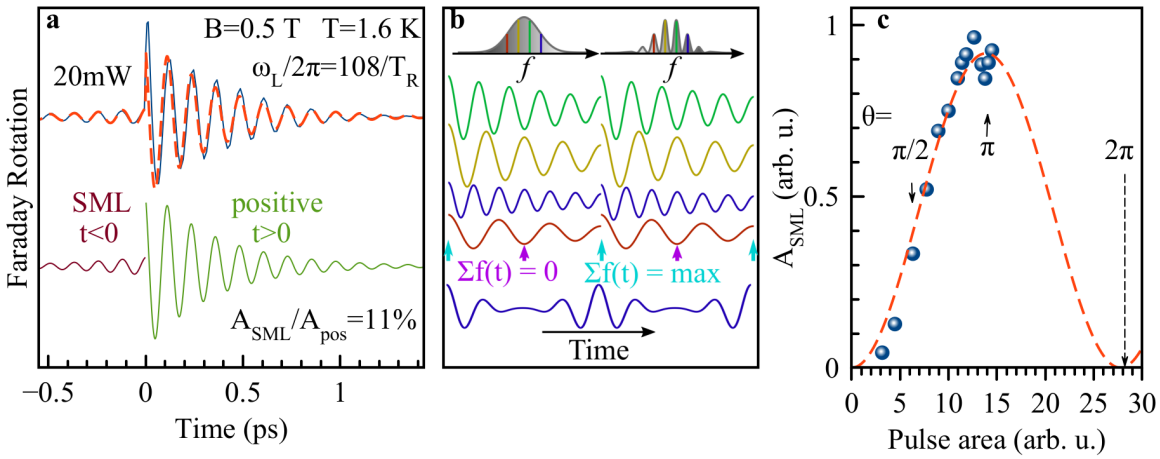

Figure 7.2.3 Spin modelocking. **a**, TRFR at low temperature $T = 1.6$ K. The signal (blue line) is composed of two oscillations. One for times $t > 0$, one for $t < 0$. The signal for $t < 0$ is the spin modelocking signal (SML). Contributions are decomposed by fit, (green and dark-red curves), both with g-factor of $+1.20$ and shifted vertically from the original curve. The SML amplitude A_{SML} and signal amplitude A_{pos} extrapolated to $t = 0$ ps, have a ratio of 11%. **b**, Schematic illustration of SML. Top, gaussian larmor frequency distribution of a nanocrystal ensemble undergoes a transition to comb like distribution due to the spin modelocking. Below, composition of SML signal (lowest curve, blue) out of exemplary four oscillating components (red, blue, yellow, green). While the oscillation is in phase for $t = nT_{\mathrm{R}}$, $n = \{0, 1, 2\}$ and T_R the laser repetition time (13.2 ns), marked by turquoise markers, the oscillation is out of phase for $n = \{0.5, 1.5\}$ (purple markers). The signal is a sum of all components $\sum f(t)$, being zero for half integer n and maximum for full integer n. **c**, Amplitude of SML extrapolated to $t < 0$ (red curve in **a**) as a function of the laser pulse area $P^{1/2}$. Dashed line is a guide for the eye, indicating Rabi oscillations.

modelocking signal.

With increasing of the excitation power (the pulse area, as time integrated energy of a single pulse, $\theta \propto \sqrt{P}$) the SML amplitude is expected to show a Rabi oscillation [Gre06a], shown in Fig. 7.2.3**c**. The two states, $|0\rangle$, as resident hole and $|1\rangle$ as full binding of said resident hole in a hole singlet state, form the eigenstates of a Bloch sphere. The spin-selective excitation with circular polarized light leads to a hole spin polarization with the SML amplitude directly dependent on the pulse area. The maximum therein correspond to a pulse area $\theta = \pi$, while the minima correspond to 2π [Gre06a].

In combination with the information of the spin ensemble distribution (Δg) and the excitation efficiency (θ), the coherence time T_2 can be estimated by a theoretical modelling of the signal [Fra12; Yug09]. The details of this methods will be presented in a more theoretical elaborated publication. Still, it can be stated, that the best agreement was found for times $T_2 \approx 10 - 30$ ns.

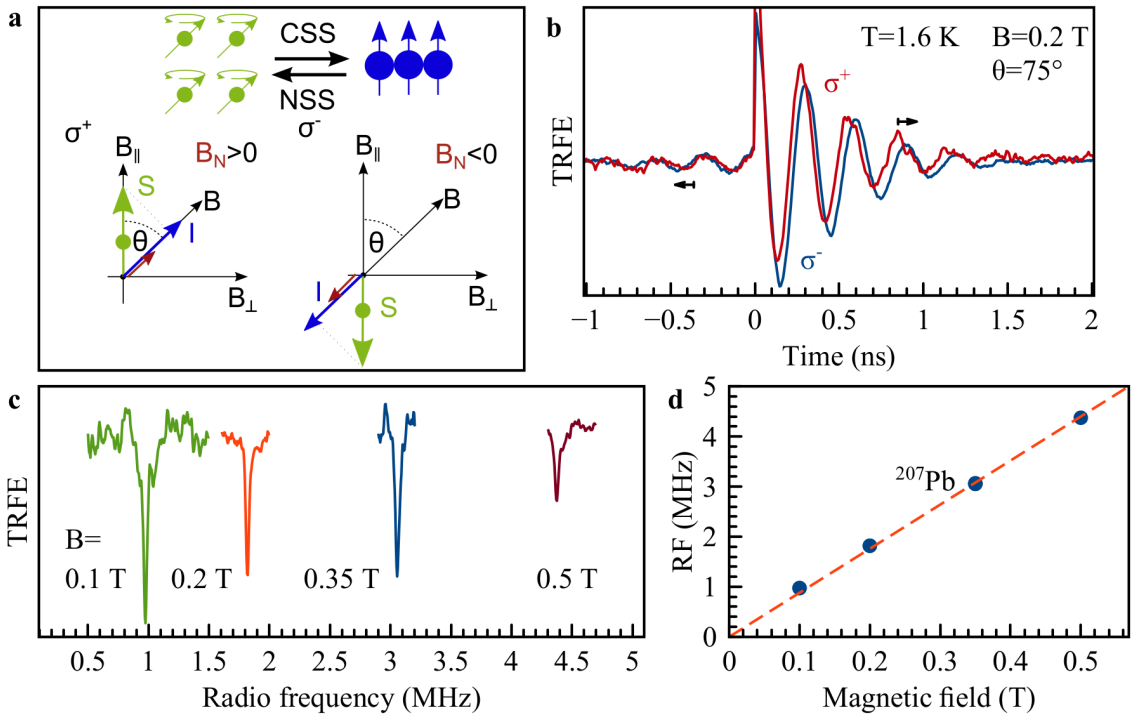

Figure 7.3.1 Optically detected nuclear magnetic resonance (ODNMR). a, The DNP scheme for carriers with positive g-factor sign. Repeated for convenience from Sec. 2.4, Fig. 2.4.1 and Fig. 5.2.6. **b**, Time-resolved Faraday ellipticity signals for σ^+ (red) and σ^- (blue) excitation polarization shows a difference in precession frequency due to presence of a DNP. **c**, ODNMR signals in various magnetic fields. On signal as in (**b**) for labelled magnetic fields and σ^+ excitation on a fixed time delay, a frequency-swept RF signal was applied. The time delay was set in accordance to a given precession frequency, to be at the maximum amplitude difference between σ^+ to σ^- signal, e.g. 490 ns at $B = 0.2$ T. **d**, Magnetic field dependence of the ODNMR resonance frequency (dots), red line is linear fit. Dependence matches gyromagnetic ratio γ of ^{207}Pb= 8.8 MHz/T.

7.3 Hole Spin – Nuclear Spin Interaction

The investigation of the carrier spin nuclear interaction can provide an insight into the identification of the type of carrier spin, g-factor sign and the cause of the spin dephasing. In a first step, the scheme of dynamic nuclear polarization (DNP), as discussed in the theory Sec. 2.4, was applied, see Fig. 7.3.1**a**. In a small magnetic field of $B = 0.2$ T, under an angle of $\theta = 75°$, at a low temperature of $T = 1.6$ K and under a constant helicity excitation, a dynamic nuclear polarization was observed, Fig. 7.3.1**b**. For positive time delays and σ^+ excitation, the Larmor spin precession frequency is increased, while for σ^- it is decreased. Also for negative time delays, a difference in the Larmor frequency can be obtained, and the phase between the oscillations points in a reversed direction (indicated by arrows in the figure). The shift of the Larmor frequency is driven by the Overhauser field B_N build up, caused by the DNP. For the evaluation of B_N, only the positive time delay is taken into account. The difference of $\nu_{\sigma^+} = 3.53$ GHz to $\nu_{\sigma^-} = 3.34$ GHz corresponds to a $B_N = (\nu_{\sigma^+} - \nu_{\sigma^-})h/(2g\mu_B) = 5.7$ mT. Interestingly, in respect to the upcoming observation of nuclear induced frequency focussing

(NIFF), the Overhauser field exceeds slightly the mode separation for a spin with $g = 1.2$, $\Delta B_{\mathrm{RSA}} = 4.5$ mT and the measured frequencies of 3.34 GHz and 3.53 GHz are neither multiples of the laser repetition frequency. The NIFF and DNP apply independent of each other.

The origin of the DNP can be investigated by the application of a radio frequency field, the optically-detected nuclear magnetic resonance (ODNMR), Fig. 7.3.1**c**. The nuclear spin polarization can be reduced and even erased by the RF field, heating the NSS, of the Overhauser field driving nuclear isotope, when the RF frequency coincides with the Larmor frequency. This nuclear magnetic resonance (NMR), can be optically detected via a change of the Larmor frequency of the carriers interacting with the nuclear. In the experiment, it is useful to detect the TRFE signal amplitude at a fixed time delay. In a configuration as shown in Fig. 7.3.1**b**, the time delays were chosen in a way, that the NMR appears as minimum, but would be in general of arbitrary shape (folding of Lorentzian shaped NMR with the sinusoidal spin signal). From a magnetic field of 0.1 to 0.5 T, ODNMR resonances are observed as pronounced signal dips, Fig. 7.3.1**c**. The ODNMR resonances shift to higher frequencies with the magnetic field, remain of a similar width (≈ 30 kHz FWHM, $T^*_{2,\mathrm{N}} = 1/(\pi\Gamma_{\mathrm{N}}) = 10.6$ μs), but decrease slightly in amplitude. The ODNMR resonance frequency shifts linear, Fig. 7.3.1**d**, and follows the Zeeman splitting of ^{207}Pb with a gyromagnetic ratio $\gamma = 8.80$ MHz/T. This gyromagnetic ratio shows a chemical shift of 11000 ppm to the vacuum value [Wra90]. Note, a shift due to the Knight field should appear as frequency offset at zero magnetic fields rather than a difference in the gyromagnetic ratio (slope). Similar to the bulk hybrid organic inorganic perovskite samples, the identification of the nuclear spin, as being ^{207}Pb, allows to assign the resident carrier spin as hole spin, see also Sec. 4.4 [Kir21b]. Further, this carrier identification is in line with the observation of holes in $CsPbBr_3$ nanocrystals with a g-factor of 0.86 by Crane et. al. [Cra20]. The identification for the nanocrystals by Crane et al. is mainly driven by the g-factor value, being close to the hole g-factor value observed in bulk $CsPbBr_3$ $g_h = 0.74$, and the contrast to the electron g-factor $g_e = 1.96$ [Bel19]. See also Fig. 6.1.1 in Ch. 6.

7.3.1 Nuclear Induced Frequency Focusing

Turning back to the spin modelocking, an additional experiment was performed to test the spin modelocking mechanism, and further to identify the role of nuclei in this process. An unambiguous proof of the spin modelocking is to study the phase synchronisation condition. The previously shown regime of PSC can be extended, by applying an additional excitation pulse in between the 13.2 ns pulse interval. In Fig. 7.3.2**a**, an experiment is shown where the pump beam was, after passing of the mechanical delay line, separated by a beam splitter into two beams. While the first pump beam was not changed in its beam path, the second beam was passed via an additional delay line, giving 1/10 of T_R delay 1.3 ns, before reuniting with the beam path of the first pump. By blocking either the first or the second beam, a regular SML signal is observed and the phase synchronisation condition is not changed. Letting both pump beams pass, the pulse separation splits to a separation of 1/10 T_R and 9/10. Only the first condition is of importance here. As last curve, in Fig. 7.3.2**a**, and magnified in Fig. 7.3.2**b**, at times multiple to $1/10T_R$, the signal recovers as oscillation with bell shaped envelope. It is important to emphasize that these bursts are purely driven by the

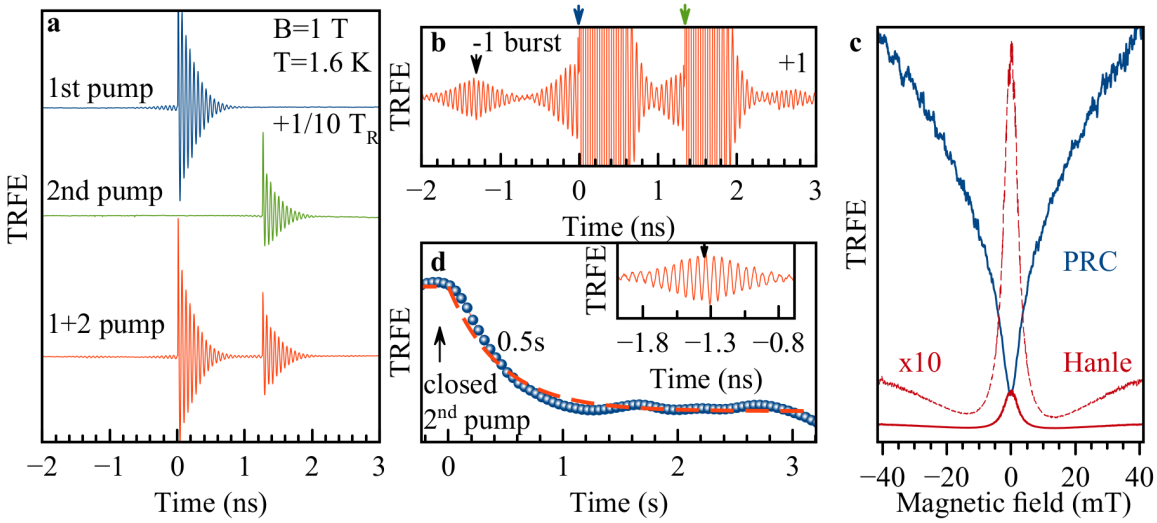

Figure 7.3.2 Spin modelocking with nuclear frequency focussing. **a**, Development of two pulse excitation scheme. Blue curve corresponds to TRFE dynamics with 1^{st} pump only, green with 2^{nd} only, red with combined 1^{st} and 2^{nd}. Excitation powers for the first and second pumps are 25 mW and 13 mW, respectively. **b**, TRFE signal with 1^{st}+2^{nd} pumps, at $t_{1^{st}} = 0$ and $t_{2^{nd}} = +1.3$ ns, in zoomed y-scale. Two additional bursts appear, labelled "−1", "+1" at $t = -1.3$ ns and $t = 2.6$ ns, respectively. **c**, PRC (blue) and Hanle (red) curve at the probe delay $t = -10$ ps. For PRC, the magnetic field points along light propagation direction, while for the Hanle measurement, the magnetic field is perpendicular. Ten times magnified Hanle curve is given by dashed line. Excitation power is 20 mW. **d**, Dynamics of burst amplitude (signal as in **a-b**) (the time delay is indicated in the inset) decay after closing the 2^{nd} pump with a fast shutter. The exponential fit gives $\tau = 0.5$ s.

changed phase synchronisation condition and no influence of any reflected, or in another way parasitically added pump pulse, could be origin of these bursts. The burst appears from the constructive superposition of spin oscillations according to a pattern with 1.3 ns separated pulses. Interestingly, the burst in a positive time delay (+1) and the one in a negative time delay (-1) differ slightly in shape and amplitude. The negative one is much clearer and stronger in shape, than the one in the positive delay, giving rise of the assumption, that another nanoseconds long living influence is present for positive time delays but disappears up to the negative time delay.

To recall the possibility of a hole spin Larmor frequency tuning by nuclear spins, Sec. 7.3, a nuclear influence on the spin modelocking might be expected. The nuclear spin influence may manifest in terms of the nuclear induced frequency focusing (NIFF). As each NC exhibits a non zero nuclear spin surrounding, the respective Overhauser field B_N could tune the hole spin frequency in such a way, that it matches the phase synchronisation condition. The nuclear induced frequency focusing can be described as a positive feedback loop [Mar19]. If a nanocrystal carrier spin is detuned from the phase synchronisation condition in such a way, that an additive B_N would be needed to fulfil it, a slight increase of B_N leads to a partial fulfilment and an increase of the carrier spin polarization. With increasing of the carrier spin polarization, the nuclear polarization rises and the nanocrystal is even further tuned to fulfil the phase synchronization condition, and so on. Finally, if the phase synchronization

condition is matched, a further build up of B_N would decrease the carrier spin polarization. Thus, blocking a further increase of B_N. It is worth to note that this effect works also for nanocrystals, for which a smaller negative B_N than a positive B_N would fulfil the PSC, as it is arbitrary to either increase or decrease the Larmor frequency to fulfil the PSC. The mode separation, corresponding to a field of $B_{\mathrm{RSA}} = 4.5$ mT, can be even exceeded by the Overhauser field, as shown in Sec. 7.3.

Still, one needs to be aware of the differences in the mechanisms of NIFF and DNP in an external field parallel to the optical axis. In the parallel DNP, the nuclear polarization is proportional to the scalar product of spin polarization and magnetic field ($\mathbf{B} \cdot \mathbf{S}$), which equals to zero in the NIFF regime, hence a non zero spin projection along the magnetic field is needed. This can exist due to a misalignment of the sample plane in respect to the magnetic field [Mar19] or if to consider the optical Stark effect induced by the pump pulse [Car09]. The optical Stark effect becomes important, if to consider that a carrier spin, which is not fulfilling the PSC, is excited during its precession in the z-y plane. Due to the optical Stark effect the exciting pulse can be than considered as an effective magnetic field applied along the z direction, which rotates the non zero y component of the spin along the x-y direction. Thus leading to a projection of the carrier spin along the external magnetic field direction, $\mathbf{B} \cdot \mathbf{S} \neq 0$.

The presence of a NIFF can be proven with an observation of the time dynamics of the burst disappearance, if to change from two pulse to single pulse regime. In Fig. 7.3.2**d**, a time delay equal to -1 burst maximum is fixed, and the signal amplitude recorded, before and after closing of the 2$^{\mathrm{nd}}$ pump beam. After the closing, a single exponential decay is seen with a fitted time constant of 0.5 s. This time exceeds the carrier spin longitudinal relaxation time T_1 (presented in upcoming Sec. 7.4) and is comparable to a typical nuclear relaxation time $T_{1,N} = 5.5$ s [Kir21b]. To elaborate, at the time of the closing of the 2$^{\mathrm{nd}}$ pump, still, an Overhauser field was imprinted into the nanocrystals, for the fulfilment of the 1/10 T_R PSC, prevailing the burst amplitude for 0.5 s. Further, the presence of a NIFF assisted spin modelocking is in line with the observation of an enhanced spin modelocking amplitude in low temperatures, as typically in low temperatures a higher nuclear polarization can be observed, see also Fig. 4.3.2.

Last, a measure of the nuclear spin fluctuations shall be obtained. In Fig. 7.3.2**c**, a regular single pulse polarization recovery curve and a resonant spin amplifiaction experiment is shown, see Sec. 2.5 (PRC) and 2.7 (RSA). At a fixed time delay of $t = -10$ ps as a function of a weak magnetic field in Faraday geometry, the PRC is observed. The PRC shows two superimposed Lorentzian peaks, with FWHM of 88.4 mT and 10.4 mT, representing the spread of the nuclear fluctuation field. The appearance of an RSA peak comb, separation $B_{\mathrm{RSA}} = 4.5$ mT, in Voigt geometry in dependence of the magnetic field is suppressed, due to the presence of the spin modelocking. Instead, two super imposed Lorentzian curves (Hanle curves) are observed. One with a FWHM of 5.4 mT and another with 53.2 mT.

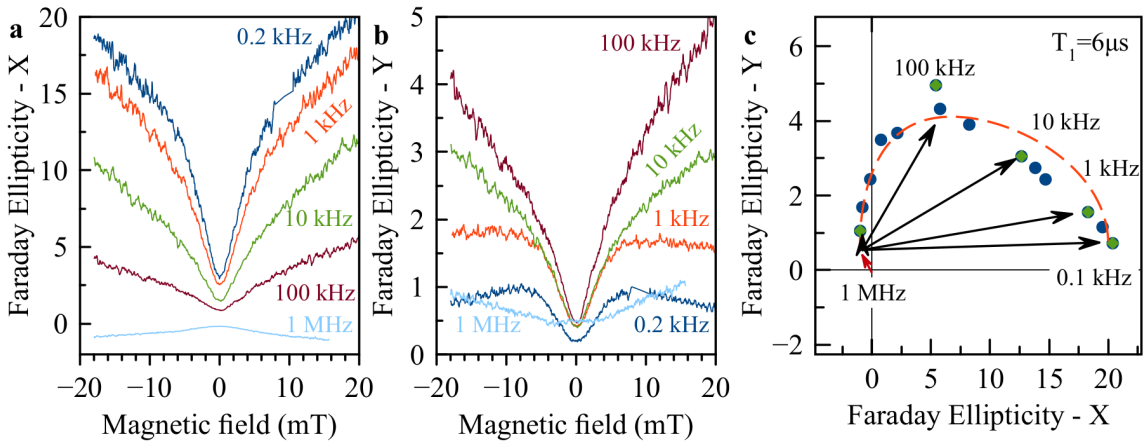

Figure 7.4.1 Spin Inertia. **a**–**b**, PRC curves for various modulation frequencies, as recorded by Lock-In - X (Y)-channel **a**(**b**). The Lock-In phase of the reference signal was set to 0° and kept constant for all curves. **c**, X versus Y-channel of amplitudes for $B = -20$ mT. Black arrows indicate vectors for specific frequencies and red arrow gives an estimate of the negative offset. $T = 1.6$ K for all panels. A theoretical spin inertia curve gives a best fitting with $T_1 = 6$ μs

7.4 T_1 Measured by Spin Inertia

To complete the set of spin dynamics characteristics, the longitudinal relaxation time T_1 was determined. T_1 can be measured using the spin inertia technique, see Sec. 2.6 [Hei15; Smi18]. In Fig. 7.4.1**a**, a set of PRC curves for increasing pump modulation frequencies f_{mod} are shown. With an increase of f_{mod}, the amplitude drops, in accordance with the theory. Further, the PRC curves become broader, which might be a sign of decreasing nuclear fluctuations in a low frequency modulation, but is not analysed in detail. Interestingly, the amplitude turns even into a negative amplitude for high frequencies as 1 MHz. This effect can be explained, if one takes into account the specifics of the signal detection by the Lock-In technique. In the spin inertia technique, not only the amplitude drops, but also the spin polarization is delayed in respect to the exciting pulse sequence [Mik18]. Thus, in the Lock-In, a phase difference between the detected and the reference signal appears. In the Lock-In technique, the detected probe signal is multiplied with the reference frequency $S = FE\exp(i\omega t + \varphi) \times \exp(-i\omega t)$, where the oscillating terms cancel. If the phase is zero, the signal gets fully projected to the (real part) X-channel of the Lock-In. However, with appearing of a phase, the signal starts to be also partly projected into the (imaginary part) Y-channel. In a typical measurement, thus, the phase is all the time adjusted in accordance to the used modulation frequency, in a way that all the signal is projected into the X-channel. In this case the Y-channel is typical ignored. Here, the phase set in the Lock-In was kept constant on the value adjusted for a slow modulation frequency (0.2 kHz) and both channels, X and Y, analysed, shown in Fig. 7.4.1**a-b**. The Y-channel signal shape matches the X-channel signal of two superimposed Lorentzians and increases in amplitude with the rise of the modulation frequency. For a full analysis, both the X and Y channel signals are plotted against each other in a Lissajous-like way, with the respective values for $B = 20$ mT. In this way both, the amplitude drop and the phase change, can be seen clearly by the deviation of the observed egg like shape, from a point type (no spin

inertia effect) or line (amplitude drop without phase change). The vector length towards each point gives the real signal amplitude. In fact, it is experimentally unavoidable to have a small amount of a parasitic signal, being independent from the modulation frequency, for instance, from a small amount of scattered light adding to the signal. Thus, at some point of the phase rotation, the sum of spin signal plus offset, crosses the zero line. This reflects the observed sign change of the 1 MHz PRC curve, in Fig. 7.4.1**a**. In combination of, the amplitude drop, phase rotation, and the offset, the signal can be simulated and a longitudinal relaxation time of $T_1 = 6$ μs extracted (red dashed curve in Fig. 7.4.1**c**).

7.5 Summary/Discussion

The all inorganic lead halide nanocrystals embedded in a fluorophasphate glass matrix turned out to show a very clear spin response. Interestingly, in this nanocrystals only one carrier type, the hole spin, is observed. Also, the spectral shape of the Faraday amplitude shows only a single, Gaussian-type, resonance in contrast to the typically dispersive resonances observed in bulk crystals, assuming a dominant trion type spin excitation mechanism in contrast to the superimposed exciton-trion like excitation mechanisms found for bulk structures.

With a spin dephasing time T_2^* about one nanosecond at small magnetic fields, the hole spin ensemble shows a comparable, but smaller, dephasing time as carrier spins in all inorganic lead halide perovskite $CsPbBr_3$ [Bel19]. The accelerated dephasing in elevated Voigt magnetic fields does not drastically differ, here a spread of g-factor of 0.03 was obtained, while in bulk $CsPbBr_3$ single crystals $\Delta g = 0.05$ was measured.

The most drastic difference occur in different aspects. In nanocrystals, an enhanced carrier spin lifetime T_1 up to microseconds, an increased activation energy, an increased nuclear spin interaction, and the effect of spin modelocking, was observed. All these are assumed to originate from the increased carrier localization in nanocrystals.

To conclude, the all inorganic nanocrystals embedded in a glass matrix are very promising for application. Undemanding synthesis and a good protection against environmental factors come together with a spin dynamic prevailing above the temperature of liquid nitrogen. Even the unavoidable drawback of an inhomogeneous nanocrystal system seems to be solvable, as with the observed spin modelocking effect, the ensemble can be driven to a collective mode.

8

Summary and Outlook

Summary. In this thesis, the carrier spin dynamics in several lead halide crystals were studied. Explicitly, the hybrid organic, single crystals $MAPbI_3$ and $FA_{0.9}Cs_{0.1}PbBr_{0.2}I_{2.8}$ single crystals and the all inorganic, $CsPb(Cl_xBr_{(1-x)})_3$, nanocrystals were treated in detail. The main focus were studies using the large toolbox of the time resolved pump probe technique established in conventional semiconductors. In all crystals, pronounced resident carrier spin signals were obtained and, apart from the nanocrystal case, both electron and hole spin simultaneously. The resident carriers showed a nanosecond long spin precession, which allowed to determine precisely their g-factor and the g-factor anisotropy. Further, the change of T_2^* with tuning of external parameters like the bath temperature and the magnetic field, proofed a small thermal activation energy, leading to delocalization, and a spread of g-factor of a magnitude common for resident carriers. The differences in the Kerr amplitude between electron and hole spin further showed an independence of both carriers. They are not equally populated, thus not bound in an exciton or a photogenerated electron hole pair.

In comparison of the spin signals with the reflectivity and photoluminescence measurements, those evaluations were further strengthened. For both single crystals, the exciton lifetimes were determined to fall into the range of ≈ 300 ps, well below the observed spin relaxation times of the carriers. Also, the exciton g-factors, for $MAPbI_3$ treated explicit and for $FAPbI_3$ taken from literature [Miy15], both being $g \approx 2.3$, matches well the combined g-factor of the resident carriers, which reflects a proper determination of the g-factor values and signs.

The experimental observations together with a theoretical estimate, lead to a comprehensive picture of carrier g-factors in hybrid organic and all inorganic lead halide perovskites. An universal law of the g-factor upon the band gap energy was formulated. Within this model, the g-factor trend was well reproduced and the g-factor anisotropies turned out to be individual for each crystal, leading to small deviations from the predicted uniaxial dependence.

Studying the carrier-nuclear spin interaction revealed as a versatile tool. As the hole spins showed a much stronger nuclear interactions than electron spins, a clear identification could be provided. Further, in the present, iodine based, single crystal cases, the build up of a dynamic nuclear polarization, giving rise to a strong Overhauser field, was observed. The Overhauser field pointed in different directions for electron and hole spins, which confirmed the assumption, from the exciton g-factor, of a negative g-factor sign of holes. From all nuclear

isotopes the dominant role of lead ^{207}Pb hyperfine interaction was identified, by an optically detected nuclear magnetic resonance measurement.

A promising approach to improve the chemical stability of the perovskite crystals is to embed them in a protective surrounding. Here, the approach of a glassy surrounding was chosen. Stable, nanometer sized, all inorganic $CsPb(Cl_xBr_{(1-x)})_3$ nanocrystals form, which results in strongly confined and therefore localized carriers. In the nanocrystals, the electron spin signal vanished, while a clear hole spin signal remained. The spin dynamics of the hole spins showed a significant higher thermal activation energy, giving rise to a remaining signal above liquid nitrogen temperature. Inevitably, the nanocrystal spin ensemble is inhomogeneous, leading to a shorter ensemble dephasing time, as compared to the bulk case. The higher inhomogeneity and so the presence of a distribution of Larmor frequencies, covering multiples of the laser repetition rate, lead in turn to the presence of spin modelocking, a revival of the spin coherence long after the dephasing time T_2^*. With the use of the spin modelocking, the observable resident hole spin polarization of the nanocrystal ensemble is not longer limited by T_2^* but rather by T_2. The presence of the spin modelocking effect was proven and a spin control was demonstrated by a two pulse protocol, giving rise to characteristic spin revival bursts, well separated from the excitation pulses.

The hole spins in those nanocrystals showed a strong hyperfine interaction. A dynamic nuclear polarization was achieved, and the interaction with ^{207}Pb spin revealed by an optically detected nuclear magnetic resonance. The prior demonstrated spin revival bursts, in the spin mode locking, were used to reveal the presence of nuclear induced frequency focussing.

Overall, the well-established physical description and observation of the charge carrier and nuclear spin dynamics of III-V and II-VI semiconductors was successfully extended to the inorganic and hybrid organic inorganic lead halide perovskites.

Outlook. For the future, the presented studies motivate for several new perspectives. First of all, so far no limits of the chemical composition were found. Both all inorganic as well as hybrid organic inorganic lead halide perovskites showed pronounced carrier spin signals. Numerous substitutions within the ABX_3 structure are conceivable.

The A-cation divides the class of lead halides into the hybrid organic inorganic and all inorganic class. As the quantum efficiency for the hybrid organic inorganic class is typically higher than for the all inorganic class, a perspective would be to study several A cations.

In particular, in a remarkable study of a broad variety of material compositions, Ref. [Zha21b], a chemical composition close to $FA_{0.9}Cs_{0.1}PbI_{2.8}Br_{0.2}$, namely $MA_{0.1}Cs_{0.05}FA_{0.85}PbI_{2.85}Br_{0.15}$, showed a promising durability (device lifetime >1200 h) and performance (19.5% quantum efficiency), motivating a gradual admixture of MA, FA and Cs. In this study, further, the alkali metal caesium was substituted successfully by potassium. Such a substitution may also help to identify the role of caesium.

Another approach is to vary the organic A-cation. For instance, the next candidate of the nitrogen series MA (CH_3NH_3) and FA ($CH(NH_2)_2$) is guanidine (GA, $HNC(NH_2)_2$). Though, as for its molecular size, the respective tolerance factor of a guanidine lead halide crystal rapidly exceeds one, a certain pathway would be to use an admixture to $MA_{1-x}GA_xPbI_3$ crystals [Zha20a].

In particular, recently, the role of hydrogen was pointed out to influence the perovskite

performance in a solar cell application [Zha21a]. A promising way to study the role of the hydrogen surrounding would be a replacement with deuterium [Har18; Var19]. Instead of a spin $I_{\mathrm{H}} = 1/2$, the heavier deuterium has a spin $I_{\mathrm{D}} = 1$, which should result in a change of the interaction with the carrier spins, e.g. broadening of PRC curve etc.

An engineering of the nuclear spin environment would be also interesting in respect to a nuclear purification of the lead isotopes. It is possible to either enrich the amount of ^{207}Pb to 100% abundance or to purify it to 0%. The latter case might be the more interesting one. While both, enrichment and purification may lead to a better understanding of the electron spin hyperfine interaction, in the latter case, the erased background of lead spins, may facilitate to reveal the presence of a halogen spin interaction with both carrier spins, which is difficult in other approaches [Fu20].

On the *B*-cation side, it is frequently discussed to replace lead by the non toxic tin. Tin based perovskite solar cells reach an efficiency of about 13% [Nis20]. Again, studies of the carrier spin dynamics might help to improve the physical description of such systems.

Besides the chemical composition, a promising perspective is the nanostructuring of perovskite crystals. In this case, the confinement and surface effects should be studied by variation of the nanocrystal size and form. The chances of doping the crystals should be explored. It would be beneficial to study both, electron and hole spins. A doping might also extend the field of studies towards the area of diluted magnetic semiconductors, by the introduction of manganese, or localized surface plasmons, by the introduction of silver particles [Che21].

Lastly, two dimensional perovskite layers (2D Ruddlesden-Popper), may give rise to interesting physical phenomena, like a strong Rashba-Dresselhaus effect [Pha22].

List of Figures

Bibliography

[Abr94] A. Abragam. *The Principles of Nuclear Magnetism*. Oxford: University Press, 1994.

[Aeb20] M. Aebli, L. Piveteau, O. Nazarenko, B. M. Benin, F. Krieg, R. Verel, and M. V. Kovalenko. "Lead-Halide Scalar Couplings in ^{207}Pb NMR of $APbX_3$ Perovskites (A = Cs, Methylammonium, Formamidinium; X = Cl, Br, I)". In: *Scientific Reports* 10.1 (2020), p. 8229. DOI: 10.1038/s41598-020-65071-4.

[Ala21] A. Alaei, A. Circelli, Y. Yuan, Y. Yang, and S. S. Lee. "Polymorphism in metal halide perovskites". In: *Materials Advances* 2.1 (2021), pp. 47–63. DOI: 10.1039/D0MA00643B.

[Ale01] K. S. Aleksandrov and J. Bartolomé. "Structural distortions in families of perovskite-like crystals". In: *Phase Transitions* 74.3 (2001), pp. 255–335. DOI: 10.1080/01411590108228754.

[Ale76] K. S. Aleksandrov. "The sequences of structural phase transitions in perovskites". In: *Ferroelectrics* 14.1 (1976), pp. 801–805. DOI: 10.1080/00150197608237799.

[Ary21] P. Aryal, H. Kim, S. Saha, J. Cho, A. V. Ntarisa, S. Kothan, and J. Kaewkhao. "Rapid and convenient crystallization of quantum dot $CsPbBr_3$ inside a phosphate glass matrix". In: *Journal of Alloys and Compounds* 866 (2021), p. 158974. DOI: 10.1016/j.jallcom.2021.158974.

[Ash76] N. W. Ashcroft and N. D. Mermin. *Solid state physics*. eng. New York [u.a.]: Holt, Rinehart and Winston, 1976.

[Att15] J. P. Attfield, P. Lightfoot, and R. E. Morris. "Perovskites". In: *Dalton Transactions* 44.23 (2015), pp. 10541–10542. DOI: 10.1039/C5DT90083B.

[Aws08] D. D. Awschalom, T. Dietl, M. Kaminska, and H. Ohno. *Spintronics, Volume 82 - 1st Edition*. Vol. 82. Semiconductors and Semimetals. Academic Press, 2008.

[Bö18] K. W. Böer and U. W. Pohl. *Semiconductor Physics*. Ed. by K. W. Böer and U. W. Pohl. Cham: Springer International Publishing, 2018. DOI: 10.1007/978-3-319-69150-3_1.

[Bar20] M. Baranowski and P. Plochocka. "Excitons in Metal-Halide Perovskites". In: *Advanced Energy Materials* 10.26 (2020), p. 1903659. doi: https://doi.org/10.1002/aenm.201903659.

[Bay02] M. Bayer, G. Ortner, O. Stern, et al. "Fine structure of neutral and charged excitons in self-assembled In(Ga)As/(Al)GaAs quantum dots". In: *Physical Review B* 65.19 (2002), p. 195315. doi: 10.1103/PhysRevB.65.195315.

[Bed88] J. G. Bednorz and K. A. Müller. "Perovskite-type oxides–The new approach to high-T_c superconductivity". In: *Reviews of Modern Physics* 60.3 (1988), pp. 585–600. doi: 10.1103/RevModPhys.60.585.

[Bel16] V. V. Belykh, E. Evers, D. R. Yakovlev, F. Fobbe, A. Greilich, and M. Bayer. "Extended pump-probe Faraday rotation spectroscopy of the submicrosecond electron spin dynamics in n-type GaAs". In: *Phys. Rev. B* 24 (2016), p. 241202.

[Bel19] V. V. Belykh, D. R. Yakovlev, M. M. Glazov, et al. "Coherent spin dynamics of electrons and holes in $CsPbBr_3$ perovskite crystals". In: *Nature Communications* 10.1 (2019), p. 673. doi: 10.1038/s41467-019-08625-z.

[Bes05] B. Beschoten. "Spin coherence in semiconductors". In: *Magnetism goes Nano*. Ed. by S. Blügel, T. Brückel, and C. M. Scheider. Vol. 26. Forschungszentrum Jülich, 2005. Chap. E7.

[Bla18] J.-C. Blancon, A. V. Stier, H. Tsai, et al. "Scaling law for excitons in 2D perovskite quantum wells". In: *Nature Communications* 9.1 (2018), p. 2254. doi: 10.1038/s41467-018-04659-x.

[BR16] S. Boyer-Richard, C. Katan, B. Traoré, R. Scholz, J.-M. Jancu, and J. Even. "Symmetry-Based Tight Binding Modeling of Halide Perovskite Semiconductors". In: *J. Phys. Chem. Lett.* 7.19 (2016), pp. 3833–3840. doi: 10.1021/acs.jpclett.6b01749.

[Bra17] R. E. Brandt, J. R. Poindexter, P. Gorai, et al. "Searching for "Defect-Tolerant" Photovoltaic Materials: Combined Theoretical and Experimental Screening". In: *Chemistry of Materials* 29.11 (2017), pp. 4667–4674. doi: 10.1021/acs.chemmater.6b05496.

[Bug86] M. Bugajski, W. Kuszko, and K. Regiński. "Diamagnetic shift of exciton energy levels in GaAs-$Ga_{1-x}Al_xAs$ quantum wells". In: *Solid State Communications* 60.8 (1986), pp. 669–673. doi: 10.1016/0038-1098(86)90265-6.

[Car09] S. G. Carter, A. Shabaev, S. E. Economou, T. A. Kennedy, A. S. Bracker, and T. L. Reinecke. "Directing Nuclear Spin Flips in InAs Quantum Dots Using Detuned Optical Pulse Trains". In: *Physical Review Letters* 102.16 (2009), p. 167403. doi: 10.1103/PhysRevLett.102.167403.

[Che21] Y. Chen, Y. Zhang, L. Bao, W. Liu, and Y. Zhang. "Plasmon-Enhanced Blue Photoluminescence Efficiency from $CsPb(Br/Cl)_3$ Perovskite Nanocrystals by Silver Nanoparticles". In: *The Journal of Physical Chemistry C* 125.19 (2021), pp. 10631–10638. doi: 10.1021/acs.jpcc.1c01136.

[Cra20] M. J. Crane, L. M. Jacoby, T. A. Cohen, Y. Huang, C. K. Luscombe, and D. R. Gamelin. "Coherent Spin Precession and Lifetime-Limited Spin Dephasing in $CsPbBr_3$ Perovskite Nanocrystals". In: *Nano Letters* 20.12 (2020), pp. 8626–8633. doi: 10.1021/acs.nanolett.0c03329.

[Dan14] Y. Dang, Y. Liu, Y. Sun, et al. "Bulk crystal growth of hybrid perovskite material $CH_3NH_3PbI_3$". en. In: *CrystEngComm* 17.3 (2014), pp. 665–670. doi: 10.1039/C4CE02106A.

[Dar14] C. Darwin. "LXXVIII. The theory of X-ray reflexion. Part II". In: *The London, Edinburgh, and Dublin Philosophical Magazine and Journal of Science* 27.160 (1914), pp. 675–690. doi: 10.1080/14786440408635139.

[Den06] Denninger. "Graduate College 448 "Magnetic Resonance", Introduction to ESR". Lecture Script. Stuttgart, Germany, 2006.

[Din16] J. Ding, H. Fang, Z. Lian, J. Li, Q. Lv, L. Wang, J.-L. Sun, and Q. Yan. "A self-powered photodetector based on a $CH_3NH_3PbI_3$ single crystal with asymmetric electrodes". en. In: *CrystEngComm* 18.23 (2016), pp. 4405–4411. doi: 10.1039/C5CE02531A.

[Din17] J. Ding, S. Du, Y. Zhao, et al. "High-quality inorganic–organic perovskite $CH_3NH_3PbI_3$ single crystals for photo-detector applications". In: *Journal of Materials Science* 52.1 (2017), pp. 276–284. doi: 10.1007/s10853-016-0329-2.

[Din18] J. Ding, L. Jing, X. Cheng, Y. Zhao, S. Du, X. Zhan, and H. Cui. "Design Growth of $MAPbI_3$ Single Crystal with (220) Facets Exposed and Its Superior Optoelectronic Properties". In: *The Journal of Physical Chemistry Letters* 9.1 (2018), pp. 216–221. doi: 10.1021/acs.jpclett.7b03020.

[Dir16] D. N. Dirin, I. Cherniukh, S. Yakunin, Y. Shynkarenko, and M. V. Kovalenko. "Solution-Grown $CsPbBr_3$ Perovskite Single Crystals for Photon Detection". In: *Chemistry of Materials* 28.23 (2016), pp. 8470–8474. doi: 10.1021/acs.chemmater.6b04298.

[Don18] Y. Dong, T. Qiao, D. Kim, D. Parobek, D. Rossi, and D. H. Son. "Precise Control of Quantum Confinement in Cesium Lead Halide Perovskite Quantum Dots via Thermodynamic Equilibrium". In: *Nano Letters* 18.6 (2018), pp. 3716–3722. doi: 10.1021/acs.nanolett.8b00861.

[Dra83] T. Drakenberg and S. Forsén. "The halogens–chlorine, bromine, and iodine". In: *The Multinuclear Approach to NMR Spectroscopy*. Ed. by Lambert, J. B., and F. G. Riddell. the Netherlands NATO ASI Series: Springer, 1983, pp. 405–444.

[Dya08] M. I. Dyakonov. *Spin Physics in Semiconductors*. en. Ed. by M. I. Dyakonov. Springer Series in Solid-State Sciences. Berlin, Heidelberg: Springer, 2008. doi: 10.1007/978-3-540-78820-1_1.

[Dya72] M. I. Dyakonov and V. I. Perel'. "Spin relaxation of conduction electrons in noncentrosymmetric semiconductors". In: *Sov. Phys. Solid State* 13 (1972), pp. 3023–3026.

[Epe14] G. E. Eperon, S. D. Stranks, C. Menelaou, M. B. Johnston, L. M. Herz, and H. J. Snaith. "Formamidinium lead trihalide: a broadly tunable perovskite for efficient planar heterojunction solar cells". In: *Energy Environ. Sci.* 7.3 (2014), pp. 982–988. DOI: 10.1039/C3EE43822H.

[Eve15] J. Even. "Pedestrian Guide to Symmetry Properties of the Reference Cubic Structure of 3D All-Inorganic and Hybrid Perovskites". In: *J. Phys. Chem. Lett* 6.12 (2015), pp. 2238–2242.

[Fab16] D. H. Fabini, C. C. Stoumpos, G. Laurita, A. Kaltzoglou, A. G. Kontos, P. Falaras, M. G. Kanatzidis, and R. Seshadri. "Reentrant Structural and Optical Properties and Large Positive Thermal Expansion in Perovskite Formamidinium Lead Iodide". In: *Angewandte Chemie International Edition* 55.49 (2016), pp. 15392–15396. DOI: https://doi.org/10.1002/anie.201609538.

[Far46] M. Faraday. "I. Experimental researches in electricity.—Nineteenth series". In: *Philosophical Transactions of the Royal Society of London* 136 (1846), pp. 1–20. DOI: 10.1098/rstl.1846.0001.

[Fen20] Y. Feng, L. Pan, H. Wei, et al. "Low defects density $CsPbBr_3$ single crystals grown by an additive assisted method for gamma-ray detection". In: *Journal of Materials Chemistry C* 8.33 (2020), pp. 11360–11368. DOI: 10.1039/D0TC02706E.

[Fok10] L. V. Fokina, I. A. Yugova, D. R. Yakovlev, et al. "Spin dynamics of electrons and holes in InGaAs/GaAs quantum wells at millikelvin temperatures". In: *Physical Review B* 81.19 (2010), p. 195304. DOI: 10.1103/PhysRevB.81.195304.

[Fox01] A. Fox. *Optical Properties of Solids*. Oxford master series in condensed matter physics. Oxford University Press, 2001.

[Fra12] F. Fras, B. Eble, B. Siarry, F. Bernardot, A. Miard, A. Lemaître, C. Testelin, and M. Chamarro. "Hole spin mode locking and coherent dynamics in a largely inhomogeneous ensemble of *p*-doped InAs quantum dots". In: *Physical Review B* 86.16 (2012), p. 161303. DOI: 10.1103/PhysRevB.86.161303.

[Fro14] J. M. Frost, K. T. Butler, F. Brivio, C. H. Hendon, M. van Schilfgaarde, and A. Walsh. "Atomistic Origins of High-Performance in Hybrid Halide Perovskite Solar Cells". In: *Nano Letters* 14.5 (2014), pp. 2584–2590. DOI: 10.1021/nl500390f.

[Fro16] J. M. Frost and A. Walsh. "What Is Moving in Hybrid Halide Perovskite Solar Cells?" In: *Acc. Chem. Res.* 49.3 (2016), pp. 528–535. DOI: 10.1021/acs.accounts.5b00431.

[Frö79] D. Fröhlich, K. Heidrich, H. Künzel, G. Trendel, and J. Treusch. "Cesium-trihalogen-plumbates a new class of ionic semiconductors". In: *Journal of Luminescence* 18-19 (1979), pp. 385–388. DOI: 10.1016/0022-2313(79)90146-7.

[Fu19] Y. Fu, H. Zhu, J. Chen, M. P. Hautzinger, X.-Y. Zhu, and S. Jin. "Metal halide perovskite nanostructures for optoelectronic applications and the study of physical properties". In: *Nat. Rev. Mater.* 4 (2019), pp. 169–188.

[Fu20] Y. Fu and X. Kong. "Magnetic Resonance for Challenging Quadrupolar Halide Spins in Perovskites". In: *ACS Central Science* 6.7 (2020), pp. 1037–1039. DOI: 10.1021/acscentsci.0c00814.

[Fuj74] Y. Fujii, S. Hoshino, Y. Yamada, and G. Shirane. "Neutron-scattering study on phase transitions of $CsPbCl_3$". In: *Physical Review B* 9.10 (1974), pp. 4549–4559. DOI: 10.1103/PhysRevB.9.4549.

[GA21] G. Garcia-Arellano, G. Trippé-Allard, L. Legrand, et al. "Energy Tuning of Electronic Spin Coherent Evolution in Methylammonium Lead Iodide Perovskites". In: *The Journal of Physical Chemistry Letters* 12.34 (2021), pp. 8272–8279. DOI: 10.1021/acs.jpclett.1c01790.

[Gal16] K. Galkowski, A. Mitioglu, A. Miyata, et al. "Determination of the exciton binding energy and effective masses for methylammonium and formamidinium lead tri-halide perovskite semiconductors". In: *Energy & Environmental Science* 9.3 (2016), pp. 962–970. DOI: 10.1039/C5EE03435C.

[Gal17] K. Galkowski. "Magneto-optical and microscopic properties of organo lead halide perovskites". PhD thesis. Université Paul Sabatier - Toulouse III, 2017.

[Gla12a] M. M. Glazov. "Coherent spin dynamics of electrons and excitons in nanostructures (a review)". In: *Phys. Solid State* 54 (2012), pp. 1–27.

[Gla12b] M. M. Glazov, I. A. Yugova, and A. L. Efros. "Electron spin synchronization induced by optical nuclear magnetic resonance feedback". In: *Physical Review B* 85.4 (2012), p. 041303. DOI: 10.1103/PhysRevB.85.041303.

[Gla18] M. M. Glazov. *Electron & Nuclear Spin Dynamics in Semiconductor Nanostructures*. Oxford: Oxford University Press, 2018.

[Gla72] A. M. Glazer. "The classification of tilted octahedra in perovskites". In: *Acta Crystallographica Section B: Structural Crystallography and Crystal Chemistry* 28.11 (1972), pp. 3384–3392. DOI: 10.1107/S0567740872007976.

[Gla75] A. M. Glazer. "Simple ways of determining perovskite structures". In: *Acta Crystallographica Section A: Crystal Physics, Diffraction, Theoretical and General Crystallography* 31.6 (1975), pp. 756–762. DOI: 10.1107/S0567739475001635.

[Gle13] A. M. Glezer and I. E. Permyakova. *Melt-Quenched Nanocrystals*. CRC Press, 2013.

[Gol26] V. M. Goldschmidt. "Die Gesetze der Krystallochemie". In: *Naturwissenschaften* 14.21 (1926), pp. 477–485. DOI: 10.1007/BF01507527.

[Gre06a] A. Greilich, R. Oulton, E. A. Zhukov, et al. "Optical Control of Spin Coherence in Singly Charged (In,Ga)As/GaAs Quantum Dots". In: *Physical Review Letters* 96.22 (2006), p. 227401. DOI: 10.1103/PhysRevLett.96.227401.

[Gre06b] A. Greilich, D. R. Yakovlev, A. Shabaev, et al. "Mode Locking of Electron Spin Coherences in Singly Charged Quantum Dots". In: *Science* 313.5785 (2006), pp. 341–345. DOI: 10.1126/science.1128215.

[Gre07] A. Greilich. "Spin Coherence of Carriers in InGaAs/GaAs Quantum Wells and Quantum Dots". PhD thesis. Dortmund, Germany: TU Dortmund, 2007.

[Hö21] J. Höcker, F. Brust, M. Armer, and V. Dyakonov. "A temperature-reduced method for the rapid growth of hybrid perovskite single crystals with primary alcohols". In: *Cryst. Eng. Comm.* 23 (2021), pp. 2202–2207. DOI: 10.1039/D0CE01759K.

[Hä91] H. G. Häfele. "Spin-Flip Raman Scattering". In: *Landau Level Spectroscopy*. Ed. by G. Landwehr and E. I. Rashba. Vol. 27. Elsevier Amsterdam, 1991, pp. 208–275. doi: 10.1016/B978-0-444-88535-7.50012-1.

[Har18] J. R. Harwell, J. L. Payne, M. T. Sajjad, et al. "Role of lattice distortion and A site cation in the phase transitions of methylammonium lead halide perovskites". In: *Phys. Rev. Materials* 2.6 (2018), p. 065404. doi: 10.1103/PhysRevMaterials.2.065404.

[He21] Y. He, C. C. Stoumpos, I. Hadar, et al. "Demonstration of Energy-Resolved γ-Ray Detection at Room Temperature by the CsPbCl3 Perovskite Semiconductor". In: *Journal of the American Chemical Society* 143.4 (2021), pp. 2068–2077. doi: 10.1021/jacs.0c12254.

[Hei15] F. Heisterkamp, E. A. Zhukov, A. Greilich, D. R. Yakovlev, V. L. Korenev, A. Pawlis, and M. Bayer. "Longitudinal and transverse spin dynamics of donor-bound electrons in fluorine-doped ZnSe: Spin inertia versus Hanle effect". In: *Physical Review B* 91.23 (2015), p. 235432. doi: 10.1103/PhysRevB.91.235432.

[Hei16] F. Heisterkamp, E. Kirstein, A. Greilich, E. A. Zhukov, T. Kazimierczuk, D. R. Yakovlev, A. Pawlis, and M. Bayer. "Dynamics of nuclear spin polarization induced and detected by coherently precessing electron spins in fluorine-doped ZnSe". In: *Phys. Rev. B* 93.8 (2016), p. 081409.

[Hem92] R. J. Hemley and R. E. Cohen. "Silicate Perovskite". In: *Annual Review of Earth and Planetary Sciences* 20.1 (1992), pp. 553–600. doi: 10.1146/annurev.ea.20.050192.003005.

[Hir78] S. Hirotsu and T. Suzuki. "Elastic Constants and Thermal Expansion of $CsPbCl_3$". In: *Journal of the Physical Society of Japan* 44.5 (1978), pp. 1604–1611. doi: 10.1143/JPSJ.44.1604.

[Hir94] M. Hirasawa, T. Ishihara, T. Goto, K. Uchida, and N. Miura. "Magnetoabsorption of the lowest exciton in perovskite-type compound $(CH_3NH_3)PbI_3$". In: *Physica B: Condensed Matter* 201 (1994), pp. 427–430. doi: 10.1016/0921-4526(94)91130-4.

[How98] C. J. Howard and H. T. Stokes. "Group-Theoretical Analysis of Octahedral Tilting in Perovskites". In: *Acta Crystallographica Section B: Structural Science* 54.6 (1998), pp. 782–789. doi: 10.1107/S0108768198004200.

[Hua21] G. Huang, S. Rassel, J. Qu, S. Xu, C. Wang, and D. Ban. "Manipulation of spin splitting in two-dimensional lead bromide perovskite Rashba piezoelectrics". In: *ACS Appl. Electron. Mater.* 3.1 (2021), pp. 285–291.

[Ito79] H. Ito, J. Nakahara, and R. Onaka. "Magneto-optical Study of the Exciton States in $CsPbCl_3$". In: *Journal of the Physical Society of Japan* 47.6 (1979), pp. 1927–1935. doi: 10.1143/JPSJ.47.1927.

[Ivc05] E. L. Ivchenko. *Optical spectroscopy of semiconductor nanostructures*. Harrow, UK: Alpha Science Int., 2005.

[Ivc18] E. L. Ivchenko. "Magnetic Circular Polarization of Exciton Photoluminescence". In: *Physics of the Solid State* 60.8 (2018), pp. 1514–1526. doi: 10.1134/S1063783418080127.

[Jam75] T. L. James. *Nuclear Magnetic Resonance in Biochemistry*. New York: Academic Press, 1975.

[Jen19] A. K. Jena, A. Kulkarni, and T. Miyasaka. "Halide Perovskite Photovoltaics: Background, Status, and Future Prospects". In: *Chem. Rev.* 119.5 (2019), pp. 3036–3103. doi: 10.1021/acs.chemrev.8b00539.

[Jeo15] N. J. Jeon, J. H. Noh, W. S. Yang, Y. C. Kim, S. Ryu, J. Seo, and S. I. Seok. "Compositional engineering of perovskite materials for high-performance solar cells". In: *Nature* 517.7535 (2015). doi: 10.1038/nature14133.

[Jeo21] J. Jeong, M. Kim, J. Seo, et al. "Pseudo-halide anion engineering for α-$FAPbI_3$ perovskite solar cells". In: *Nature* 592.7854 (2021), pp. 381–385. doi: 10.1038/s41586-021-03406-5.

[Kal91] V. K. Kalevich and V. L. Korenev. "Optical polarization of nuclei and ODNMR in GaAs/AlGaAs quantum wells". In: *Appl. Magn. Reson.* 2 (1991), pp. 397–411.

[Kep15] M. Kepenekian, R. Robles, C. Katan, D. Sapori, L. Pedesseau, and J. Even. "Rashba and Dresselhaus effects in hybrid organic-inorganic perovskites: from basics to devices". In: *ACS Nano* 9 (2015), pp. 11557–11567.

[Ker77] J. Kerr. "XLIII. On rotation of the plane of polarization by reflection from the pole of a magnet". In: *The London, Edinburgh, and Dublin Philosophical Magazine and Journal of Science* 3.19 (1877), pp. 321–343. doi: 10.1080/14786447708639245.

[Kie15] G. Kieslich, S. Sun, and A. K. Cheetham. "An extended Tolerance Factor approach for organic–inorganic perovskites". In: *Chem. Sci.* 6.6 (2015), pp. 3430–3433. doi: 10.1039/C5SC00961H.

[Kim14] M. Kim, J. Im, A. J. Freeman, J. Ihm, and H. Jin. "Switchable $S = 1/2$ and $J = 1/2$ Rashba bands in ferroelectric halide perovskites". In: *PNAS* 111 (2014), pp. 6900–6904.

[Kir19] M. S. Kirschner, B. T. Diroll, P. Guo, et al. "Photoinduced, reversible phase transitions in all-inorganic perovskite nanocrystals". In: *Nature Communications* 10.1 (2019), p. 504. doi: 10.1038/s41467-019-08362-3.

[Kir21a] E. Kirstein, D. R. Yakovlev, M. M. Glazov, et al. "The Landé factors of electrons and holes in lead halide perovskites: universal dependence on the band gap". In: *arXiv:2112.15384 [cond-mat]* (2021). arXiv: 2112.15384.

[Kir21b] E. Kirstein, D. R. Yakovlev, M. M. Glazov, et al. "Lead-Dominated Hyperfine Interaction Impacting the Carrier Spin Dynamics in Halide Perovskites". In: *Advanced Materials* 34.1 (2021), p. 2105263. doi: 10.1002/adma.202105263.

[Kir22] E. Kirstein, D. R. Yakovlev, E. A. Zhukov, J. Höcker, V. Dyakonov, and M. Bayer. "Spin dynamics of electrons and holes interacting with nuclei in $MAPbI_3$ perovskite single crystals". In: *arXiv:2201.06867* (2022).

[Kit05] C. Kittel. *Introduction to solid state physics*. eng. 8. ed. Hoboken, NJ: Wiley, 2005.

[Koj09] A. Kojima, K. Teshima, Y. Shirai, and T. Miyasaka. "Organometal Halide Perovskites as Visible-Light Sensitizers for Photovoltaic Cells". In: *J. Am. Chem. Soc.* 131.17 (2009), pp. 6050–6051. doi: 10.1021/ja809598r.

[Kol21] E. V. Kolobkova, M. S. Kuznetsova, and N. V. Nikonorov. "Perovskite $CsPbX_3$ (X=Cl, Br, I) Nanocrystals in fluorophosphate glasses". In: *Journal of Non-Crystalline Solids* 563 (2021), p. 120811. DOI: 10.1016/j.jnoncrysol.2021.120811.

[Kor11] V. L. Korenev. "Multiple stable states of a periodically driven electron spin in a quantum dot using circularly polarized light". In: *Physical Review B* 83.23 (2011), p. 235429. DOI: 10.1103/PhysRevB.83.235429.

[Kos19] A. N. Kosarev, S. V. Poltavtsev, L. E. Golub, et al. "Microscopic dynamics of electron hopping in a semiconductor quantum well probed by spin-dependent photon echoes". In: *Physical Review B* 100.12 (2019), p. 121401. DOI: 10.1103/PhysRevB.100.121401.

[Kri21] F. Krieg, P. C. Sercel, M. Burian, et al. "Monodisperse Long-Chain Sulfobetaine-Capped $CsPbBr_3$ Nanocrystals and Their Superfluorescent Assemblies". In: *ACS Central Science* 7.1 (2021), pp. 135–144. DOI: 10.1021/acscentsci.0c01153.

[Lan28] G. S. Landsberg and L. Mandelstam. "Eine neue Erscheinung bei der Lichtzerstreuung in Krystallen". de. In: *Naturwissenschaften* 16.28 (1928), pp. 557–558. DOI: 10.1007/BF01506807.

[Lia15] Z. Lian, Q. Yan, Q. Lv, et al. "High-Performance Planar-Type Photodetector on (100) Facet of $MAPbI_3$ Single Crystal". In: *Scientific Reports* 5.1 (2015), p. 16563. DOI: 10.1038/srep16563.

[Liu14] F. Liu, A. V. Rodina, D. R. Yakovlev, et al. "Exciton spin dynamics of colloidal CdTe nanocrystals in magnetic fields". In: *Physical Review B* 89.11 (2014), p. 115306. DOI: 10.1103/PhysRevB.89.115306.

[Liu19a] J. Liu, L. Shen, Y. Chen, et al. "Highly luminescent and ultrastable cesium lead halide perovskite nanocrystal glass for plant-growth lighting engineering". In: *Journal of Materials Chemistry C* 7.43 (2019), pp. 13606–13612. DOI: 10.1039/C9TC04799A.

[Liu19b] L. Liu, R. Zhao, C. Xiao, et al. "Size-Dependent Phase Transition in Perovskite Nanocrystals". In: *The Journal of Physical Chemistry Letters* 10.18 (2019), pp. 5451–5457. DOI: 10.1021/acs.jpclett.9b02058.

[Lon21] N. Long, Y. Fu, T. Xu, et al. "Nanocrystallization and optical properties of $CsPbBr_{3-x}I_x$ perovskites in chalcogenide glasses". In: *Journal of the European Ceramic Society* 41.8 (2021), pp. 4584–4589. DOI: 10.1016/j.jeurceramsoc.2021.03.034.

[Lv17] Q. Lv, W. He, Z. Lian, J. Ding, Q. Li, and Q. Yan. "Anisotropic moisture erosion of $CH_3NH_3PbI_3$ single crystals". In: *CrystEngComm* 19.6 (2017), pp. 901–904. DOI: 10.1039/C6CE02317G.

[Mar19] S. Markmann, C. Reichl, W. Wegscheider, and G. Salis. "Universal nuclear focusing of confined electron spins". In: *Nature Communications* 10.1 (2019), p. 1097. DOI: 10.1038/s41467-019-08882-y.

[Mas14] F. Masiello, G. Cembali, A. I. Chumakov, S. H. Connell, C. Ferrero, J. Härtwig, I. Sergeev, and P. Van Vaerenbergh. "Rocking curve measurements revisited". In: *Journal of Applied Crystallography* 47.4 (2014), pp. 1304–1314. doi: 10.1107/S1600576714012527.

[Mas20] S. Masi, A. F. Gualdrón-Reyes, and I. Mora-Seró. "Stabilization of Black Perovskite Phase in $FAPbI_3$ and $CsPbI_3$". In: *ACS Energy Lett.* 5.6 (2020), pp. 1974–1985. doi: 10.1021/acsenergylett.0c00801.

[Mei84] F. Meier and B. P Zakharchenya, eds. *Optical Orientation*. Amsterdam: Elsevier, 1984.

[Mer05] H. Mertins, S. Valencia, A. Gaupp, W. Gudat, P. Oppeneer, and C. Schneider. "Magneto-optical polarization spectroscopy with soft X-rays". In: *Applied Physics A* 80 (2005), pp. 1011–1020. doi: 10.1007/s00339-004-3129-5.

[Mik18] A. V. Mikhailov, V. V. Belykh, D. R. Yakovlev, P. S. Grigoryev, J. P. Reithmaier, M. Benyoucef, and M. Bayer. "Electron and hole spin relaxation in InP-based self-assembled quantum dots emitting at telecom wavelengths". In: *Physical Review B* 98.20 (2018), p. 205306. doi: 10.1103/PhysRevB.98.205306.

[Miy15] A. Miyata, A. Mitioglu, P. Plochocka, O. Portugall, J. T.-W. Wang, S. D. Stranks, H. J. Snaith, and R. J. Nicholas. "Direct measurement of the exciton binding energy and effective masses for charge carriers in organic–inorganic tri-halide perovskites". In: *Nature Physics* 11.7 (2015), pp. 582–587. doi: 10.1038/nphys3357.

[Moc17] R. W. Mocek, V. L. Korenev, M. Bayer, et al. "High-efficiency optical pumping of nuclear polarization in a GaAs quantum well". In: *Physical Review B* 96.20 (2017), p. 201303. doi: 10.1103/PhysRevB.96.201303.

[Mur12] M. Murakami, Y. Ohishi, N. Hirao, and K. Hirose. "A perovskitic lower mantle inferred from high-pressure, high-temperature sound velocity data". In: *Nature* 485.7396 (2012), pp. 90–94. doi: 10.1038/nature11004.

[Mur20] B. Murali, H. K. Kolli, J. Yin, R. Ketavath, O. M. Bakr, and O. F. Mohammed. "Single Crystals: The Next Big Wave of Perovskite Optoelectronics". In: *ACS Materials Letters* 2.2 (2020), pp. 184–214. doi: 10.1021/acsmaterialslett.9b00290.

[Mus21] A. Musiienko, D. R. Ceratti, J. Pipek, et al. "Defects in Hybrid Perovskites: The Secret of Efficient Charge Transport". en. In: *Advanced Functional Materials* 31.48 (2021), p. 2104467. doi: 10.1002/adfm.202104467.

[MY21] A. R. b. Mohd Yusoff, A. Mahata, M. Vasilopoulou, et al. "Observation of large Rashba spin–orbit coupling at room temperature in compositionally engineered perovskite single crystals and application in high performance photodetectors". In: *Mater. Today* 46 (2021), pp. 18–27. doi: 10.1016/j.mattod.2021.01.027.

[Naz17] O. Nazarenko, S. Yakunin, V. Morad, I. Cherniukh, and M. V. Kovalenko. "Single crystals of caesium formamidinium lead halide perovskites: solution growth and gamma dosimetry". In: *NPG Asia Materials* 9.4 (2017), e373. doi: 10.1038/am.2017.45.

[Ned15] G. Nedelcu, L. Protesescu, S. Yakunin, M. I. Bodnarchuk, M. J. Grotevent, and M. V. Kovalenko. "Fast Anion-Exchange in Highly Luminescent Nanocrystals of Cesium Lead Halide Perovskites ($CsPbX_3$, X = Cl, Br, I)". In: *Nano Letters* 15.8 (2015), pp. 5635–5640. DOI: 10.1021/acs.nanolett.5b02404.

[Nes18] M. O. Nestoklon, S. V. Goupalov, R. I. Dzhioev, et al. "Optical orientation and alignment of excitons in ensembles of inorganic perovskite nanocrystals". In: *Phys. Rev. B* 97 (2018), p. 235304.

[Nes21] M. O. Nestoklon. "Tight-binding description of inorganic lead halide perovskites in cubic phase". In: *Computational Materials Science* 196 (2021), p. 110535. DOI: https://doi.org/10.1016/j.commatsci.2021.110535.

[Nie16] D. Niesner, M. Wilhelm, I. Levchuk, A. Osvet, S. Shrestha, M. Batentschuk, C. Brabec, and T. Fauster. "Giant Rashba splitting in $CH_3NH_3PbBr_3$ organic-inorganic perovskite". In: *Phys. Rev. Lett* 117 (2016), p. 126401.

[Nis20] K. Nishimura, M. A. Kamarudin, D. Hirotani, et al. "Lead-free tin-halide perovskite solar cells with 13% efficiency". In: *Nano Energy* 74 (2020), p. 104858. DOI: 10.1016/j.nanoen.2020.104858.

[Nol77] A. Nolle. "^{207}Pb magnetic shielding anisotropy in $Pb(NO_3)_2$, $PbCO_3$, $PbCrO_4$, $PbMo0_4$ and $PbWO_4$ by Fourier transform NMR". In: *Zeitschrift für Naturforschung A* 32a (1977), pp. 964–967.

[Nre] *Best Research-Cell Efficiency Chart*. https://www.nrel.gov/pv/cell-efficiency.html. 2021-06-09.

[Ode17] P. Odenthal, W. Talmadge, N. Gundlach, et al. "Spin-polarized exciton quantum beating in hybrid organic–inorganic perovskites". In: *Nature Phys.* 13.9 (2017), pp. 894–899. DOI: 10.1038/nphys4145.

[Oku15] T. Oku. "Crystal Structures of $CH_3NH_3PbI_3$ and Related Perovskite Compounds Used for Solar Cells". In: *Solar Cells - New Approaches and Reviews* (2015). DOI: 10.5772/59284.

[Oku20] T. Oku. "Crystal structures of perovskite halide compounds used for solar cells". In: *REV. ADV. MAT. SCI.* 59.1 (2020), pp. 264–305. DOI: 10.1515/rams-2020-0015.

[Ove53] A. W. Overhauser. "Polarization of Nuclei in Metals". In: *Physical Review* 92.2 (1953), pp. 411–415. DOI: 10.1103/PhysRev.92.411.

[Pag77] D. Paget, G. Lampel, B. Sapoval, and V. I. Safarov. "Low field electron-nuclear spin coupling in gallium arsenide under optical pumping conditions". In: *Physical Review B* 15.12 (1977), pp. 5780–5796. DOI: 10.1103/PhysRevB.15.5780.

[Pha22] M. T. Pham, E. Amerling, T. A. Ngo, et al. "Strong Rashba-Dresselhaus Effect in Nonchiral 2D Ruddlesden-Popper Perovskites". In: *Advanced Optical Materials* 10.1 (2022), p. 2101232. DOI: 10.1002/adom.202101232.

[Piv20] L. Piveteau, V. Morad, and M. V. Kovalenko. "Solid-State NMR and NQR Spectroscopy of Lead-Halide Perovskite Materials". In: *J. Am. Chem. Soc.* 142.46 (2020), pp. 19413–19437. DOI: 10.1021/jacs.0c07338.

[Pra17] R. Prasanna, A. Gold-Parker, T. Leijtens, B. Conings, A. Babayigit, H.-G. Boyen, M. F. Toney, and M. D. McGehee. "Band Gap Tuning via Lattice Contraction and Octahedral Tilting in Perovskite Materials for Photovoltaics". In: *J. Am. Chem. Soc.* 139.32 (2017), pp. 11117–11124. DOI: 10.1021/jacs.7b04981.

[Pri21] A. Privitera, M. Righetto, F. Cacialli, and M. K. Riede. "Perspectives of Organic and Perovskite-Based Spintronics". In: *Advanced Optical Materials* 9.14 (2021), p. 2100215. DOI: 10.1002/adom.202100215.

[Ram28] C. V. Raman and K. S. Krishnan. "The Negative Absorption of Radiation". en. In: *Nature* 122.3062 (1928), pp. 12–13. DOI: 10.1038/122012b0.

[Rot59] L. M. Roth, B. Lax, and S. Zwerdling. "Theory of Optical Magneto-Absorption Effects in Semiconductors". In: *Phys. Rev.* 114.1 (1959), p. 90. DOI: 10.1103/PhysRev.114.90.

[Saj20] M. Sajedi, M. Krivenkov, D. Marchenko, A. Varykhalov, J. Sánchez-Barriga, E. D. L. Rienks, and O. Rader. "Absence of a giant Rashba effect in the valence band of lead halide perovskites". In: *Physical Review B* 102.8 (2020), p. 081116. DOI: 10.1103/PhysRevB.102.081116.

[Sak11] J. J. Sakurai and J. Napolitano. *Modern quantum mechanics*. 2nd ed. Boston: Addison-Wesley, 2011.

[Sak69] T. Sakudo, H. Unoki, Y. Fujii, J. Kobayashi, and M. Yamada. "A new structural phase transition in $CsPbCl_3$". In: *Physics Letters A* 28.8 (1969), pp. 542–543. DOI: 10.1016/0375-9601(69)90094-2.

[Sar17] R. Saran, A. Heuer-Jungemann, A. G. Kanaras, and R. J. Curry. "Giant Bandgap Renormalization and Exciton–Phonon Scattering in Perovskite Nanocrystals". en. In: *Advanced Optical Materials* 5.17 (2017), p. 1700231. DOI: 10.1002/adom.201700231.

[Sch12] P. Scherrer. "Bestimmung der inneren Struktur und der Größe von Kolloidteilchen mittels Röntgenstrahlen". In: *Kolloidchemie Ein Lehrbuch*. Ed. by R. Zsigmondy. Chemische Technologie in Einzeldarstellungen. Berlin, Heidelberg: Springer, 1912, pp. 387–409. DOI: 10.1007/978-3-662-33915-2_7.

[Sha87] S. Sharma, N. Weiden, and A. Weiss. "^{207}Pb and ^{205}Tl NMR on perovskite type crystals $APbX_3$ (A = Cs, Tl, X = Br, I)". In: *Z. Naturforsch., A: Phys. Sci.* 42 (1987), pp. 1313–1320.

[Sir97] A. A. Sirenko, T. Ruf, M. Cardona, D. R. Yakovlev, W. Ossau, A. Waag, and G. Landwehr. "Electron and hole g factors measured by spin-flip Raman scattering in $CdTe/Cd_{(1-x)}Mg_xTe$ single quantum wells". In: *Phys. Rev. B* 56.4 (1997), pp. 2114–2119. DOI: 10.1103/PhysRevB.56.2114.

[Sli90] C. P. Slichter. *Principles of Magnetic Resonance*. en. 3rd ed. Springer Series in Solid-State Sciences. Berlin Heidelberg: Springer-Verlag, 1990. DOI: 10.1007/978-3-662-09441-9.

[Smi18] D. S. Smirnov, E. A. Zhukov, E. Kirstein, et al. "Theory of spin inertia in singly charged quantum dots". In: *Physical Review B* 98.12 (2018), p. 125306. DOI: 10.1103/PhysRevB.98.125306.

[Sto13] C. C. Stoumpos, C. D. Malliakas, and M. G. Kanatzidis. "Semiconducting Tin and Lead Iodide Perovskites with Organic Cations: Phase Transitions, High Mobilities, and Near-Infrared Photoluminescent Properties". In: *Inorganic Chemistry* 52.15 (2013), pp. 9019–9038. DOI: 10.1021/ic401215x.

[Sut16] B. R. Sutherland and E. H. Sargent. "Perovskite photonic sources". In: *Nature Photonics* 10.5 (2016), pp. 295–302. DOI: 10.1038/nphoton.2016.62.

[Swa03] I. P. Swainson, R. P. Hammond, C. Soullière, O. Knop, and W. Massa. "Phase transitions in the perovskite methylammonium lead bromide, $CH_3ND_3PbBr_3$". In: *Journal of Solid State Chemistry* 176.1 (2003), pp. 97–104. DOI: 10.1016/S0022-4596(03)00352-9.

[Tan03] K. Tanaka, T. Takahashi, T. Ban, T. Kondo, K. Uchida, and N. Miura. "Comparative study on the excitons in lead-halide-based perovskite-type crystals $CH_3NH_3PbBr_3$ $CH_3NH_3PbI_3$". In: *Solid State Communications* 127.9 (2003), pp. 619–623. DOI: 10.1016/S0038-1098(03)00566-0.

[Tar18] F. F. Targhi, Y. S. Jalili, and F. Kanjouri. "$MAPbI_3$ and $FAPbI_3$ perovskites as solar cells: Case study on structural, electrical and optical properties". In: *Results in Physics* 10 (2018), pp. 616–627.

[TN20] T. T. Thu Nguyen, Y. Kim, S. Bae, et al. "Raman Scattering Studies of the Structural Phase Transitions in Single-Crystalline $CH_3NH_3PbCl_3$". In: *The Journal of Physical Chemistry Letters* 11.10 (2020), pp. 3773–3781. DOI: 10.1021/acs.jpclett.0c00920.

[Tre82] G. Trendel. "Electronic and phonon properties of the plumbates CsPbCl , CsPbBr and their mixed crystals ; Elektronische und phononische Eigenschaften der Plumbate CsPbCl , CsPbBr und ihrer Mischkristalle". German. Hochschulschrift. Dortmund: Dortmund, 1982.

[Tsc14] O. Tschauner, C. Ma, J. R. Beckett, C. Prescher, V. B. Prakapenka, and G. R. Rossman. "Discovery of bridgmanite, the most abundant mineral in Earth, in a shocked meteorite". In: *Science* (2014). DOI: 10.1126/science.1259369.

[Var19] P. R. Varadwaj, A. Varadwaj, H. M. Marques, and K. Yamashita. "Significance of hydrogen bonding and other noncovalent interactions in determining octahedral tilting in the CH_3 NH_3 PbI_3 hybrid organic-inorganic halide perovskite solar cell semiconductor". In: *Scientific Reports* 9.1 (2019), p. 50. DOI: 10.1038/s41598-018-36218-1.

[Vla17] M. Vladimirova, S. Cronenberger, D. Scalbert, et al. "Nuclear spin relaxation in n-GaAs: From insulating to metallic regime". In: *Phys. Rev. B* 95.12 (2017), p. 125312.

[Wal20] A. Walsh. *WMD-group/hybrid-perovskites* *https://github.com/WMD-group/hybrid-perovskites*. 2020-02-12.

[Wan19] J. Wang, C. Zhang, H. Liu, et al. "Spin-optoelectronic devices based on hybrid organic-inorganic trihalide perovskites". In: *Nat. Commun.* 10 (2019), p. 129.

[Wei19] H. Wei and J. Huang. "Halide lead perovskites for ionizing radiation detection". In: *Nat. Commun.* 10 (2019), p. 1066.

[Whi16] P. S. Whitfield, N. Herron, W. E. Guise, K. Page, Y. Q. Cheng, I. Milas, and M. K. Crawford. "Structures, Phase Transitions and Tricritical Behavior of the Hybrid Perovskite Methyl Ammonium Lead Iodide". In: *Scientific Reports* 6.1 (2016), p. 35685. doi: 10.1038/srep35685.

[Wil21] R. G. Wilks, A. Erbing, G. Sadoughi, et al. "Dynamic Effects and Hydrogen Bonding in Mixed-Halide Perovskite Solar Cell Absorbers". In: *The Journal of Physical Chemistry Letters* 12.16 (2021), pp. 3885–3890. doi: 10.1021/acs.jpclett.1c00745.

[Win03] R. Winkler. *Spin–Orbit Coupling Effects in Two-Dimensional Electron and Hole Systems*. en. Ed. by R. Winkler. Springer Tracts in Modern Physics. Berlin, Heidelberg: Springer, 2003. doi: 10.1007/978-3-540-36616-4_1.

[Wra90] B. Wrackmeyer and K. Horchler. "^{207}Pb-NMR parameters". In: *Annual Reports on NMR Spectroscopy*. Ed. by G. A. Webb. Academic Press, 1990, vol. 22 249–306.

[Xu21] Y. Xu, X. Zhao, M. Xia, and X. Zhang. "Perovskite nanocrystal doped all-inorganic glass for X-ray scintillators". In: *Journal of Materials Chemistry C* 9.16 (2021), pp. 5452–5459. doi: 10.1039/D0TC05979J.

[Yak08] D. R. Yakovlev and M. Bayer. "Coherent Spin Dynamics of Carriers". In: *Spin Physics in Semiconductors*. Ed. by M. I. Dyakonov. Spin Physics in Semiconductors. Berlin, Heidelberg: Springer, 2008, pp. 135–177. doi: 10.1007/978-3-540-78820-1_6.

[Yin05] Y. Yin and A. P. Alivisatos. "Colloidal nanocrystal synthesis and the organic–inorganic interface". en. In: *Nature* 437.7059 (2005), pp. 664–670. doi: 10.1038/nature04165.

[Yu16] Z. G. Yu. "Effective-mass model and magneto-optical properties in hybrid perovskites". In: *Scientific Reports* 6 (2016), p. 28576. doi: 10.1038/srep28576.

[Yu19] C.-J. Yu. "Advances in modelling and simulation of halide perovskites for solar cell applications". In: *Journal of Physics: Energy* 1.2 (2019), p. 022001. doi: 10.1088/2515-7655/aaf143.

[Yug07] I. A. Yugova, A. Greilich, D. R. Yakovlev, et al. "Universal behavior of the electron g factor in GaAs/$Al_xGa_{(1-x)}$As quantum wells". In: *Phys. Rev. B* 75.24 (2007), p. 245302. doi: 10.1103/PhysRevB.75.245302.

[Yug09] I. A. Yugova, M. M. Glazov, E. L. Ivchenko, and Al. L. Efros. "Pump-probe Faraday rotation and ellipticity in an ensemble of singly charged quantum dots". In: *Physical Review B* 80.10 (2009), p. 104436. doi: 10.1103/PhysRevB.80.104436.

[Yug12] I. A. Yugova, M. M. Glazov, D. R. Yakovlev, A. A. Sokolova, and M. Bayer. "Coherent spin dynamics of electrons and holes in semiconductor quantum wells and quantum dots under periodical optical excitation: Resonant spin amplification versus spin mode locking". In: *Physical Review B* 85.12 (2012), p. 125304. doi: 10.1103/PhysRevB.85.125304.

[Zei16] W. G. Zeier, A. Zevalkink, Z. M. Gibbs, G. Hautier, M. G. Kanatzidis, and G. J. Snyder. "Denken wie ein Chemiker: Thermoelektrika intuitiv". In: *Angewandte Chemie* 128.24 (2016), pp. 6938–6954. DOI: 10.1002/ange.201508381.

[Zha20a] Z. Zhang, D. Liu, and K. Wu. "First-principles study of structural stability, electronic and optical properties of GA-doped MAPbI3". In: *Spectrochimica Acta Part A: Molecular and Biomolecular Spectroscopy* 226 (2020), p. 117638. DOI: 10.1016/j.saa.2019.117638.

[Zha20b] Q. Zhao, A. Hazarika, L. T. Schelhas, et al. "Size-Dependent Lattice Structure and Confinement Properties in $CsPbI_3$ Perovskite Nanocrystals: Negative Surface Energy for Stabilization". In: *ACS Energy Letters* 5.1 (2020), pp. 238–247. DOI: 10.1021/acsenergylett.9b02395.

[Zha21a] X. Zhang, J.-X. Shen, M. E. Turiansky, and C. G. Van de Walle. "Minimizing hydrogen vacancies to enable highly efficient hybrid perovskites". In: *Nature Materials* (2021), pp. 1–6. DOI: 10.1038/s41563-021-00986-5.

[Zha21b] Y. Zhao, T. Heumueller, J. Zhang, et al. "A bilayer conducting polymer structure for planar perovskite solar cells with over 1,400 hours operational stability at elevated temperatures". In: *Nature Energy* (2021), pp. 1–9. DOI: 10.1038/s41560-021-00953-z.

[Zhu18] E. A. Zhukov, E. Kirstein, N. E. Kopteva, et al. "Discretization of the total magnetic field by the nuclear spin bath in fluorine-doped ZnSe". In: *Nature Communications* 9.1 (2018), pp. 1–8. DOI: 10.1038/s41467-018-04359-6.

List of my Publications

[Heisterkamp et al., 2015] Heisterkamp, F., Greilich, A., Zhukov, E. A., Kirstein, E., Kazimierczuk, T., Korenev, V. L., Yugova, I. A., Yakovlev, D. R., Pawlis, A., and Bayer, M. Inhomogeneous nuclear spin polarization induced by helicity-modulated optical excitation of fluorine-bound electron spins in ZnSe. *Phys. Rev. B*, 92(24):245441, 2015.

[Heisterkamp et al., 2016] Heisterkamp, F., Kirstein, E., Greilich, A., Zhukov, E. A., Kazimierczuk, T., Yakovlev, D. R., Pawlis, A., and Bayer, M. Dynamics of nuclear spin polarization induced and detected by coherently precessing electron spins in fluorine-doped ZnSe. *Phys. Rev. B*, 93(8):081409, 2016.

[Akimov et al., 2017] Akimov, I. A., Salewski, M., Kalitukha, I. V., Poltavtsev, S. V., Debus, J., Kudlacik, D., Sapega, V. F., Kopteva, N. E., Kirstein, E., Zhukov, E. A., Yakovlev, D. R., Karczewski, G., Wiater, M., Wojtowicz, T., Korenev, V. L., Kusrayev, Y. G., and Bayer, M. Direct measurement of the long-range $p - d$ exchange coupling in a ferromagnet-semiconductor Co/CdMgTe/CdTe quantum well hybrid structure. *Phys. Rev. B*, 96(18):184412, 2017.

[Smirnov et al., 2018] Smirnov, D. S., Zhukov, E. A., Kirstein, E., Yakovlev, D. R., Reuter, D., Wieck, A. D., Bayer, M., Greilich, A., and Glazov, M. M. Theory of spin inertia in singly charged quantum dots. *Phys. Rev. B*, 98(12):125306, 2018.

[Zhukov et al., 2018a] Zhukov, E. A., Kirstein, E., Kopteva, N. E., Heisterkamp, F., Yugova, I. A., Korenev, V. L., Yakovlev, D. R., Pawlis, A., Bayer, M., and Greilich, A. Discretization of the total magnetic field by the nuclear spin bath in fluorine-doped ZnSe. *Nat Commun*, 9(1):1–8, 2018a. ISSN 2041-1723.

[Zhukov et al., 2018b] Zhukov, E. A., Kirstein, E., Smirnov, D. S., Yakovlev, D. R., Glazov, M. M., Reuter, D., Wieck, A. D., Bayer, M., and Greilich, A. Spin inertia of resident and photoexcited carriers in singly charged quantum dots. *Phys. Rev. B*, 98(12):121304, 2018b.

[Afanasiev et al., 2019] Afanasiev, M. M., Kozyrev, N. V., Kirstein, E., Kalevich, V. K., Zhukov, E. A., Mantsevich, V. N., Krivenko, I. S., Karczewski, G., Yakovlev, D. R., Kusraev, Y. G., and Bayer, M. Electron g -factor in coupled quantum wells CdTe and CdMnTe. *J. Phys.: Conf. Ser.*, 1400:066023, 2019. ISSN 1742-6588, 1742-6596.

[Kopteva et al., 2019a] Kopteva, N. E., Kirstein, E., Zhukov, E. A., Hussain, M., Bhatti, A. S., Pawlis, A., Yakovlev, D. R., Bayer, M., and Greilich, A. Spin dephasing of electrons and holes in isotopically purified ZnSe/(Zn,Mg)Se quantum wells. *Phys. Rev. B*, 100(20):205415, 2019a.

[Kopteva et al., 2019b] Kopteva, N. E., Yugova, I. A., Zhukov, E. A., Kirstein, E., Evers, E., Belykh, V. V., Korenev, V. L., Yakovlev, D. R., Bayer, M., and Greilich, A. Theoretical Modeling of the Nuclear-Field Induced Tuning of the Electron Spin Precession for Localized Spins. *physica status solidi (b)*, 256(6):1800534, 2019b. ISSN 1521-3951.

[Korenev et al., 2019] Korenev, V. L., Kalitukha, I. V., Akimov, I. A., Sapega, V. F., Zhukov, E. A., Kirstein, E., Ken, O. S., Kudlacik, D., Karczewski, G., Wiater, M., Wojtowicz, T., Ilyinskaya, N. D., Lebedeva, N. M., Komissarova, T. A., Kusrayev, Y. G., Yakovlev, D. R., and Bayer, M. Low voltage control of exchange coupling in a ferromagnet-semiconductor quantum well hybrid structure. *Nat Commun*, 10(1):1–8, 2019. ISSN 2041-1723.

[Zhukov et al., 2019] Zhukov, E. A., Kusrayev, Y. G., Kirstein, E., Thomann, A., Salewski, M., Kozyrev, N. V., Yakovlev, D. R., and Bayer, M. Optical orientation of acceptor-bound hole magnetic polarons in bulk (Cd,Mn)Te. *Phys. Rev. B*, 99(11):115204, 2019.

[Kirstein et al., 2020] Kirstein, E., Kozyrev, N. V., Afanasiev, M. M., Mantsevich, V. N., Krivenko, I. S., Kalevich, V. K., Salewski, M., Chusnutdinow, S., Wojtowicz, T., Karczewski, G., Kusrayev, Y. G., Zhukov, E. A., Yakovlev, D. R., and Bayer, M. Short range proximity effect induced by exchange interaction in tunnel-coupled CdTe and (Cd,Mn)Te quantum wells. *Phys. Rev. B*, 101(3):035301, 2020.

[Smirnov et al., 2020] Smirnov, D. S., Zhukov, E. A., Yakovlev, D. R., Kirstein, E., Bayer, M., and Greilich, A. Spin polarization recovery and Hanle effect for charge carriers interacting with nuclear spins in semiconductors. *Phys. Rev. B*, 102(23):235413, 2020.

[Zhukov et al., 2020] Zhukov, E. A., Mantsevich, V. N., Yakovlev, D. R., Kopteva, N. E., Kirstein, E., Waag, A., Karczewski, G., Wojtowicz, T., and Bayer, M. Renormalization of the electron g factor in the degenerate two-dimensional electron gas of ZnSe- and CdTe-based quantum wells. *Phys. Rev. B*, 102(12):125306, 2020.

[Kirstein et al., 2021a] Kirstein, E., Yakovlev, D. R., Glazov, M. M., Zhukov, E. A., Kudlacik, D., Kalitukha, I. V., Sapega, V. F., Dimitriev, G. S., Semina, M. A., Nestoklon, M. O., Ivchenko, E. L., Kopteva, N. E., Dirin, D. N., Nazarenko, O., Kovalenko, M. V., Baumann, A., Höcker, J., Dyakonov, V., and Bayer, M. The Landé factors of electrons and holes in lead halide perovskites: universal dependence on the band gap. *arXiv:2112.15384 [cond-mat]*, 2021a. ArXiv: 2112.15384.

[Kirstein et al., 2021b] Kirstein, E., Zhukov, E. A., Smirnov, D. S., Nedelea, V., Greve, P., Kalitukha, I. V., Sapega, V. F., Pawlis, A., Yakovlev, D. R., Bayer, M., and Greilich, A. Extended spin coherence of the zinc-vacancy centers in ZnSe with fast optical access. *Communications Materials*, 2(1):1–8, 2021b. ISSN 2662-4443. doi:10.1038/s43246-021-00198-z.

[Kirstein et al., 2022a] Kirstein, E., Yakovlev, D. R., Glazov, M. M., Evers, E., Zhukov, E. A., Belykh, V. V., Kopteva, N. E., Kudlacik, D., Nazarenko, O., Dirin, D. N., Kovalenko, M. V., and Bayer, M. Lead-Dominated Hyperfine Interaction Impacting the Carrier Spin Dynamics in Halide Perovskites. *Advanced Materials*, 34(1):2105263, 2022a. ISSN 1521-4095. doi:10.1002/adma.202105263.

[Kirstein et al., 2022b] Kirstein, E., Yakovlev, D. R., Zhukov, E. A., Höcker, J., Dyakonov, V., and Bayer, M. Spin dynamics of electrons and holes interacting with nuclei in $MAPbI_3$ perovskite single crystals. *arXiv:2201.06867*, 2022b. ArXiv: 2201.06867.

Acknowledgement

During my studies, I was fortunate to be surrounded by many great people who helped and supported me and were simply good colleagues. I am indebted to many people in many ways, which is difficult to do justice to. So the following thanks can only be given in random order and remain incomplete.

First of all, I would like to thank my supervisors, Alex Greilich and Dmitry Yakovlev, with whom I was able to realise numerous projects and on whose expertise I could always rely. I would also like to thank Evgeny Zhukov, with whom I worked on the Piko II setup and was able to solve many experimental pitfalls. I am very grateful for the joint measurements on the Piko I and Spin Flip Raman setup with Eiko Evers, Vasilii Belykh, Dennis Kudladik and Nataliia Kopteva. A big thank you also goes to Mikhail Glazov, Marina Semina, Mikhail Nestoklon, Evgeny Ivchenko and Dmitry Smirnov who always helped with their experience and theoretical models. Also, without constant supply of first-class samples, this work would have been impossible, my thanks to Julian Höcker, Vladimir Dyakonov, Dmitry Dirin, Maksym Kovalenko, Maria Kuznetsova and Elena Kolobkova. All this would have been impossible without the unparalleled commitment of Manfred Bayer.

During my time as a doctoral student, I was fortunate to be able to carry out projects in St. Petersburg. Each time I was warmly received and well looked after. Each visit was a great pleasure. I would like to thank Vladimir Kalevich, Mikhail Afanasiev, Yuri Kusrayev and Nikolai Kozyrev for a fantastic snowy spring at the Ioffe Institute, Mikhail Petrov and Ivan Ignatiev for a summer of white nights at Peterhof and Victor Sapega and Ina Kalitukha for another unforgettable summer at the Ioffe institute. Further all the colleagues I had the honour to work with.

Special thanks to Fabian Heisterkamp and Tomasz Kazimierczuk who helped me a lot in the early days. I don't want to forget to thank Ilya Akimov, Vladimir Korenev and Olga Ken. Special thanks go to the chair experimental physics 2. Lars Wieschollek, Daniel Tüttmann, Klaus Wiegers, Michaela Wäscher and Katharina Sparka deserve special mention here, without whom this smooth apparatus would not have been functional. I would also like to thank everyone at the chair for an unforgettable time, with scientific and not-so-scientific discussions that often lasted late into the night. Thank you.

It is very important for me to thank my parents, my brother and my friends, who have always had my back and supported me without compromise.

Eidesstattliche Versicherung

Ich versichere hiermit an Eides statt, dass ich die vorliegende Masterarbeit mit dem Titel "Coherent spin dynamics and carrier-nuclear interaction in lead halide perovskite crystals" selbständig und ohne unzulässige fremde Hilfe erbracht habe. Ich habe keine anderen als die angegebenen Quellen und Hilfsmittel benutzt sowie wörtliche und sinngemäßse Zitate kenntlich gemacht. Die Arbeit hat in gleicher oder ähnlicher Form noch keiner Prüfungsbehörde vorgelegen.

Ort, Datum | Unterschrift

Belehrung

Wer vorsätzlich gegen eine die Täuschung über Prüfungsleistungen betreffende Regelung einer Hochschulprüfungsordnung verstößt handelt ordnungswidrig. Die Ordnungswidrigkeit kann mit einer Geldbuše von bis zu 50.000,00 Euro geahndet werden. Zuständige Verwaltungsbeh"orde für die Verfolgung und Ahndung von Ordnungswidrigkeiten ist der Kanzler/die Kanzlerin der Technischen Universität Dortmund. Im Falle eines mehrfachen oder sonstigen schwerwiegenden Täuschungsversuches kann der Prüfling zudem exmatrikuliert werden (§63 Abs. 5 Hochschulgesetz -HG-). Die Abgabe einer falschen Versicherung an Eides statt wird mit Freiheitsstrafe bis zu 3 Jahren oder mit Geldstrafe bestraft. Die Technische Universität Dortmund wird ggf. elektronische Vergleichswerkzeuge (wie z.B. die Software ”turnitin”) zur Überprüfung von Ordnungswidrigkeiten in Prüfungsverfahren nutzen.

Die oben stehende Belehrung habe ich zur Kenntnis genommen.

Ort, Datum | Unterschrift